THE USE OF NANOSTRUCTURED 316L STAINLESS STEEL FOR
ORTHOPEDIC AND CARDIOVASCULAR APPLICATIONS: FABRICATION,
CHARACTERIZATION, AND *IN VITRO* CELLULAR INTERACTIONS

A THESIS SUBMITTED TO
THE GRADUATE SCHOOL OF NATURAL AND APPLIED SCIENCES
OF
MIDDLE EAST TECHNICAL UNIVERSITY

BY

YAŞAR KEMAL ERDOĞAN

IN PARTIAL FULFILLMENT OF THE REQUIREMENTS
FOR
THE DEGREE OF DOCTOR OF PHILOSOPHY
IN
BIOMEDICAL ENGINEERING

JANUARY 2024

Approval of the thesis:

THE USE OF NANOSTRUCTURED 316L STAINLESS STEEL FOR ORTHOPEDIC AND CARDIOVASCULAR APPLICATIONS: FABRICATION, CHARACTERIZATION, AND *IN VITRO* CELLULAR INTERACTIONS

submitted by **YAŞAR KEMAL ERDOĞAN** in partial fulfillment of the requirements for the degree of **Doctor of Philosophy** in **Biomedical Engineering, Middle East Technical University** by,

Prof. Dr. Halil Kalıpçılar
Dean, Graduate School of **Natural and Applied Sciences**   _____

Prof. Dr. Vilda Purutçuoğlu
Head of the Department, **Biomedical Engineering**   _____

Assoc. Prof. Dr. Batur Ercan
Supervisor, **Metallurgical and Materials Eng., METU**   _____

Prof. Dr. Pelin Mutlu
Co-Supervisor, **Biotechnology, Ankara University**   _____

Examining Committee Members:

Prof. Dr. Ayşen Tezcaner
Engineering Science, METU   _____

Assoc. Prof. Dr. Batur Ercan
Metallurgical and Materials Eng., METU   _____

Prof. Dr. İrem Erel Göktepe
Chemistry, METU   _____

Assoc. Prof. Dr. Burak Derkuş
Chemistry, Ankara University   _____

Asst. Prof. Dr. Cem Bayram
Nanotechnology and Nanomedicine, Hacettepe Uni.   _____

Date: 16.01.2024

I hereby declare that all information in this document has been obtained and presented in accordance with academic rules and ethical conduct. I also declare that, as required by these rules and conduct, I have fully cited and referenced all material and results that are not original to this work.

Name Last name: Yaşar Kemal Erdoğan

Signature:

ABSTRACT

THE USE OF NANOSTRUCTURED 316L STAINLESS STEEL FOR ORTHOPEDIC AND CARDIOVASCULAR APPLICATIONS: FABRICATION, CHARACTERIZATION, AND *IN VITRO* CELLULAR INTERACTIONS

Erdoğan, Yaşar Kemal
Doctor of Philosophy, Biomedical Engineering
Supervisor: Assoc. Prof. Dr. Batur Ercan
Co-Supervisor: Prof. Dr. Pelin Mutlu

January 2024, 98 pages

316L stainless steel (SS) is one of the commonly-used implant materials in biomedical applications due to its ideal mechanical properties, acceptable biocompatibility, and low cost. However, the bioinert nature of 316L SS led to limited osteointegration in orthopedic applications, and poor endothelization in cardiovascular applications. Furthermore, infection, nickel ion release, stent restenosis and limited corrosion resistance are major clinical challenges for SS and led to gradual decline of its use as an implant material.

To eliminate the aforementioned issues, nanoscale surface modification on 316L SS can be a potential remedy. In this thesis, nanostructures having different morphologies and feature sizes were fabricated on the surfaces. Afterwards, the physical and chemical properties of anodized surfaces were characterized.

For orthopedic applications, *in vitro* cellular interactions showed that bone cell viability on 200 nm nanodimple surfaces was promoted up to 68% compared to non-anodized surfaces. Moreover, a 71% and 58% decrease in *S. aureus* and *P.*

aeruginosa colonies were detected on 200 nm nanodimple surfaces compared to the non-anodized surfaces.

For cardiovascular applications, *in vitro* HUVECs functions thrived on the nanostructured surfaces. Furthermore, the nanostructured surfaces significantly promoted endothelial cell viability, enhanced cellular migration, stimulated nitric oxide and prostaglandin secretion, while down-regulating the expressions of VCAM and ICAM gene and decreased platelet adhesion and hemolysis rate.

The findings of this thesis indicate that nanostructured 316L SS surfaces improved corrosion resistance and enhanced endothelization and hemocompatibility. Simultaneously, these surfaces promoted osteoblast interactions and restricted the bacterial attachment, showcasing their potential for biomedical applications.

Keywords: 316L SS; Anodization; Nanostructure; Surface topography; Bioactivity

ÖZ

ORTEPEDİK VE KARDİYOVASKÜLER UYGULAMALAR İÇİN NANOYAPILI 316L PASLANMAZ ÇELİĞİN KULLANIMI: ÜRETİMİ, KARAKTERİZASYONU VE *İN VİTRO* HÜCRESEL ETKİLEŞİMİ

Erdoğan, Yaşar Kemal
Doktora, Biyomedikal Mühendisliği
Tez Yöneticisi: Doç. Dr. Batur Ercan
Ortak Tez Yöneticisi: Prof. Pelin Mutlu

Ocak 2024, 98 sayfa

316L Paslanmaz çelik (SS) ideal mekanik özellikleri, kabul edilebilir biyouyumluluğu ve düşük maliyeti nedeniyle biyomedikal uygulamalarda yaygın olarak kullanılan implant malzemelerinden biridir. Ancak, 316L SS biyo-etkisiz yüzey özelliği, ortopedik uygulamalarda sınırlı osteointegrasyona, kardiyovasküler uygulamalarda ise zayıf endotelizasyona yol açmaktadır. Ayrıca, enfeksiyon, nikel iyon salımı, stent restenozu ve sınırlı korozyon direnci SS için önemli klinik zorluklardır ve implant malzemesi olarak kullanımının giderek azalmasına yol açmıştır.

Yukarıda belirtilen sorunları ortadan kaldırmak için 316L SS yüzeyine nano ölçekli modifikasyonu potansiyel bir çözüm olabilir. Bu tezde, yüzeyler üzerinde farklı morfoloji ve boyutlara sahip nanoyapılar üretildi. Daha sonra anodize yüzeylerin fiziksel ve kimyasal özellikleri karakterize edilmiştir.

Ortopedik uygulamalar için i*n vitro* hücre etkileşimler, 200 nm boyutundaki nanohendek yüzeylerin kemik hücre canlılığını, çıplak yüzeylere kıyasla %68'e

kadar artırmıştır. Ayrıca 200 nm nanohendek yüzeylerde çıplak yüzeylere kıyasla *S. aureus* ve *P. aeruginosa* kolonilerinde %71 ve %58 oranında azalma tespit edildi.

Kardiyovasküler uygulamalar için *in vitro* endotel hücre fonksiyonlarının nano yapılı yüzeyler üzerinde gelişmiştir. Ayrıca, nanoyapılı yüzeylerin endotel hücre canlılığını önemli ölçüde arttırdığı, hücresel göçü desteklediği, nitrik oksit ve prostaglandin salımını uyarırken, VCAM ve ICAM gen ifadesini sınırladığı ve trombosit yapışması ile hemoliz oranını azalttığı görülmüştür.

Bu tez çalışmasının bulguları, nanoyapılı 316L paslanmaz çelik yüzeylerin korozyon direncini arttırdığı, endotelizasyon ve kan uyumluluğunu desteklediğini göstermektedir. Eş zamanlı olarak bu yüzeylerin kemik doku etkileşimlerini desteklediği ve bakteri tutunmasını kısıtladığını, biyomedikal uygulamalara yönelik potansiyelini ortaya çıkarmaktadır.

Anahtar Kelimeler: 316L paslanmaz çelik; Anodizasyon; Nanoyapı; Yüzey topografyası; Biyoaktivite

To

The 100th Anniversary of the Republic of Turkey…

My Beloved Parents & My Love

ACKNOWLEDGMENTS

TABLE OF CONTENTS

LIST OF TABLES

LIST OF FIGURES

FIGURES

xvi

LIST OF ABBREVIATIONS

ABBREVIATIONS

AFM   atomic force microscopy

End-1   Endothelium-1 function

FBS   fetal bovine serum

HFOB   human osteoblast cell

HUVEC   human umbilical vein endothelial cell

ISR   in-stent restenosis

MTT   3-4,5-dimethyl-thiazolyl-2,5-diphenyltetrazolium bromide

NA   non-anodized surface

ND25   nanodimple 316L stainless steel having 25 nm feature size

ND200   nanodimple 316L stainless steel having 200 nm feature size

NO   nitric oxide

NP25   nanopit 316L stainless steel having 25 nm feature size

NP200   nanopit 316L stainless steel having 200 nm feature size

PRP   platelet rich plasma

SEM   scanning electron microscopy

SS   stainless steel

XPS   x-ray photoelectron spectroscopy

CHAPTER 1

INTRODUCTION

316L stainless steel (316L SS) is among the commonly used implant materials in cardiovascular, dental and orthopedic applications (Bekmurzayeva et al., 2018). As illustrated in Figure 1.1, 316L SS presents numerous opportunities as an implant material in the body. This material is preferred due to its ideal mechanical properties and corrosion resistance, acceptable biocompatibility, and ease of manufacturing (Chen & Thouas, 2015; Nouri & Wen, 2021). 316L SS also provides a significant price advantage compared to other metallic biomaterials (*i.e*., titanium and titanium alloys), which makes it the material of choice to fabricate implants in the developing and underdeveloped countries across the world (Sutha et al., 2013; Mohandesnezhad et al., 2022).

There are various types of stainless steel, which are classified by their microstructure: austenitic, ferritic, martensitic and duplex steel. The austenitic phase of 316L stainless steel is commonly preferred in application and mainly composed of iron, chromium, nickel, molybdenum and a low amount of carbon (hence the 'L'). It has a face-centered cubic (FCC) crystal structure, and characterized by very low yield strength-to-tensile strength ratio (Talha et al., 2013). Chromium content of 316L SS provides resistant to corrosion and improve its oxidation resistance at high temperatures. The presence of low amounts of carbon (0.03 wt%) also improves its corrosion resistance and minimizes potential adverse tissue response (Chen & Thouas, 2015). In addition, austenitic 316L SS has non-magnetic properties, which is critical for magnetic resonance imaging use, and therefore it is preferable for orthopedic applications.
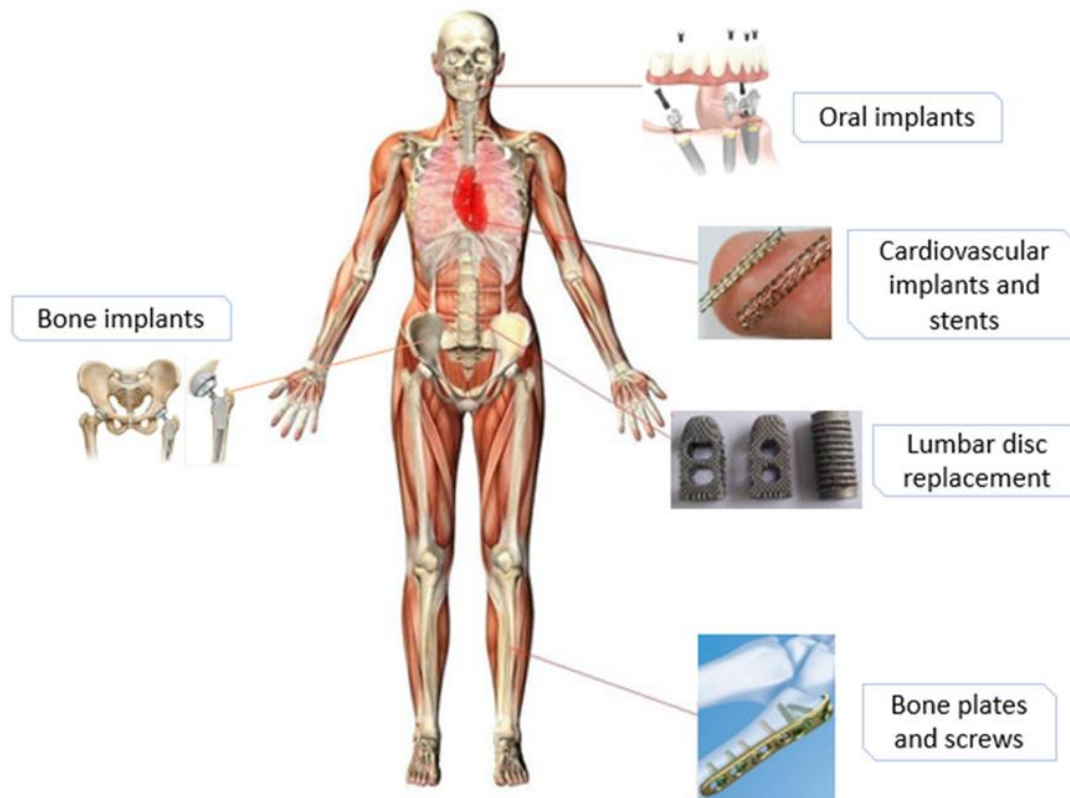
Figure 1.1 Major applications of 316L SS as an implant material in the body
(Resnik et al., 2020)

1.1 The Problems Associated with 316L Stainless Steel Implant in Biomedical Application

Despite its numerous advantages, there are some clinical challenges of using 316L SS implants in the body, such as its bioinert nature, localized corrosion problems, nickel ion release, which can lead to allergenic and inflammatory effects, as well as platelet activation and thrombosis formation. In addition, bacterial attachment and the risk of infection is also critical for 316L SS implants. Surface modification of 316L SS was proposed to overcome these complications (Staruch et al., 2017; Cherian et al., 2022). In this thesis, we investigated major problems associated with the use of 316L SS separately for orthopedic and cardiovascular applications.

1.1.1   Orthopedic Applications

The bioinert nature of 316L SS hinders the desired cellular response; limits new bone formation and osseointegration in orthopedic applications. Inadequate osseointegration would lead to micromotion of the implant and, in the long run, result in failure due to aseptic loosening. Aside from lacking bioactivity, another important problem of 316L SS implants is their septic failure. Since 316L SS does not possess any antibacterial activity, once bacteria attach and subsequently form a biofilm on its surfaces, it is very difficult to eradicate it. Frequently, it requires a revision surgery and replacement of the implant. Considering that most bacteria build resistance to commonly-used antibiotics, fighting with infection is becoming a pressing issue.

In clinics, infection poses significant drawbacks for all orthopedic applications, and there is still no definitive remedy for this issue. Therefore, treating an implant infection can be challenging due to the complexity of the process, the high cost associated with the treatment, and often the requirement for a revision surgery. Bacterial attachment on implant surfaces is a critical and plays an important role in the formation of biofilm. Once bacteria adhere to the implant surfaces, they begin to form a biofilm. The biofilm is a colony of bacteria that adhere to each other and to a surface. Biofilm formation consist of mainly three steps: i) initial attachment and adherence of bacteria, ii) accumulation due to cellular aggregation, and iii) biofilm detachment of bacterial cells (Lu et al., 2022). Thus, once biofilm forms, it is difficult to eradicate the infection by the host immune system and antibiotic therapy. Therefore, it can lead to various complications, including tissue damage and implant failure. That being said, if initial attachment of bacteria to implant surfaces can be prevented, it provides a crucial factor in preventing biofilm formation and reducing the risk of infection. Thus, a desirable orthopedic implant material is anticipated to hinder bacterial attachment or minimize biofilm formation. Simultaneously, it should enhance the cellular responses, and particularly promote osseointegration.

Staphylococcus aureus (*S. aureus*) and *Staphylococcus epidermidis* (*S. epidermis*) are the most common bacteria causing implant infection (Pietrocola et al., 2022). For example, an examination involving 242 orthopedic patients for infections linked to both internal and external fixation systems revealed that *S. aureus* was the primary pathogen. Conversely, infections associated with knee and hip arthro-prostheses exhibited *S. epidermidis* as the predominant bacterial species (Montanaro et al., 2011). Another study from UK showed that 44% of orthopedic implant infections were caused by *S. aureus* (Lamagni, 2014).

It was first discovered that cicada wings having nanotopography showed antibacterial effect against *Pseudomonas aeruginosa* (*P. aeruginosa*), as illustrated in Figure 1.2b (Ivanova et al., 2012). In addition, it was found that natural nanotopography of dragonfly wings showed bactericidal properties (Bandara et al., 2017). Thus, nanostructured modification of implant surfaces emerged as a promising approach for preventing bacterial attachment and biofilm formation. The surface properties, such as surface topography, charge, chemistry and energy, play critical roles in the bacterial attachment (Cheng et al., 2019; Zheng et al., 2021). Especially, creating a nanostructured topography on implant surfaces can be a promising strategy to improve the biological response, and at the same time prevent bacterial colonization on 316L SS implant surfaces (Herath et al., 2022; Rasouli et al., 2018).
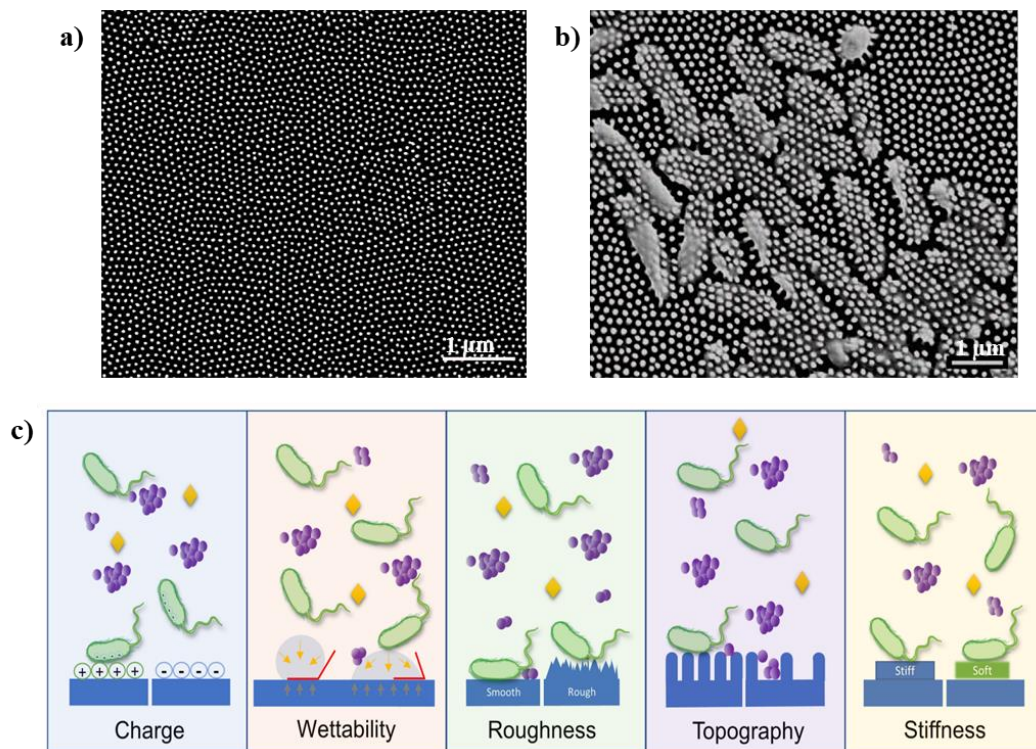
Figure 1.2 a) Scanning electron microscope (SEM) image of the nanostructured surface of cicada wing, b) bactericidal effect of the nanostructured on cicada wing towards *P. aeruginosa* (Ivanova et al., 2012), c) schematic illustration of various surface properties which influence bacterial attachment (Zheng et al., 2021).

1.1.2 Cardiovascular Application

Coronary artery disease (CAD) is primarily caused by atherosclerotic plaque formation inside the coronary arteries, which carry oxygen rich blood to the heart. CAD is the leading cause of mortality worldwide, and it is associated with 17.8 million deaths annually (Brown et al., 2023). The inner layer of coronary arteries consists of endothelial cells, which provides an anticoagulant barrier between the vessel walls and blood. Therefore, endothelial cells have major role in maintaining hemostasis and regulate thrombosis, platelet adhesion, smooth muscle cell proliferation, inflammation and blood flow (Galley & Webster, 2004; Pober & Sessa, 2007). Endothelial dysfunction plays a major role in the formation of atherosclerosis

(Jebari-Benslaiman et al., 2022). Atherosclerosis is a progressive condition where fatty deposits, cholesterol, calcium, and other substances accumulate on the inner walls of the coronary arteries, as shown in Figure 1.3 (Libby et al., 2019). These deposits form plaques that narrow or block the arteries. When coronary arteries are narrowed or blocked, oxygen and nutrient-rich blood cannot reach heart muscle. When this situation occurs, heart muscle cells begin to die, potentially leading to arrhythmia and heart attack. Eventually, it can result in fatality.
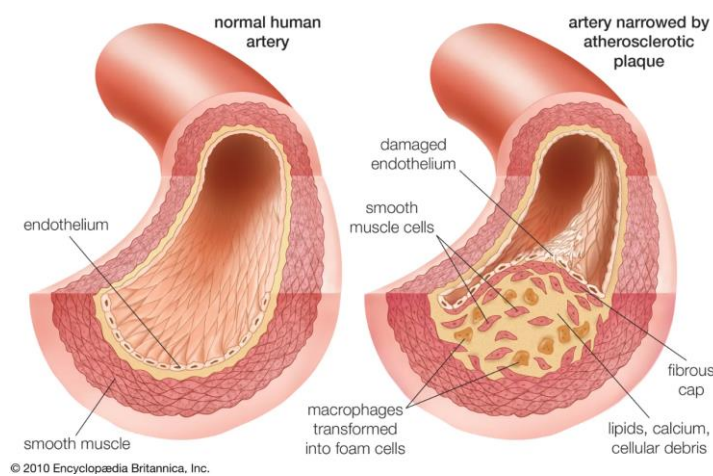
Figure 1.3 Healthy artery (on the left) compared with an artery affected by atherosclerosis (on the right) (Britannica, 2023).

1.1.2.1 Coronary Artery Stent

Arterial stent application is one of treatment methods for coronary artery disease. A stent is a small and expandable tube made of metal or polymer, and it is crimped onto a balloon catheter. Stent is inserted into the narrowed arteries to treat or prevent a blockage and keep them open (Fu et al., 2020). Figure 1.4 illustrates the steps involved in stent placement in a narrowed artery. When balloon tip of the catheter reaches the plaque formed against the artery wall, the balloon is expanded to push the plaqued artery walls open. Once the artery is widened, the balloon is deflated and

removed, while the stent is locked in place, holding the vessel open even after the balloon is deflated. The stent remains in place permanently to maintain the widened artery.
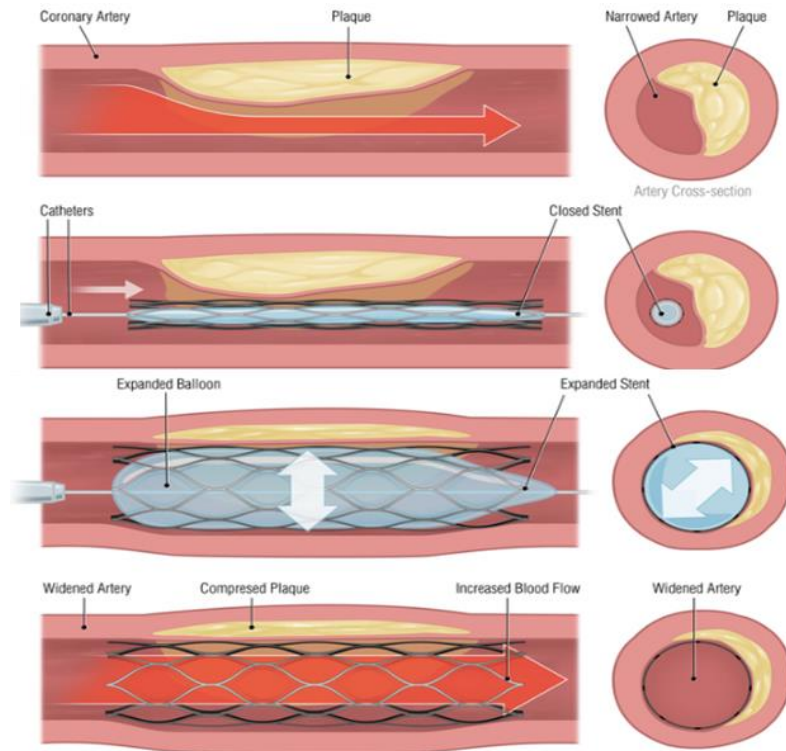
Figure 1.4 A schematic representation of the stent implantation inside a narrowed artery.

1.1.2.2 Challenges of Using 316L SS Bare Metal Stent

The first successful stent implantation in a coronary artery was in 1986 (Iqbal et al., 2013). The demand for stents is significantly increasing each year due to the growing prevalence of heart disease and population growth (Fu et al., 2020). 316L SS is one of the most-commonly used stent materials due to its ideal mechanical properties, and low elastic recoil (Wang et al., 2018). However, various issues related to 316L SS, as well as the implanted stent material of choice, can lead to unsuccessful clinical applications. Firstly, using bare metal surfaces, which are bioinert, cause delayed

endothelization, and may potentially promote inflammation and smooth muscle cell proliferation.

In-stent restenosis (ISR) is another major issue in clinical applications. ISR is defined as the re-narrowing of a stented coronary artery after stent implantation (Torrado et al., 2018). This re-narrowing is a result of endothelial cell layer damage with subsequent neointimal proliferation around the stent. Vascular smooth muscle cells migrate towards areas of injury, proliferate and form the neointimal. ISR remains an essential problem in all cardiovascular stent applications, and it occurs about 10–30% of the cases after stenting (Yao et al., 2021).
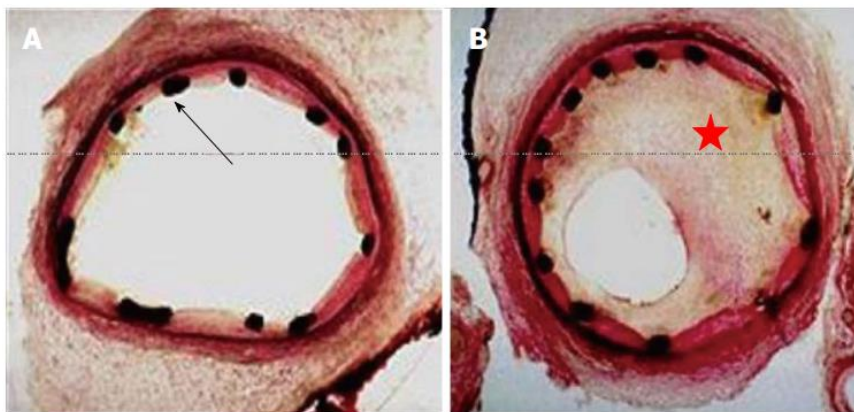
Figure 1.5 a) Cross-section of a coronary artery immediately after bare metal stent implantation, and b) formation of significant in-stent restenosis with neointimal hyperplasia (red star) after six months of bare metal stent implantation (Chadi et. al, 2017).

Stent thrombosis is another significant complication in clinical application. Stent thrombosis pertains to the development of blood clots on the stent surface, which can cause sudden blockage of the stenting artery. Stent thrombosis can occur at acute, subacute, early (within 30 days after implantation), late (between 1 month and 1 year), and very late (>1 year after implantation) periods after implantation. A study revealed that stent thrombosis is associated with a mortality rate ranging from 5% to

45% and recurrence rate of 15–20% at 5 years. (Gori et al., 2019; Noaman et al., 2020). There are many reasons for stent thrombosis, such as delayed re-endothelization on the stent surface, surface properties of the stent, slow coronary blood flow, and low shear stress leading to activation of the intrinsic pathway. Platelet activation on the stent surface may also cause stent thrombosis.

On the other hand, corrosion and wear of 316 SS stents in the body are major issues and leading to the failure of implantation. The surface chemistry and its passive film layer of stainless steel directly affect the corrosion behavior of surface. When a stent corrodes, it loses its mechanical properties and releases harmful metal ions (Koster et al., 2001). Nickel ion releases have adverse effect on human, which may cause inflammation, skin allergen or carcinogenicity in human body (Yang & Ren, 2010). This metal ions releases from stent surface could change local tissue microenvironment that leading to inflammation mediators and promote stent restenosis. For example, Saito suggested that nickel ion releases from bare 316L surface could major factor to stent restenosis (Saito et al., 2009).

In order to address these clinical challenges, novel stent designs and material development research are critical (Clare et al., 2022). For instance, the development of drug-eluting stents and bioabsorbable stents are innovative strides in this field. However, drug-eluting stents have major long-term problems, such as delayed endothelization and healing, late and very late stent thrombosis, and inflammation. On the other hand, biodegradable stents promise new developments and may help address some of these issues in clinical applications. Nonetheless, it come with certain limitations. Biodegradable polymer stent have lower mechanical strength, while biodegradable metal stents have shorter degradation times, which compromise radial strength (Zong et al., 2022). To enhance the mechanical properties of biodegradable stents, they are fabricated to have thicker struts compared to traditional metal stents. However, the thicker struts can affect blood flow dynamics and may contribute to a higher risk of restenosis (Bowen et al., 2016). Also, biodegradable stents may delay the healing process, and potentially lead to thrombosis. In the case of biodegradable stent using Mg or Zn alloys, gas bubbles

can be released, and likely to delay healing of the vessel by accumulating around the implant (Im et al., 2017).

Numerous research efforts aim to address the aforementioned issues, seeking to minimize adverse effects and establish an ideal stent surface for clinical applications (Jaganathan et al., 2014). Critically, the stent surface must be offer rapid endothelization, high corrosion resistance, and optimal hemocompatibility for successful stent implantation (Bian et al., 2022; Fu et al., 2020). Towards this goal, surface modifications to create a nanostructure on the 316L SS stent surface can be a promising method to enhance the functional cellular integrity of the stent material (Park et al., 2020).

1.2 Surface Modification: Anodization

Anodization (anodic oxidation) is a electrochemical process to grow an oxide layer on the surfaces of valve metals upon the application of a DC potential in certain electrolytes. The anodization method can be applied to various metals, such as titanium and titanium alloys (Gardin et al., 2021; Chopra et al., 2021), aluminum (Feng et al., 2014), tantalum (Uslu et al., 2021), iron (M. Li et al., 2017), zinc (Guillory et al., 2019; Sanchez et al., 2011), stainless steel (Dhawan et al., 2017a), Co-Cr (Nagai et al., 2014), and *etc*. By controlling the anodization parameters, it is possible to fabricate oxide based nanofeatures on metallic surfaces, including aluminum (Davoodi et al., 2020; S. Liu et al., 2021), titanium (Minagar et al., 2012; Piszczek et al., 2020), zirconium (Zal et al., 2022), and *etc*. A basic set-up for anodization of 316L SS is shown in Figure 1.6. The anodization set-up consists of two electrodes, where 316L SS serves as the anode and platinum serve as the cathode, an electrolyte, and an electrical connection to a DC power supply. The nanostructured surface properties, which include feature size, topography and morphology of the nanostructures, can be controlled by changing electrochemical parameters, such as applied DC potential, anodization duration, electrolyte type and concentration, temperature, pH, anode-cathode distance, and etc.

10
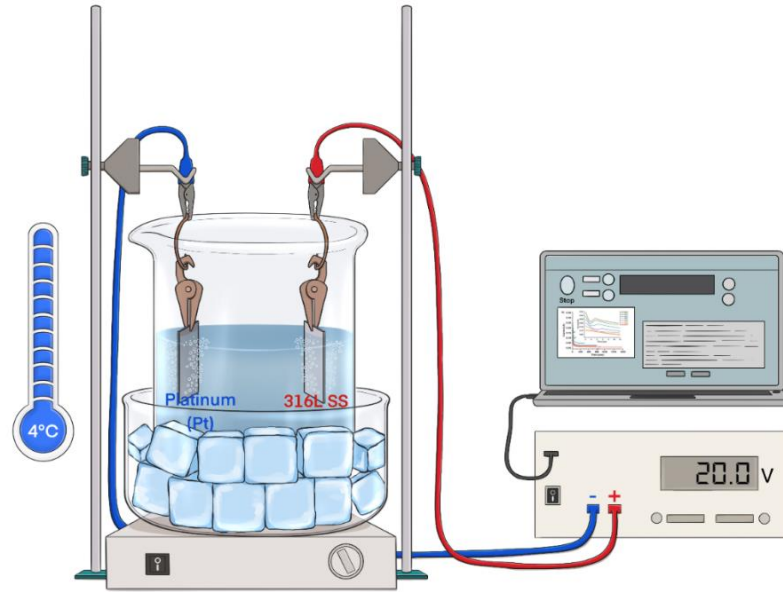
Figure 1.6 Schematic representation for anodization of 316L SS.

The anodization mechanism of stainless steel is complicated and still unclear, and it requires further research (Zhao et al., 2021). In literature, several studies revealed that the use of perchloric acid as an electrolyte for the anodization of stainless steel provides formation of nanostructures on the surfaces (Tsuchiya et al., 2012; Benčina et al., 2022). Also, various studies used H_2SO_4 (Asoh et al., 2016) or NH_4F (Kure et al., 2012) containing electrolytes to fabricate nanostructures on stainless steel. The most-widely accepted mechanism for the anodization of 316L SS consists of three stages (Domínguez et al., 2019). In the first step, when 316L SS is exposed to a sufficient DC potential in an electrolyte solution, the formation of an oxide layer on the surface occurs (1).

$$xM(Cr, Fe, Ni) + \frac{y}{2}O_2 \; \rightarrow \; M_xO_y \; (Cr_2O_3, Fe_2O_3, NiO) \tag{1}$$
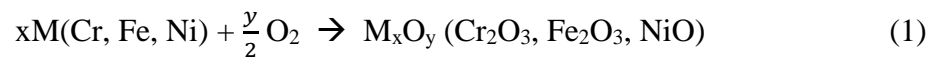
In the second step, dissolution of the oxide layer starts and nanostructure formation begins on the surfaces (2). The electrolyte color changes to brown-yellow during anodization, which indicates the dissolution of the oxide layer.

$$Cr_2O_3 + 6H^+ \; \rightarrow \; 2Cr^{3+} + 3H_2O \tag{2}$$

11

$$Fe_2O_3 + 6H^+ \quad \rightarrow \quad 2Fe^{3+} + 3H_2O$$

$$NiO + 2H^+ \quad \rightarrow \quad Ni^{2+} + H_2O$$
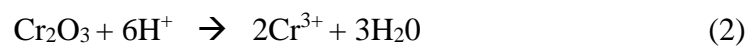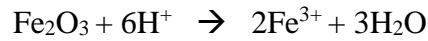
In the third stage, the reaction between dissolution and oxide formation reaches an equilibrium, and a balance is established for the growth of the nanostructure oxide layer.

1.2.1 Anodization for Orthopedic Application

In the last couple of decade, anodization of different metallic implant components received considerable attention due to it is simplicity and ability to obtain nanofeatures having different feature sizes and morphologies by changing the anodization parameters, *i.e.*, voltage, time, and etc. (Indira et al., 2015; L. Mohan et al., 2020; Zhao et al., 2021). For instance, our research group previously created nanopores, nanodimples, nanotubes, and nanocoral morphologies on tantalum surfaces and controlled the feature size of these morphologies between 20 and 140 nm to enhance the osteoblast (bone cell) functions on these surfaces (Uslu et al., 2021). In other study, we formed nanotubular structures on titanium surfaces via anodization, and controlled the feature size of these nanotubular structures between 25 and 140 nm. The nanotubular structures improved exosome secretion, which in turn stimulated the endothelial cell viability (Gardin et al., 2021). A similar study showed that aluminum could be anodized to obtain nanopores have a pore size range of 25–75 nm, and it was found that the larger pore size on anodized aluminum dramatically enhanced cellular proliferation (Ni et al., 2014). Also, our research group showed that anodized nanostructured tantalum surfaces enhanced stem cell differentiation and improve corrosion resistance (Erdogan et al., 2023).

Similarly, *in vivo* studies confirmed that anodized nanostructured Ti6Al4V surfaces promoted osteoblast proliferation and differentiation compared to the untreated Ti6Al4V surface. Moreover, the *in vivo* results of rat animal model demonstrated that 8 weeks after the surgery, the ratio of bone volume to total volume of anodized

implant was 43.4%, which represented 1.5 times that of the control implant, as shown in Figure 1.7. In addition, the nanostructured implant surfaces significantly enhanced new bone formation and the direct bone integration between the implant and bone tissue (Ren et al., 2021).
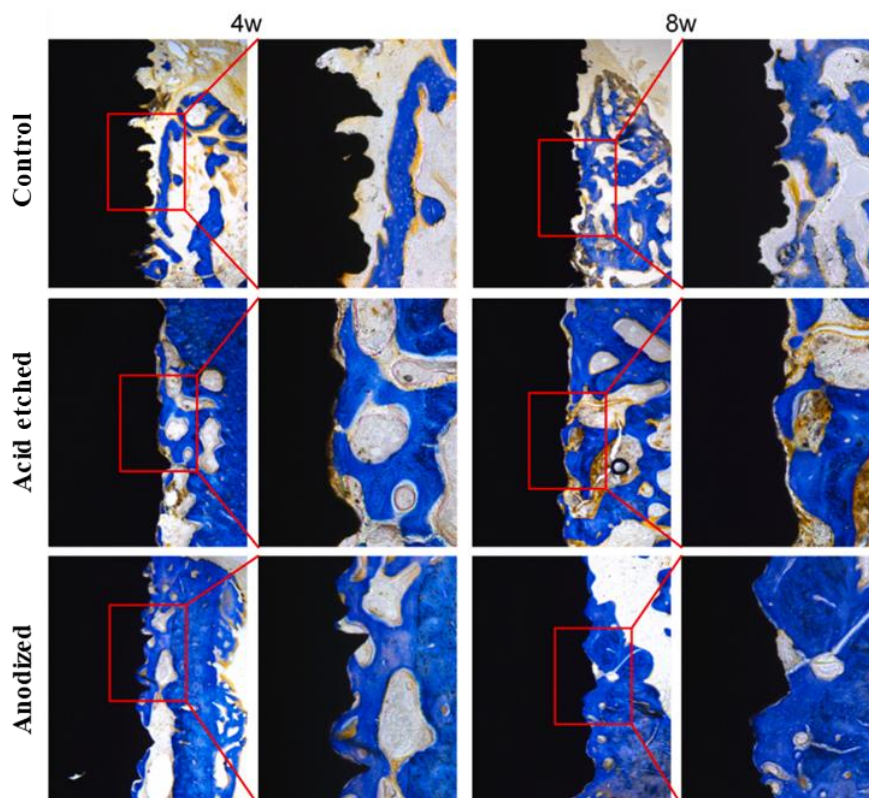
Figure 1.7 Histological staining at week 4 (left) and week 8 (right) after implantation. The blue, light yellow, and black parts are bone tissue, fibrous tissue, and Ti6Al4V implant, respectively (Ren et al., 2021).

Several studies investigated the fabrication of nanostructures on 316L SS surfaces via anodization, and characterized the effect of anodization on surface properties (Łyczkowska-Widłak et al., 2020; Benčina et al., 2022), cellular functions (Latifi et al., 2013; Dhawan et al., 2017), and bacterial colonization (Gonzalez et al., 2021; Rodriguez-Contreras et al., 2018). For example, anodized 316L SS surfaces containing both micro- and nanopores were shown to induce osteoblast-like cell adhesion, which was correlated with increased surface roughness (Hsu et al., 2020).

In a recent study, anodized 316L SS implants were shown to improve bone recovery 4 weeks after implantation and supported osseointegration in a rabbit model. However, these anodized implants had non-uniform and unordered nanostructures on implant surfaces (Cho et al., 2021). Aside from tissue interactions, various studies identified the nanostructured surface topography to inhibit attachment and growth of bacteria (Resnik et al., 2020; Chopra et al., 2021). Though the anodization method was not used, nanoscale surface topography on SS was shown to be critical in limiting *S. aureus* and *P. aeruginosa* colony formation (Wu et al., 2018). In addition, Jang et al. showed that nanotextured 316L SS surfaces fabricated by electrochemical etching significantly inhibited *Escherichia coli* (*E. coli*) and *S. aureus* attachment. Though nanofeatures were identified to inhibit bacteria colonization, it should be noted that aforementioned nanotextures were irregular and did not possess an array of repeating nanostructured topographical features (Jang et al., 2018).

Although nanofeatured surfaces on 316L SS were fabricated via different techniques to interact with various tissues, most of the fabricated surface features were non-uniform. They could not be scaled-up for large curved areas, and they were prone to delamination failure, which would limit their use in orthopedic applications. Anodization of 316L SS to provide uniform and controllable nanofeatures would be advantageous, and optimization of the nanofeature size to enhance bone cell functions and anti-fouling properties is required for their adaptation in orthopedic applications. Therefore, the first aim of the thesis study is to identify a surface topography that enhances bone cell interactions and, at the same time, limit bacterial colonization on 316L SS. For this purpose, we fabricated and characterized ND structures on 316L SS using anodization. The effect of the ND size on bone cell functions and anti-fouling properties against Gram-positive *S. aureus* and Gram-negative *P. aeruginosa* was investigated.

1.2.2 Anodization for Cardiovascular Application

There are several studies in the literature investigating the anodization of implant materials used for stents *in vitro* and *in vivo*. For example, Nuhn et al. indicated that titanium stents having 90nm diameter nanotubular structures reduced stenosis by 30% compared to the bare stainless steel surfaces, as shown in Figure 1.8 (Nuhn et al., 2017). In addition, the nanostructured Ti stent showed 15.6% and 5.6% thinner neointima over the struts compared to the bare Ti and SS stents.
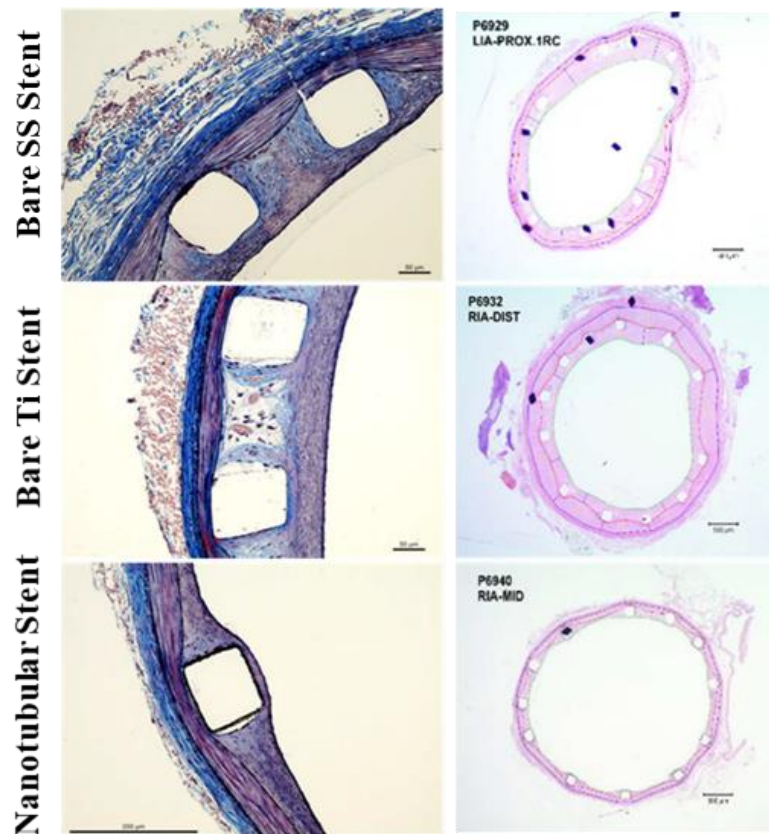
Figure 1.8 Stented rabbit arteries after 28 days of implantation. The nanoengineered stents showed a 15.6% and 5.6% thinner neointima over the struts compared to the bare Ti stent and bare SS stent control groups (Nuhn et al., 2017).

In another study, it was demonstrated that anodized zinc implants enhanced corrosion resistance and improved endothelization with no observed neointimal growth. However, the success rate of the polished implant surface in the experiment was observed to be only 44% due to lack of endothelization and the absence of roughness on the implant surface (Guillory et al., 2019).

In other study, nanoscale coated titania on stainless steel stent surfaces was shown to improve endothelization. In addition, about 50% decrease in neointimal stenosis, and no thrombosis formation were observed after implantation in rabbit artery for 8 weeks *in vivo*. However, significant lumen narrowing and in-stent restenosis were observed in the bare SS stent. This stent restenosis occurrence is related to poor endothelization with no tissue ingrowth and lack of nanoscale topography on stent surface, as shown in Figure 1.9 (Cherian et al., 2020).
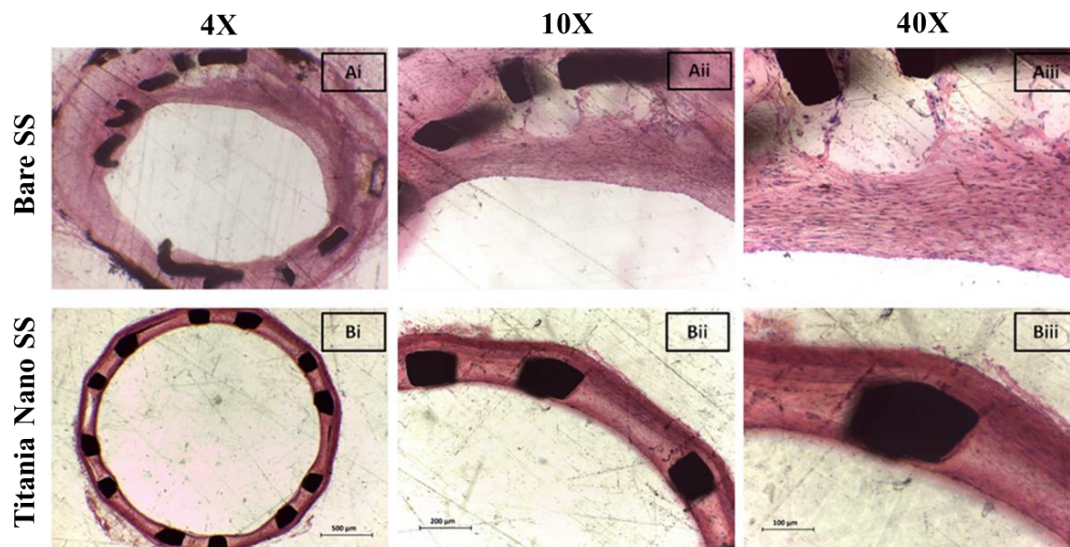
Figure 1.9 The histology images of bare (top) and b) nanoscale titania coated SS stent (bottom) after 8 weeks of implantation (Cherian et al., 2020).

1.3   Aim of the Study

Despite its widespread use, 316L stainless steel implants still have major drawbacks in biomedical applications. Various studies are continually exploring surface

modifications to address challenges and improve the biocompatibility of 316L SS implants. That being said, there is a limited number of studies investigating the fabrication of nanostructures on 316L SS and their biological interactions *in vitro* for both orthopedic and cardiovascular applications. To fill this gap in literature, in the first chapter of the thesis, we briefly introduced 316L stainless steel implants used in biomedical applications, stated material induced drawbacks of using 316L SS, and highlighted surface modification as a potential remedy. In the second chapter, we investigated the use of nanostructured 316L SS for orthopedic applications, and how osteoblast functions and bacterial colonization were altered upon the surface modification. In the third chapter, we comprehensively investigated nanostructured surface for cardiovascular stent applications. Endothelial cell viability, migration, functions, gene expression, along with platelet adhesion and hemolysis rate were investigated. In the final chapter of the thesis, we discussed the results and future perspectives of the nanoscale modified 316L SS implants for biomedical devices.

Thus, the aims of this thesis are as follows:

    1- For orthopedic applications;

Chapter 2 focuses on improving the osteoblast cellular interactions and limiting the bacterial attachment on implant surfaces. Therefore, this chapter aims;

(i)   to obtain nanostructures (ND) on the 316L stainless steel surfaces and to characterize of physical and chemical properties of the nanostructured surfaces,

(ii)   to investigate the osteoblast cellular interactions with the nanostructured 316L SS surfaces,

(iii)   to investigate anti-fouling and antibacterial properties of nanostructured 316L SS surfaces.

2- For cardiovascular stent applications;

Chapter 3 focuses on improving corrosion resistance, enhancing endothelization, as well as limiting stent restenosis and thrombosis for stent applications. Therefore, this chapter aims;

(iv)   to obtain two different morphologies (ND and NP) with different feature sizes to enhance corrosion behavior and limit nickel ion release.

(v)   to evaluate human umbilical vein endothelial cell (HUVEC) interactions (proliferation, migration, cellular morphology, cellular functions and gene expression) with the nanostructured 316L SS surfaces.

(vi)   to limit platelet attachment onto the nanostructured 316L SS surfaces.

CHAPTER 2

ANODIZED NANOSTRUCTURED 316L SS ENHANCES OSTEOBLAST FUNCTIONS AND EXHIBITS ANTI-FOULING PROPERTIES

In this study, arrays of nanodimples (NDs) having controlled feature sizes between 25 and 250 nm were obtained on 316L SS surfaces by anodization. Results demonstrated that the fabrication of NDs increased the surface area and, at the same time, altered the surface chemistry of 316L SS to provide chromium oxide- and hydroxide-rich surface layers. *In vitro* experiments showed that ND surfaces promoted up to a 68% higher osteoblast viability on the fifth day of culture. Immunofluorescence images confirmed a well-spread cytoskeleton organization on the ND surfaces. In addition, higher alkaline phosphate activity and calcium mineral synthesis were observed on the ND surfaces compared to the non-anodized 316L SS. Furthermore, a 71% reduction in *S. aureus* and a 58% reduction in *P. aeruginosa* colonies were observed on the ND surfaces having a 200 nm feature size compared to non-anodized surfaces at 24 h of culture. Cumulatively, the results showed that ND surface nano topography fabricated on 316L SS via anodization enhanced osteoblast viability and functions, while preventing *S. aureus* and *P. aeruginosa* biofilm synthesis.

2.1 Materials and Methods

2.1.1 Sample Preparation

Austenitic 316L SS foil (0.5mm) was cut into 1 x 1 cm^2 sized samples. Prior to anodization, samples were ultrasonically cleaned in acetone, ethanol and distilled water each for 10 minutes, respectively. For anodization, the samples were connected to a DC power supply (Genesys 300V/5, TDK Lambda) which had a two-electrode

configuration. A platinum mesh was used as the cathode and 316L SS samples were used as the anode. 316L SS samples were anodized in ethylene glycol monobutly ether (EG, Sigma-Aldrich) solution containing 7.5 % (v/v) perchloric acid ($HClO_4$, Sigma-Aldrich) to obtain nanofeatured surfaces. Anodization experiments were carried out at temperatures lower than 6 °C. To control feature size of the nanofeatures, applied potentials were altered between 25 and 80 V, and anodization durations were set between 1 and 20 min. After the anodization process, all the samples were rinsed with distilled water and dried at room temperature.

2.1.2　　　Surface Characterization

The surface morphology of the non-anodized (NA) and anodized 316L SS surfaces were investigated by scanning electron microscope (SEM, FEI Nova Nano 430) equipped with a secondary electron detector. For analysis of the nanofeature dimensions, the measurements were completed from 30 different surface features in triplicate using ImageJ 1.51 software (National Institute of Health). Atomic force microscopy (AFM, Veeco, Multimode V) was used to characterized nanoscale roughness of the samples. Surfaces were scanned in tapping mode using a silicon AFM tip having a 10 nm radius. For each sample, 1×1 μm^2 fields were analyzed at a rate of 1 Hz. The AFM data were analyzed using Image Plus software. The micron-scale roughness values of the samples were measured using a profilometer (MarSurf PS 10) from at least three different locations. The hydrophobicity of the samples was characterized using a goniometer (EasyDrop, KRÜSS GmbH). Ultrapure water (8 μL) was dropped onto each sample and sessile drop water contact angles at the sample interface were measured. Chemical composition of the outermost surface oxide layer on 316L SS was characterized with X-ray photoelectron spectroscopy (XPS; PHI 5000 Versa Probe) equipped with a monochromatic Al Kα X-ray source. High resolution spectra of the Cr 2p, Fe 2p, O 1s, and C 1s peaks were obtained. C 1s peak was used as reference and set at 284.8 eV. Curve fitting of peaks were performed with XPSPeak 41 software.

20

2.1.3 Cytotoxicity Testing

Human osteoblasts (hFOB 1.19, ATCC CRL-11372) were cultured using Dulbecco's Modified Eagle's Medium (DMEM, Sigma-Aldrich) supplemented with 10% fetal bovine serum (FBS, Sigma-Aldrich), 1% penicillin− streptomycin (Sigma-Aldrich), and 1% L-glutamine (Sigma-Aldrich) under standard cell culture conditions (37 °C and 5% CO_2). Prior to cell culture, 316L SS samples were sterilized with 70% ethanol for 15 min, followed by UV sterilization for 30 min. 3-[4,5-dimethylthiazol 2-yl]-2, 5-diphenyl tetrazolium bromide (MTT) assay was used to assess cell-surface interactions. hFOBs were seeded onto sterile 316L SS samples at a density of 10^4 cells/cm^2 and cells were cultured up to 5 days *in vitro* under standard cell culture conditions (37 °C and 5% CO_2). After the prescribed time periods, samples were rinsed with 1xPBS and transferred to fresh wells. 500 μL MTT solution (1 mg/ml) was added onto each sample and samples were incubated for 4 hr to form formazan crystals. The formazan product was solubilized in 0.1M HCL solution prepared in isopropanol. 250 μL of the dissolved solution from each sample was transferred to obtain absorbance readings at 570 using a microplate reader (Thermo Scientific Multiskan Go). The absorbance values of samples without cells (blank) were subtracted from the obtained absorbance data. MTT experiments were repeated for three times with three samples in each replicate.

2.1.4 Cellular Imaging

Cellular morphology was assessed both with SEM and immunofluorescence imaging. Prior to imaging, hFOBs seeded onto sterile samples were cultured under standard cell culture conditions (37 °C and 5% CO_2). At the 3rd day of culture, hFOBs were fixed using 4% paraformaldehyde (Sigma-Aldrich) for 20 minutes. For SEM imaging, fixed cells were dehydrated with 30, 70, 90, 95 and 100% (v/v) ethanol for 10 min each. Afterwards, samples were treated with hexamethyldisilazene (Sigma-Aldrich) and left to dry for 12 hr. The dried samples were coated with gold using

sputter coater and the images were captured with SEM (FEI Nova Nano 430). For immunofluorescence imaging, fixed cells were permeabilized with 0.2% Triton X-100 for 30 min and blocked with 5% BSA for 30 min. Actin fibers were stained with phalloidin prepared at a 1:200 dilution factor (Abcam) for 1 h. Nuclei of the cells were stained with a 4′,6-diamidino-2-phenylindole dihydrochloride (DAPI) solution prepared at 1:40 000 dilution for 30 min. Images were captured with a confocal microscope (Zeiss LSM800) and merged with ZEISS ZEN Imaging Software. Quantitative analysis was completed using ImageJ (NIH) in triplicate using three replicates for each experiment.

2.1.5 Cellular Functions

To assess hFOB functions, cells were incubated up to 5 weeks using osteogenic cell medium (DMEM F-12, 10% FBS, 1% L-glutamine, 1% penicillin−streptomycin, 50 µg/mL L-ascorbic acid, 0.01 µM dexamethasone, 10 mM β-glycerophosphate) under standard cell culture condition (37 °C and 5% CO_2). To measure ALP activity, hFOBs were seeded at a density of 2×10^4 cells/cm^2 onto sterile samples. At 2, 3, 4, and 5 weeks of culture, samples were rinsed with 1× PBS and transferred to fresh wells, followed by addition of 400 µL 0.2% Triton X solution for 5 min to lyse the cells. Cell lysates were centrifuged at 14000 rpm for 5 min at 4 °C to collect supernatants. ALP activities were assessed using a commercially available kit (ab83369, Abcam) following the manufacturer's instructions. Absorbance values were obtained using a microplate reader (Thermo Scientific Multiskan Go) at 405 nm. The ALP activity of hFOBs were determined using a standard absorbance - concentration curve of phosphate run in parallel. For alizarin red staining, 3×10^4 cells/cm^2 were seeded onto sterile samples. At 2, 3, 4, and 5 weeks of culture, cells were fixed with 4% paraformaldehyde for 20 min. After rinsing the samples with distilled water, 500 µL of a 40 mM alizarin red solution (pH = 4.2) was added onto each sample and samples were kept for 30 min at 80 rpm. Then, each sample was rinsed with distilled water once more to remove unbonded Alizarin red. Calcium

22

deposited on the samples were visualized with optical microscope (Huvitz). For quantitative analysis, 500 µL of a 10% cetylpyridinium chloride solution prepared in 10 mM disodium phosphate was added onto each sample, followed by mixing the samples in the dark for 1 h at 80 rpm. At the end of 1 h, the absorbance values were measured with a microplate reader (Thermo Scientific Multiskan) at 562 nm. ALP and alizarin red assays were performed in triplicate using three replicates for each experiment.

2.1.6   Anti-Fouling Performance

Bacterial tests were conducted with gram-positive *Staphylococcus aureus* (*S. aureus*, ATCC® 25923™) and gram-negative *Pseudomonas aeruginosa* (*P. aeruginosa*, ATCC® 27853™) to evaluate the anti-fouling properties of samples. Bacteria were taken from the stock culture and streaked onto a tryptic soy broth (TSB) agar plate. After 24 hr, a single colony from the agar plate was inoculated into 3% TSB and incubated at 37°C for 18 hr at 200 rpm. *S. aureus* and *P. aeruginosa* bacterial suspensions were prepared according to 0.5 McFarland standards, and then further diluted 1:100 with 1xPBS prior to seeding. 0.5 ml bacteria solution was added onto each sample and bacteria were allowed to adhere for 1 hr. After 1 hr, samples were gently rinsed with 1xPBS, transferred to fresh wells and incubated with 0.3% TSB at 37°C up to 24 hr. At 1, 4, 12 and 24 hr of culture, samples were transferred to sterile tubes containing 1xPBS. Each sample was vortexed for 90 seconds to detach bacteria from the sample surfaces into the PBS solution. Afterwards, PBS solution containing the bacteria were serially diluted, followed by plating 20 µL of each dilution onto agar plates. After 18 h of incubation, the number of colonies on the agar plates was counted and reported per milliliter of bacteria solution for each sample. To visualize the adherent bacteria, samples inoculated with *S. aureus* or *P. aeruginosa* were gently rinsed with 1xPBS at 4 and 24 hr of culture. SEM imaging protocol detailed in section 2.4 was followed.

Biofilm formation on samples was evaluated by crystal violet (CV) staining. Similar bacteria seeding and culture protocol were followed. After 24, 48 and 72 hr of incubation, media on the samples were aspirated. Afterwards, the samples were washed 1xPBS and transferred to fresh wells. Biofilm were stained with 500 µL 0.1% CV solution for 15 min. Once staining was completed, CV solutions were aspirated and the samples were gently washed three times with 1xPBS. Once samples were dry, 500 µL ethanol (99%) solution was added for 15 min to dissolve CV dye staining the biofilm. Optical density values were measured at 562 nm.

2.1.7   Statistical Analysis

The SPSS software was used for the statistical analysis. One-way analysis of variance (ANOVA) with Tukey's test was performed for data analysis. $p < 0.05$ was considered statistically significant.

2.2   Results and Discussions

2.2.1   Surface Characterization

Figure 2.1a shows the schematic of the electrochemical set-up used for the anodization experiments, where a platinum mesh was used as the cathode and 316L SS samples were the anode. The current-time (I-t) graphs obtained during anodization of 316L SS samples were provided in Figure 2.1b. As evident in the I−t curves, the formation of nanostructured surfaces consisted of three characteristic regions when higher voltages were used. In the first region, current passing through the system decreased swiftly, which was a result of oxide layer formation on the 316L SS surfaces. This was followed by a second region where current passing through the system increased. In the second region, dissolution of the oxide layer started and formation of nanostructures began. Finally, gradual decrease in the current was observed in the third region due to the limited ionic diffusion across the

oxide layer on the surfaces. The formation of three distinct regions on the I-t graph was in-line with literature for anodization of SS samples. In contrast, these three characteristic regions in the I-t graph did not appear when lower voltages were used during anodization. This was primarily due to lower voltages not being able to provide enough driving force for voltage induced oxide layer formation and dissolution mechanisms to dominate over each other at specific regions of the I-t graph. Though oxide layer formation and dissolution mechanisms were still active, three distinct regions were not evident on the I-t graph. After anodization of 316L SS, the surface morphology was verified with SEM (Fig 2.1c-f). It was observed that highly ordered, uniform nanostructures formed on the 316L surfaces. The obtained nanostructures had a dimple-like morphology, and thus these anodized samples were referred as nanodimple (ND) samples. It was observed that the ND size was sensitive to the anodization voltage; as the applied voltage was increased, the feature size of NDs increased, as well. In fact, arrays of NDs having a controlled and uniform feature size ranging from 25 to 250 nm were fabricated by altering the applied voltage (Fig 2.1c-f). Fig 2.1g showed that there was a linear relationship between the applied voltage and the feature size of the nanodimples forming on 316L SS (R^2: 0.98). In this study, we selected 3 different ND sizes for sample characterization to cover both nano and submicron size regimes. The selected ND sizes were 25.3 ± 1.8 nm, 110.8 ± 6.1 nm, and 208.9 ± 12.5 nm, and these samples were referred as ND25, ND100 and ND200, respectively. In addition, the non-anodized 316L SS samples were used as control, and they were referred as NA (Erdogan & Ercan, 2023).
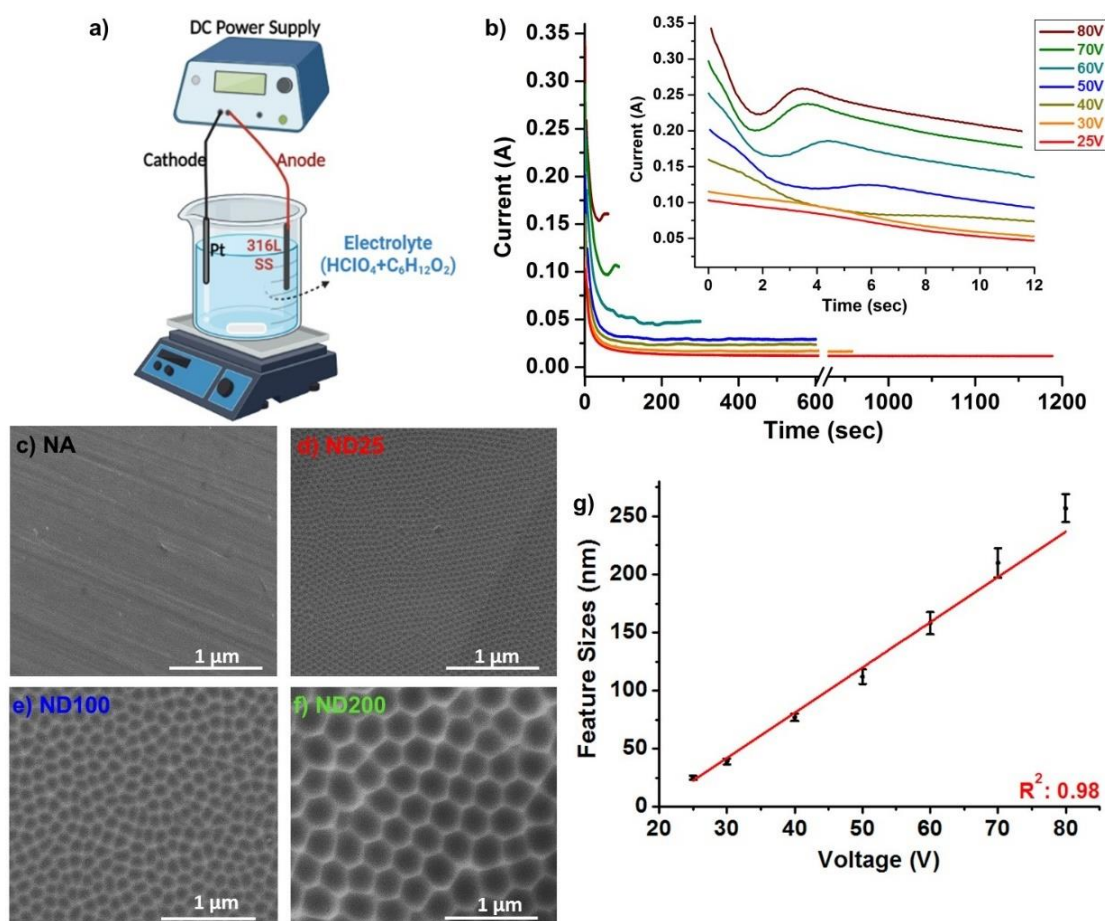
Figure 2.1 a) Schematic of the anodization set-up. b) Current-time graphs obtained during anodization of 316L SS. SEM micrographs of c) NA, d) ND25, e) ND100, and f) ND200 samples. g) ND feature size vs. voltage graph for anodized samples.

Table 2.1 The relation between anodization voltage with duration and the obtained nanofeature size.

Voltage (V)	25	30	40	50	60	70
Duration (min)	20	15	10	10	5	1.5
Nanofeature Size (nm)	25.3 ± 1.8	39.7 ± 2.5	77.5 ± 3.3	110.8 ± 6.1	158.6 ± 9.5	208.9 ± 12.5

Figure 2.2 shows AFM micrographs, and the corresponding roughness profiles across the given lines on the sample surfaces. These figures verified that the anodization process created a unique nanostructured topography on 316L SS surfaces. The root-mean square roughness values (Sq) calculated from the AFM scans were 1.5 ± 0.2, 2.9 ± 0.5, 9.7 ± 1.2 and 20.1 ± 2.1 nm for the NA, ND25, ND100 and ND200 samples, respectively (Table 1). Furthermore, surface areas of the samples were calculated to be 0.94 ± 0.09, 0.97 ± 0.11, 1.10 ± 0.14 and 1.74 ± 0.27 μm^2 for the NA, ND-25, ND-100 and ND-200, respectively (Table 1). It was clear that nanoscale surface roughness and surface area of 316L SS increased upon anodization. In fact, the increase in ND feature size increased both surface roughness and surface area. The ND200 sample had the highest nanoscale roughness ($p < 0.05$) and had the largest surface area ($p < 0.01$) compared to the NA. It should be noted that the surface roughness measurements and area calculations were limited with the resolution of the AFM tip to interact with the dimple shaped nanostructures on the 316L SS surfaces. Thus, surface morphologies could only be partially represented on the AFM micrographs. RMS and calculations represented the lower limit to the RMS of the surfaces. In addition, the roughness profile of the ND structures increased with an increase in ND feature size, which were measured to be around 1 ± 0.3, 16 ± 1.8 and 70 ± 2.6 nm for ND25, ND100 and ND200 surfaces, respectively. However, when micron scale surface roughness was measured, there was no significant difference between ND and NA surfaces (Table 1). These results indicated that anodization process did not change micrometer surface roughness, yet increased the nanoscale roughness of the surfaces.
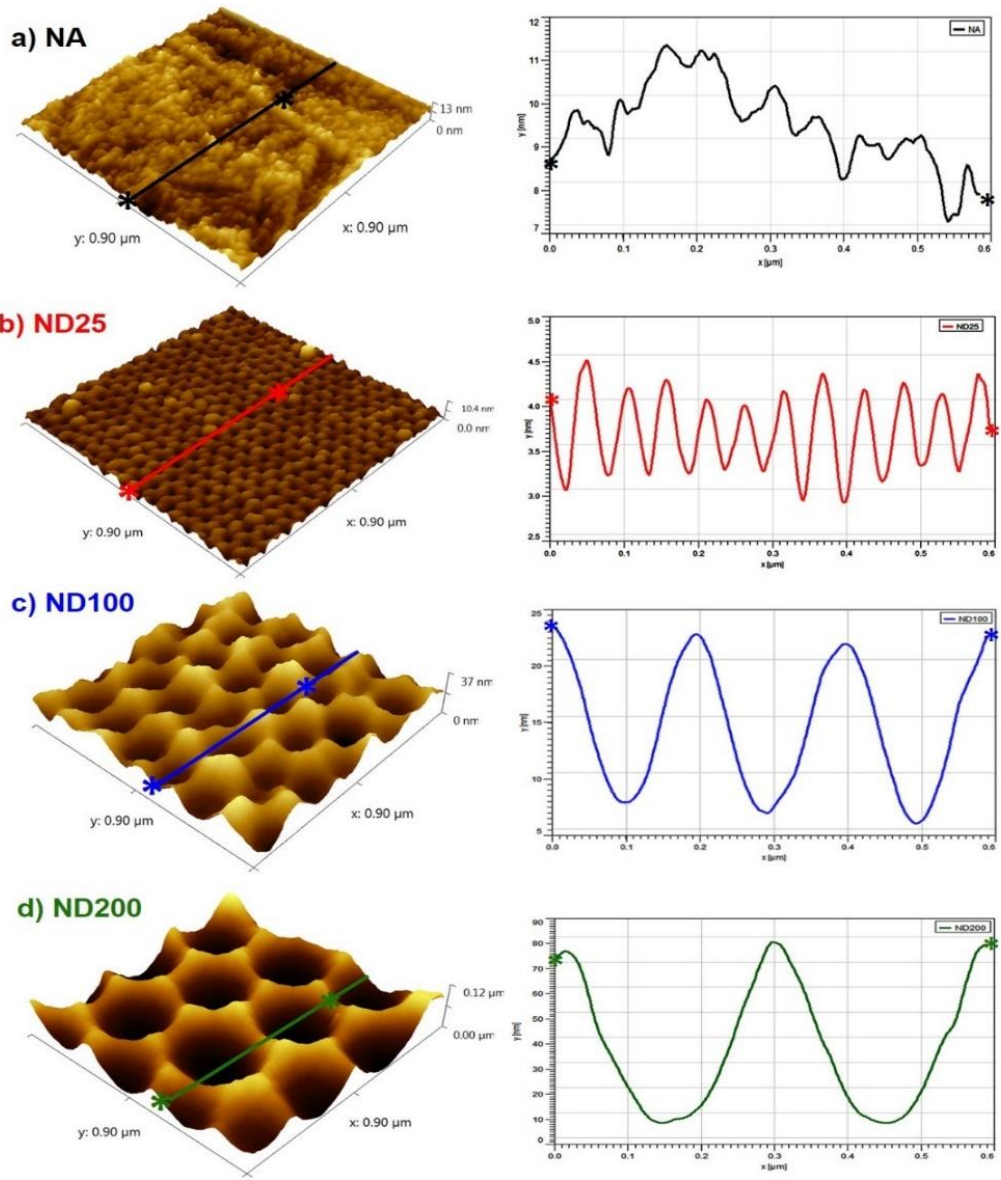
Figure 2.2 AFM images and the corresponding roughness profiles obtained across the highlighted lines for the a) NA, b) ND25, c) ND100, and d) ND200 samples.

Table 2.2 Nano- and micron-scale surface roughness values, surface areas, and sessile drop water contact angles for the NA, ND25, ND100, and ND200 samples. *p < 0.05 and **p < 0.01 compared to NA.

Sample	Surface Nanostructured roughness (Sq)	Surface Micronstrucutred roughness (Ra)	Surface Area (μm^2)	Water Contact Angle (°)
NA	1.5 ± 0.2	0.129±0.004	0.94 ± 0.09	63.6 ± 1.9
ND25	2.9 ± 0.5	0.122±0.006	0.97 ± 0.11	69.7 ± 3.5
ND100	9.7 ± 1.2*	0.126±0.007	1.10 ± 0.14	65.3 ± 3.8
ND200	20.1 ± 2.1**	0.123±0.008	1.74 ± 0.27*	72.6 ± 3.6*

Sessile drop water contact angles value for the samples were given in Table 1. We can assume that all the samples in this study showed hydrophilic characteristics independent of having NDs or not due to the all contact angles values below 90°. On the other hand, ND200 samples had a slightly higher water contact angle compared to NA (p<0.05). This result could be explained with Cassie-Baxter theory, which included the effect of surface roughness on contact angle. Since anodization process created NDs on 316L SS surfaces, it was possible that water did not completely penetrate through the NDs and left some air gaps, which led to an increase in water contact angle value of ND200.

High resolution XPS spectra of NA, ND25 and ND200 samples were provided in Figure 2.3. Curve fitting for chromium peaks (Figure 2.3a) showed that NA surfaces consisted of Cr(0) (metallic chromium), Cr_2O_3, $Cr(OH)_3$ (hydrated chromium oxide) and CrO_3 components and expressed peaks at around 573.8, 575.5, 576.8 and 579.0 eV, respectively. Upon the anodization, Cr(0), Cr_2O_3, $Cr(OH)_3$ and CrO_3 peaks for the ND25 samples slightly shifted to 574.1, 575.9, 577.1 and 579.0 eV, respectively. For ND200 surfaces, Cr_2O_3, $Cr(OH)_3$ and CrO_3 peaks shifted to 575.8, 576.9 and 578.9 eV, respectively (Latifi et al., 2013). The anodization process altered the chemical composition of the outermost layer of 316L SS and led to an increase in

the $Cr(OH)_3$ content for ND25 and ND200 surfaces compared to NA. Changes in the oxidation state of chromium led to higher binding energies in the Cr 2p spectra. Metallic Cr on the surfaces was oxidized during anodization. However, the $Cr(0)$ peak was still apparent for the ND25 surfaces due to lower potentials used during anodization. On the other hand, $Cr(0)$ peak disappeared from the XPS spectrum for the ND200 surfaces, which could be correlated with accelerated oxidation at higher voltages. Similarly, anodization process affected the chemical composition of Fe 2p at the 316L SS surfaces. Figure 2.3b showed curve fitting for Fe $2p_{3/2}$ peaks, where NA surfaces consisted of metallic iron ($Fe(0)$), Fe_2O_3 and FeOOH at 707.0, 710.2 and 711.7 eV, respectively. Upon the anodization of 316L SS, $Fe(0)$, Fe_2O_3 and FeOOH peaks for the ND25 surfaces slightly shifted to 707.2, 710.6 and 712.2 eV, respectively. For the ND200 surfaces, $Fe(0)$, Fe_2O_3 and FeOOH peaks appeared at 707.0, 710.4 and 712.1 eV, respectively. The intensity of the $Fe(0)$ peak decreased on the anodized surfaces compared to the NA surfaces. When peak intensities were compared, the lowest $Fe(0)$ intensity was observed for the ND200 surfaces, followed by the ND25 surfaces and the highest $Fe(0)$ intensity was observed for the NA surfaces. On the other hand, an opposite trend was observed for Fe_2O_3, where the highest Fe_2O_3 intensity was observed for the ND200 surfaces, followed by ND25 surfaces and the lowest peak intensity was observed for the NA surfaces. This result was an indication for oxidation of the metallic Fe and formation of Fe_2O_3 on the surfaces of 316L SS upon anodization. When XPS peaks were carefully investigated, it was observed that anodization reaction led to slight shifts for all of the chromium and iron peaks towards higher binding energies. This could be attributed to the diffusion of oxygen anions into the 316L SS matrix during anodization process. When negatively charged oxygen anions migrate towards positively charged 316L SS anode, their concentration inside the 316L SS lattice increased, which led to higher binding energies for the electrons. In literature, the color change of electrolyte used during anodization was provided as an indirect validation of Fe-oxide layer dissolution during anodization, and our findings were in-line with this assessment. When Cr(oxide+hydroxide) / Fe(oxide+hydroxide) ratios of the surfaces were

30

analyzed, NA surfaces had a ratio of 0.20, while this ratio was 0.44 and 0.48 for ND25 and ND200 surfaces, respectively. This result indicated the formation of chromium oxide and hydroxide, while iron oxide and hydroxide content diminished at the ND surfaces layers. The high-resolution spectrum of O 1s (Fig 2.3c) was curve-fitted with three different peaks at 529.8, 531.2, and 532.4 eV for the NA surfaces and these peaks were assigned to metal-oxides, hydroxides, and adsorbed water, respectively. These peaks on ND25 and ND200 surfaces shifted to 529.9, 531.4 and 532.8 eV. The intensity of the hydroxide peak significantly increased on ND25 and ND200 compared to NA. The hydroxylation degree (OH^-/O^{2-}) was quantitatively analyzed to be 0.91, 1.09 and 1.28 for NA, ND25 and ND200 surfaces, respectively. The overall increase in the OH^- content might provide some negative charge for the ND25 and ND200 surfaces. The increased intensity of $Cr(OH)_3$ peak (Figure 2.3a) supported the formation of hydroxyl groups on the oxide layer (Figure 2.3c). This was related to oxidation and dissolution of Cr under the applied voltages. When voltage was applied, initially chromium-oxide formed on the 316L SS surfaces. Afterwards, this layer dissolved inside the electrolyte to form chromium-hydroxide, whose XPS peak was observed at higher binding energies. Overall, XPS results showed that anodization process changed the surface chemical layer composition, which, might have contributed to the affects biological and antibacterial properties of 316L SS.
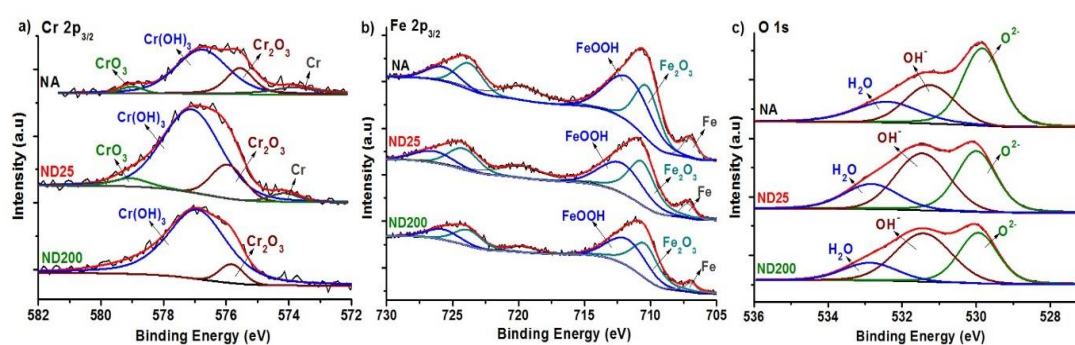
Figure 2.3 High-resolution XPS spectra of the NA, ND25, and ND200 sample surfaces for the a) Cr 2p3/2, b) Fe 2p3/2, and c) O 1s peaks.

2.2.2 Osteoblast Interactions

Figure 2.4 showed that osteoblasts were viable and successfully proliferated on NA, ND25, ND100 and ND200 surfaces up to 5 days *in vitro*. ND200 significantly enhanced hFOB proliferation compared to NA at the 1st and 3rd days of culture (p <0.05). At the end of 5th day, ND200 and ND100 both promoted higher hFOB viability compared to NA (**p<0.01 and *p<0.05). The reason for the increased cellular viability on ND200 could be explained with its unique surface properties. Specifically, ND200 had a higher nanoscale roughness and surface area compared to NA (Table 1). The increased surface area promoted higher osteoblast adhesion, proliferation and viability on ND200. Similarly, nanodimple-like structures on anodized 304L stainless steel promoted osteoblast-like cell viability and functions. However, the aforementioned study did not investigate features less than 100 nm pore size (Dhawan et al., 2017b). Similarly, Ernesto *et al.* reported anodization process increased surface roughness, resulting in enhanced cellular viability on nanostructured titanium surfaces (Partida et al., 2017). SEM micrographs of osteoblasts after 3 days of culture were presented in Figure 2.4b-e. These micrographs demonstrated that hFOB interacted to a greater extend with the ND samples compared to the NA sample. SEM images clearly showed hFOBs expressing more filopodia on ND surfaces compared to NA. Cellular morphology and cytoskeletal organization was also investigated with fluorescence staining (Figure 2.4f-i), where blue dye-stained nuclei and red dye-stained f-actin filaments. Fluorescent microscopy images revealed a well-spread cellular morphology with well-organized f-actin fibers for hFOBs on ND surfaces. Quantitative analysis of hFOB revealed that cells covered a surface area of 1.3 ± 0.1, $2.2 \pm 0.3*$, $2.1 \pm 0.3*$, and $2.2 \pm 0.2*$ (10^{-3} x mm^2/cell) for NA, ND-25, ND-100 and ND-200 samples, respectively. Clearly, osteoblasts spread more on ND samples compared to NA (*p < 0.05). The differences in cell-surface interactions could be attributed to the changes in the surface topography of the ND samples (Pan et al., 2013). It has been suggested in literature that cellular adhesion was sensitive to nanoscale roughness of the

surfaces, which led to enhanced cellular adhesion and proliferation (Hsu et al., 2020; Cho et al., 2021). The existence of numerous filopodia extensions and longer actin filaments on nanodimpled surfaces indicated that nanoscale topography provided a suitable environment for cell-surface interactions.
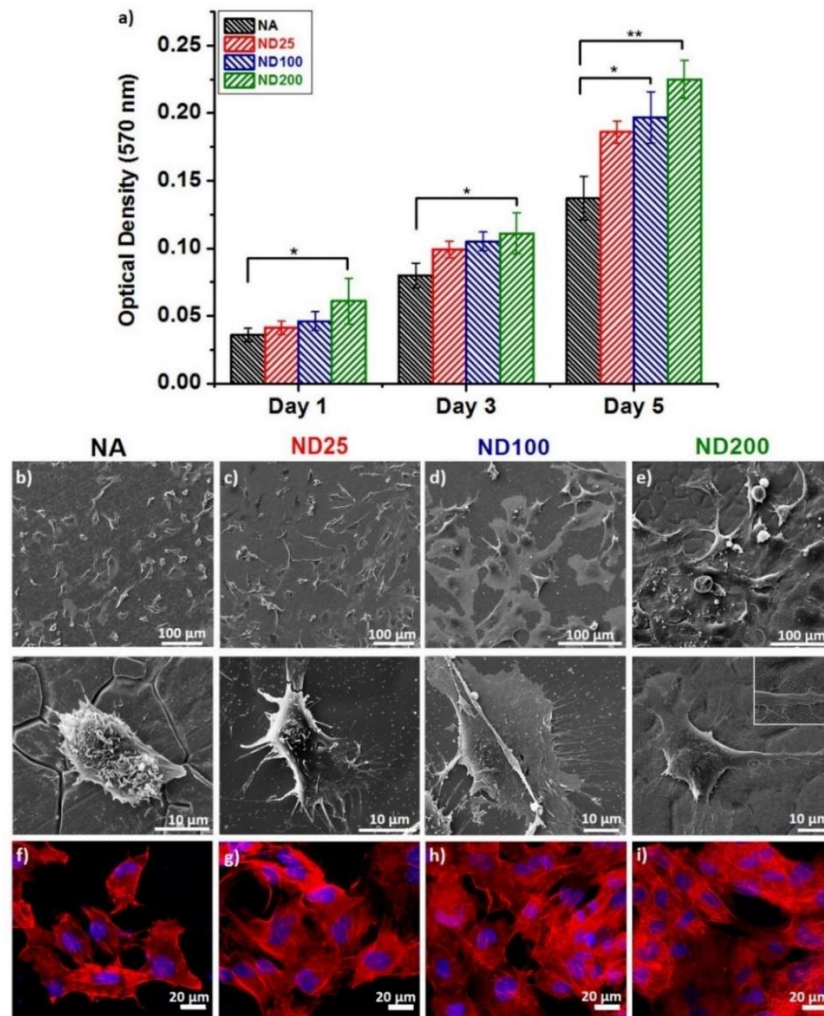
Figure 2.4 a) Osteoblast viability on the NA, ND25, ND100, and ND200 samples up to 5 days *in vitro*. *p < 0.05, and **p < 0.01. (b−e) SEM micrographs of osteoblasts at the third day of culture. (f−i) Nuclei (blue) and f-actin (red)-stained osteoblasts on the (b, f) NA, (c, g) ND25, (d, h) ND100, and (e, i) ND200 samples at the third day of culture.

To investigate hFOB functions on NA, ND25, ND100 and ND200 surfaces, alkaline phosphatase activity (ALP) and calcium mineral deposition assays were completed up to 5 weeks *in vitro* (Figure 2.5). It was observed that at the 2nd and 3rd weeks of culture, hFOBs cultured on ND200 expressed higher ALP activity compared to NA ($p < 0.05$). However, at the 4th and 5th weeks of culture, no difference was observed between the sample groups (Figure 2.5a). ALP played an important role in early bone formation, and it was an early-stage marker to indicate osteogenic differentiation of osteoblasts. This was evident in our results where nanostructured surfaces promoted higher ALP activity at early time points, as it was required for successful bone synthesis *in vivo*. To assess calcium mineral deposition of hFOBs, alizarin red staining was conducted for NA, ND25, ND100, and ND200 surfaces up to 5 weeks *in vitro* (Figure 2.5b). It was observed that mineralization gradually increased with cell culture time after the 2nd week *in vitro*. NA samples consistently had the lowest mineralization at each time point. At the 3rd and 4th weeks of culture, ND200 expressed the highest mineralization compared to NA surfaces ($p<0.01$). At the 5th week of culture, all ND surfaces promoted higher calcium mineral deposition compared to NA ($p<0.05$). The optical microscope images of the Alizarin-Red stained samples demonstrated abundant calcium deposits on ND surfaces at the 3rd week *in vitro*. These images qualitatively confirmed absorbance readings and confirmed higher mineral content (red color) on the ND surfaces compared to NA. Since cellular spreading was shown to promote cellular functions, enhanced ALP activity and calcium mineral synthesis on ND surfaces could be attributed to the well-spread hFOB morphology on ND surfaces (Pan et al., 2013).

Nanoscale topography of the surfaces significantly affect adsorption of RGD peptide bearing proteins, vitronectin, fibronectin, laminin and collagen, which stimulates adhesion and functions of bone cells (Luo et al., 2022; Le et al., 2013). Nanoscale roughness was also correlated with upregulation of osteogenic genes and ensured better interaction between bone and implant (Ni et al., 2020). Our results indicated that the nanostructured surfaces promoted hFOB viability, spreading and functions. Also, nanoscale surface topography of ND surfaces induced higher ALP activity and

calcium mineral synthesis. Since osseointegration of orthopedic implants was initially reliant on bone functions on the implant surfaces, enhanced hFOB viability, ALP activity and mineralization on ND200 could contribute to osteointegration and success of the surgery.
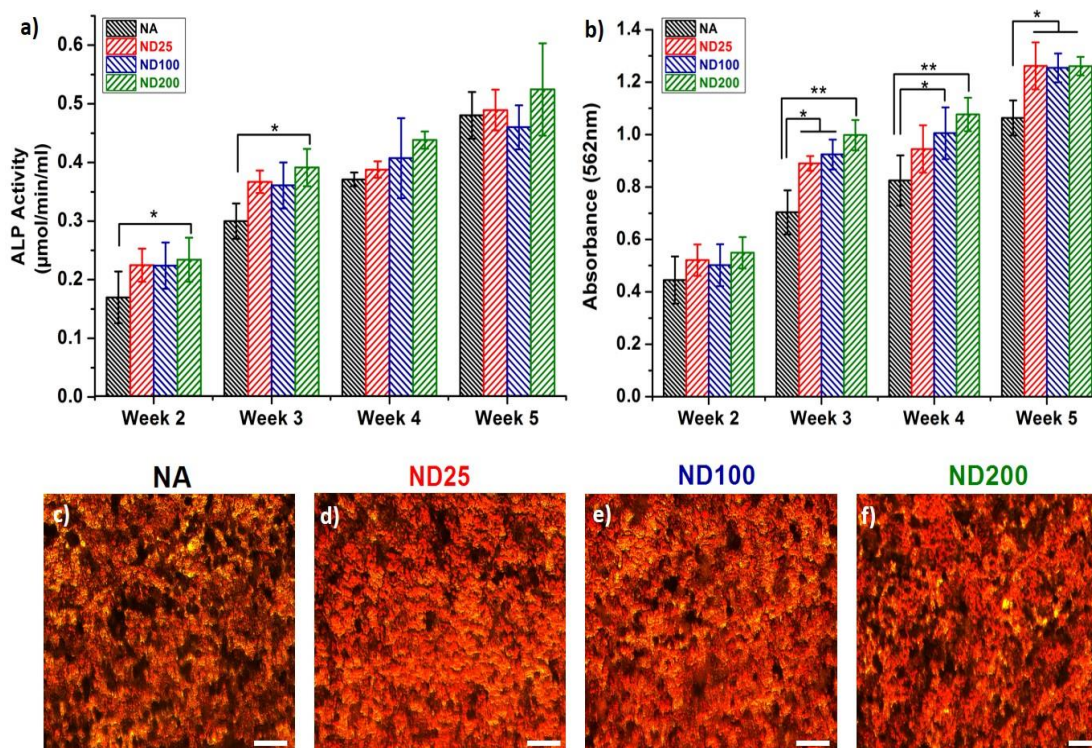
Figure 2.5 a) Alkaline phosphate activity, and b) calcium mineral deposition of osteoblasts cultured on the NA, ND25, ND100, and ND200 samples up to 5 weeks, *p < 0.05 and **p < 0.01. Alizarin red-stained images of the c) NA, d) ND25, e) ND100, and f) ND200 sample surfaces showing deposited calcium minerals at the third week of culture. Scale bars are 50 μm.

2.2.3 Anti-Fouling Properties

Since creating nanostructured topography on 316LSS surfaces enhanced hFOB viability and functions, these surfaces were further investigated to assess anti-fouling behavior of 316L SS. The attachment and growth of *S. aureus* (gram-positive) and *P. aeruginosa* (gram-negative) on the surfaces were assessed by counting colony

forming units (CFUs), as given in Figure 2.6 and 2.7, respectively. After 1 h of incubation, the quantity of adherent *S. aureus* colonies was 61%, 62% and 66% less for ND25, ND100 and ND200, respectively, compared to NA (Figure 2.6a). At 4, 12 and 24 h of culture, *S. aureus* growth on ND200 surfaces was reduced by 78%, 79% and 71%, respectively, compared to the NA surfaces. In addition, *S. aureus* growth on the ND25 surfaces was 57%, 72% and 68% reduced compared to NA surfaces at 4, 12 and 24 h of culture, respectively. For the ND100 surfaces, 62%, 72% and 70% reduction in CFUs was observed after 4, 12 and 24 h of incubation, respectively, compared to the NA surfaces. SEM images confirmed a similar trend that ND200 surfaces limited *S. aureus* growth compared to NA surfaces at 4 and 24h *in vitro* (Fig 2.6(b-e)). Moreover, agar colony counts further confirmed that nanostructured surfaces had less *S. aureus* colonies compared to the NA surfaces (Fig 2.6(f-i)). A similar trend was also observed for gram-negative *P. aeruginosa* growth on nanostructured surfaces. The results showed that ND25, ND100 and ND200 surfaces significantly limited attachment of *P. aeruginosa* by 71%, 70% and 77%, respectively, compared to NA after 1 h of incubation (Figure 2.7a). In fact, after 4, 12 and 24 h of incubation, *P. aeruginosa* colony counts were 88%, 75% and 58% reduced on ND200 surfaces compared to NA surface, respectively. *P. aeruginosa* CFUs on the ND25 surfaces were 86%, 66% and 54% reduced compared to NA surfaces after 4, 12 and 24 h of incubation, respectively. For the ND100 surfaces 84%, 65% and 54% reduction were observed after 4, 12 and 24 h of incubation, respectively, compared to the NA surface. SEM micrographs in Figure 2.7(b-e) further confirmed reduced *P. aeruginosa* growth on ND200 surfaces compared to the NA surfaces at 4 and 24h of culture *in vitro*. It was important to note that our experiments also showed limited biofilm growth up to 72 h on ND200 compared to NA for both bacteria strains (Figure 2.6j and 2.7j). At 24 h of incubation, the biofilms formed by *S. aureus* and *P. aeruginosa* on the ND200 surfaces were reduced by 52% and 31%, respectively, compared to the NA surfaces. At the end of 48 and 72 h, the biofilms formed by *S. aureus* on ND200 surfaces were 27% and 25% less,

respectively, compared to the NA surfaces. Moreover, the biofilm formed by *P. aeruginosa* on ND200 surfaces was 15% less at the end of 48 h compared to NA.
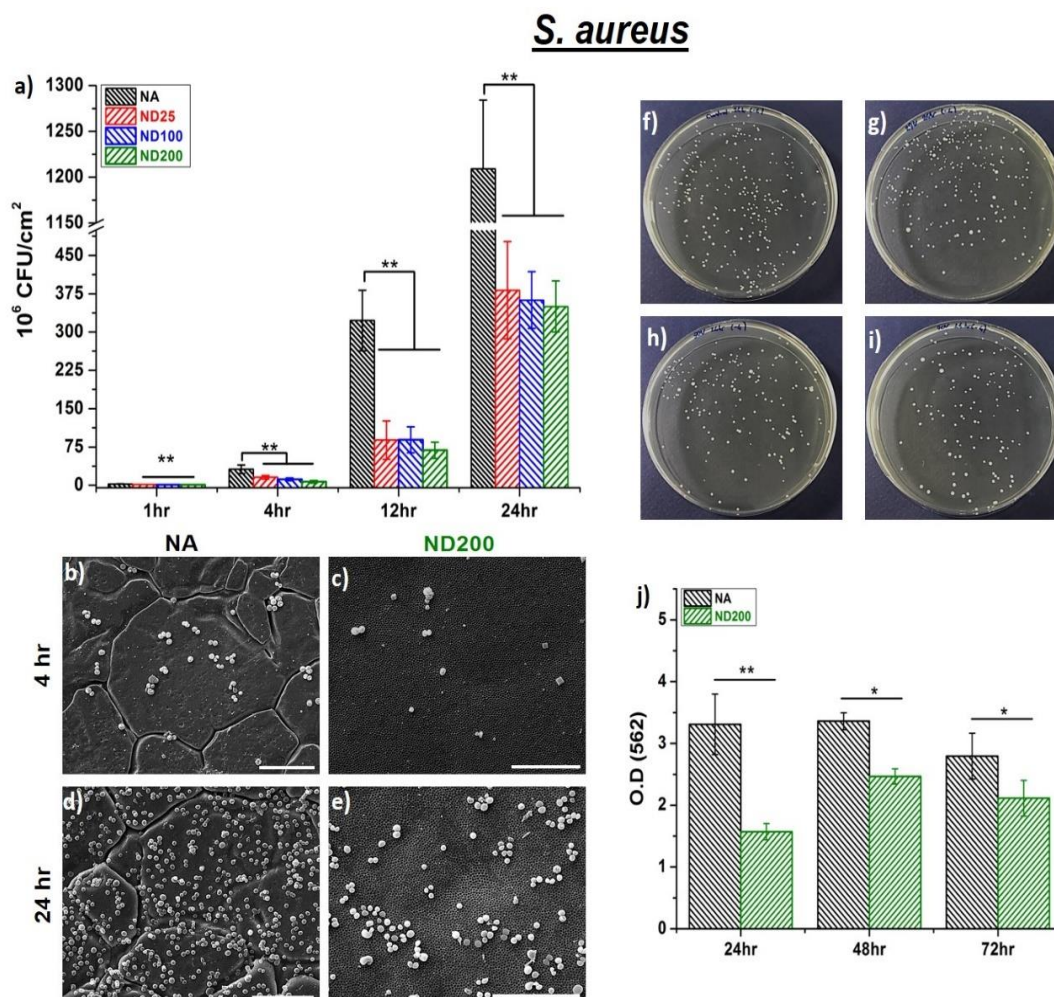
Figure 2.6 a) *S. aureus* colony counts on the NA, ND25, ND100, and ND200 samples. SEM micrographs of *S. aureus* after (b, c) 4 h and (d, e) 24 h of culture on the (b, d) NA and (c, e) ND200 samples. Representative *S. aureus* colonies on the f) NA, g) ND25, h) ND100, and i) ND200 at 24 h of culture. j) *S. aureus* biofilm formation on the NA and ND200 sample, *p < 0.05 and **p < 0.01.

The change in surface properties, such as surface roughness, chemistry, charge and wettability are important to control bacterial attachment and biofilm formation material surfaces (Feng et al., 2014; Cheng et al., 2019). In this study, we observed

that anodization process surfaces clearly played an important role on the anti-fouling properties of 316L SS (L. Liu et al., 2016; Ercan et al., 2011). Though anodization process did not change the micron scale roughness of the 316L SS surfaces, it increased their nanoscale roughness (Table 1). Our results showed that fabrication of nanodimple structures affected bacteria-surface interactions, and decreased bacterial attachment, growth and biofilm formation on the 316L SS surfaces. Nanometer scale surface roughness obtained via anodization had a significant effect of limiting bacterial growth. Our results were in-line with previous findings where nanoscale surface roughness on stainless steel was found to decrease growth of *P. aeruginosa* and *S. aureus* (Wu et al., 2018). In fact, several studies showed that fabricating nanoscale surface features limited bacterial growth despite having greater surface area (Jang et al., 2018; Feng et al., 2014; Singh et al., 2011). For instance, Agbe *et al*. showed that antibacterial efficiency of the anodized aluminum increased linearly with increased pore diameter and surface nanoscale roughness. They informed that 151nm pore size effectively killed 100% of (*E. coli)* (Agbe et al., 2022). The mechanism of action for anti-fouling characteristics for the nanostructured surfaces was closely linked to the nanoscale topography of the samples. It was suggested that bacteria could attach more easily and establish more stable attachments on smooth surfaces compared to rough ones (Wu et al., 2018). Having this said, nanostructured roughness could restrain bacterial attachment by decreasing the contact area between the bacteria and the surfaces. It was proposed that nanostructures on 316L SS led to deformation and stress on the bacterial membranes, and thus samples exhibited bactericidal effect (Jang et al., 2018). In our study, while nanostructured topography caused stress on the bacterial membranes, nanosmooth surfaces (*i.e.* NA) provided higher contact area with bacterial membranes and set the stage for more suitable attachment, which was demonstrated in Figure 2.8. It could also be speculated that anodized samples, despite having a higher total surface area, might actually have less available area for contact between the bacteria and the anodized layer due to having dimple morphology which had relatively deeper regions (Feng et al., 2015). Though bacterial cells, especially gram-

negative bacteria, could still deform, bend and maintain their contact with the underlying surface via their appendages, the dimple morphology might limit cell-to-surface contact area. Thus, it was possible that area available for bacteria to attach on the anodized nanodimpled surfaces might be less than the area calculated with AFM.

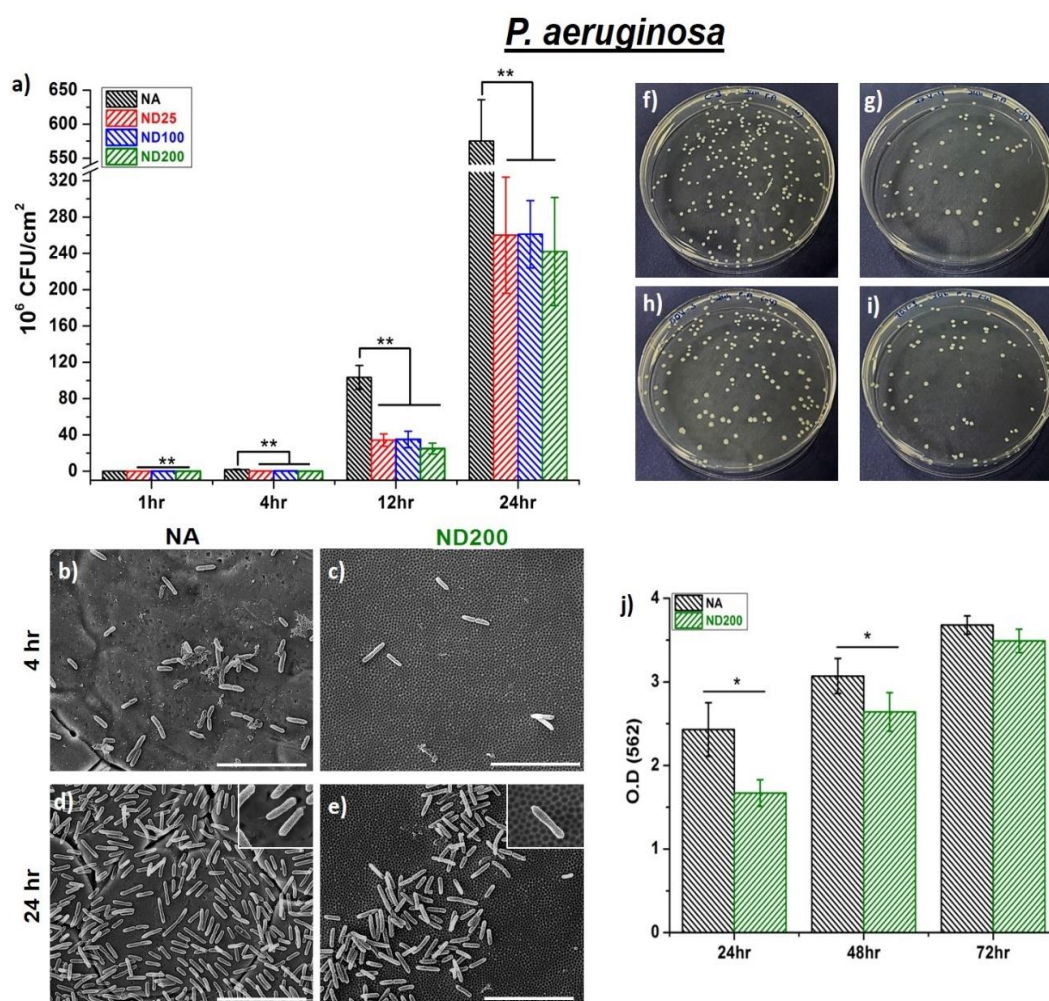**Figure 2.7** a) *P. aeruginosa* colony counts on the NA, ND25, ND100, and ND200 samples. SEM micrographs *P. aeruginosa* after (b, c) 4 h and (d, e) 24 h of culture on the (b, d) NA and (c, e) ND200 samples. Representative *P. aeruginosa* colonies on the f) NA, g) ND25, h) ND100, and i) ND200 samples at 24 h of culture. j) *P. aeruginosa* biofilm formation on the NA and ND200 samples, *p < 0.05 and **p < 0.01.

In addition to the nanoscale topography, surface chemistry of 316L SS also changed during anodization. Changes in the surface chemistry could alter the hydroxylation degree and the surface charge, which might affect bacterial attachment and growth (S. Li et al., 2019). Considering that bacteria possessed negatively charged surfaces due to carboxyl, amino, and phosphate functional groups on their cell membranes, they were expected to adhere more effectively onto positively charged surfaces due to electrostatic interactions (Zheng et al., 2021). Zhu *et al.* showed that *E. coli* and *S. aureus* effectively adhered onto the positively charged surfaces by electrostatic attraction, and as a result proposed negatively charged surfaces to restrict bacterial attachment (Zhu et al., 2015). Research conducted on anodized alumina showed that when the nanopore size on the surfaces decreased, surface area of the samples was increasing, which was enhanced repulsive forces between the surfaces and the bacteria. The increased repulsive forces were, in turn, reducing the bacterial attachment onto the nanostructured surfaces (Feng et al., 2014). Similarly, our results showed that the nanodimple surface topography on the anodized surfaces, independent of the size of the nanodimples, reduced bacterial attachment, growth and biofilm formation compared to the NA surface lacking nanofeatures. In our study, the hydroxylation degree (OH^-/O^{2-}) was increasing for the nanodimple surfaces compared to NA surfaces, which might hint for increased negative charge on the sample surfaces. Additionally, the anodization process was also increasing the total surface area for the ND samples (Table 1). Since ND surfaces had a higher surface area which was also enriched with OH^-, it could be speculated that the negative charge accumulated on the increased surface area of the nanodimple samples might contribute to the anti-fouling properties (Figure 2.8b). Although the anti-fouling effect of negative charges on OH^- could be partially cancelled by the positively charged cations forming metal hydroxide on the anodized surfaces, excess OH^-, if present, might still contribute to the decreased bacterial colonization on the samples.
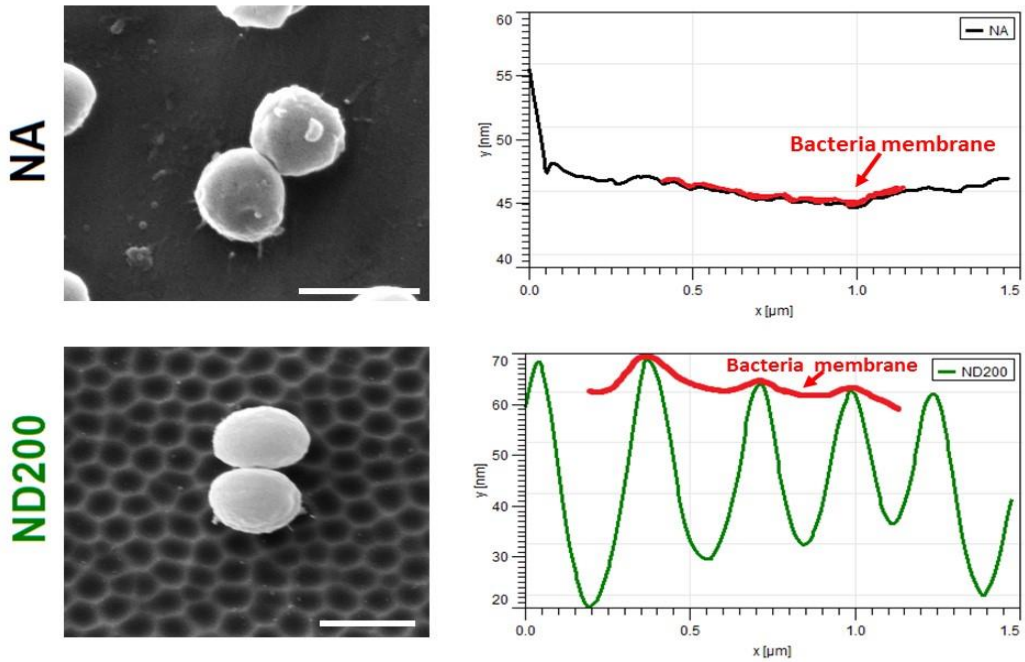
Figure 2.8 Illustration of the potential effect of a) surface topography and b) surface chemistry on bacterial attachment. Topography of the ND200 surfaces could lead to deformation of the bacterial membranes, and at the same time the negative surface charge of the ND200 samples restricted bacterial attachment. Scale bars are 1 μm.

To sum up, electrochemical anodization of 316L SS created a uniform array of surface features having nanodimple morphology. Fabrication of nanostructured surface topography on 316L SS great affected hFOB viability and bacterial growth. Nanofeatured surfaces proved to be conducive to the proliferation and mineralization

of bone cells *in vitro*, and has the potential to promote early osseointegration. Additionally, creating nanodimple morphologies having 200nm feature size on 316L SS surfaces provided anti-fouling properties that decreased *S. aureus* and *P. aeruginosa* growth *in vitro*. To the best of our knowledge, this is the first-time nanostructured surfaces topography on anodized 316L SS surfaces was demonstrated simultaneously to upregulate hFOB functions, while limiting both *S. aureus* and *P. aeruginosa* biofilm formation. According to these results, we suggest that anodization of 316L SS implant surfaces is a simple, cost-effective and efficient methods to remedy bioinert nature and septic failure of 316L SS based orthopedic implants, and nanodimple morphologies having 200nm feature size on 316L SS was promising for bone tissue engineering applications.

CHAPTER 3

FABRICATION NANOSTRUCTURED 316L SS FOR CARDIOVASCULAR STENT APPLICATIONS: IMPROVED CORROSION RESISTANCE AND ENHANCED *IN VITRO* ENDOTHELIZATION AND HEMOCOMPATIBILITY

Nowadays, many researchers focus on surface engineering approaches to modify stent surfaces to improve corrosion resistance and enhance rapid endothelization. However, there is still a crucial gap in addressing the need for effective solutions to promote rapid endothelization, prevent stent restenosis, and ensure optimal hemocompatibility. In this study, oxide based nanostructured 316L SS surfaces having two distinct surface morphologies, which were nanodimples (NDs) and nanopits (NPs), and controlled feature sizes from 25 to 200 nm were fabricated by anodization onto 316L SS surfaces. Afterwards, the surface morphology, topography, ion release, corrosion behavior and surface chemistry of nanostructured samples were characterized. Subsequently, the interaction of HUVEC cells with the nanostructured samples were investigated. The results demonstrated that the nanostructured surfaces exhibited improved endothelization, enhanced cellular migration, and promoted HUVEC functions, such as nitric oxide and prostaglandin production, while restricting the expressions of VCAM and ICAM genes. In addition, nanostructured surfaces exhibited reduced platelet adhesion and hemolysis compared to the bare 316L SS surfaces.

3.1   Materials and Methods

Austenic 316L SS foils (0.5mm) were prepared to have 1 x 1 cm^2 sized squares and ultrasonically cleaned in acetone, ethanol and distilled water each for 10 minutes, respectively. Anodization was conducted using a two-electrode configuration connected to a DC power supply (Genesys 300V/5, TDK Lambda). Platinum was used as the cathode while the sample was used as the anode. The electrolyte was

stirred at 4 rpm using a rotating magnet. Anodization experiments were carried out at temperatures lower than 6 °C. The samples were anodized using 7.5 vol % perchloric acid ($HClO_4$, 70%) in ethylene glycol monobutly ether solutions to fabricated nanodimple morphologies. To fabricated 25 and 200nm feature sized nanodimple surfaces, 27V was applied for 20 min and 70V was applied for 90 sec, respectively. To fabricated the nanopit morphologies, nanodimpled samples were anodized in 0.4 M sodium dihydrogen phosphate solution at 20V for 15 min. After the anodization process, all the samples were rinsed with distilled water and dried at room temperature.

3.1.1   Surface Characterization

The morphology of surfaces was investigated by scanning electron microscope (SEM, FEI, Nova Nano 430) equipped with a secondary electron detector and accelerating voltage was kept at 10 kV. For analysis of the feature size, the at least 50 different surface features from each sample were measured using the ImageJ 1.51 software (National Institute of Health, Bethesda, MD), and the experiments were conducted in triplicate. The surface roughness of samples was characterized by atomic force microscopy (AFM, Multimode V, Santa Barbara). The surface topography was obtained in "tapping mode" and 4×4 μm^2 fields were analyzed at a scan rate of 1 Hz. The AFM data of the samples were analyzed using Image Plus software (Peseux, Switzerland). The surface hydrophobicity of the samples was analyzed with sessile drop water contact angle using a goniometer (EasyDrop, KRÜSS GmbH, Germany). Ultrapure water (8 µL) was dropped onto each sample and then water contact angles on the sample interface were measured. The surface charge of the samples was measured as streaming potential with electrokinetic analyzer (SurPASS, Anton Paar). The pH value was kept 7.4 during the analysis. In order to calculate the zeta potential of samples, Helmholtz-Smoulchowski equation was used. Chemical composition of the outermost surface layer of the samples were characterized with X-ray photoelectron spectroscopy (XPS; Thermo Scientific)

equipped with a monochromatic Al Kα X-ray source. High resolution spectra of the Cr 2p, Fe 2p, Ni 2p, O 1s, and C 1s peaks were analyzed. C 1s using as reference peak and set at 284.8 eV. Curve fitting of the peaks were performed with XPSPeak 41 software.

3.1.2   Electrochemical Polarization and Ni Ion Release

Electrochemical corrosion of the samples was carried out in a EuroCell (Gamry) kit using a potentiostat system (Reference 1010E, Gamry). A conventional three-electrode cell system comprising of the SS samples as the working electrode, Ag/AgCl electrode as the reference electrode, and a graphite rod as counter electrode was used in this study. The open circuit potential (OC) was conducted for 1 hour in order to reach a steady state condition. Potentiodynamic current−potential curves were swept from −0.25V to 0.25V at a scan rate of 0.16 mV/s. Electrochemical impedance spectroscopy (EIS) measurements were performed using AC amplitude of ±10 mV and an applied frequency ranging from 0.2 Hz to 100 kHz. Electrochemical results were repeated three times to ensure the repeatability of the experiments. Corrosion potential (E_{corr}), corrosion current density (I_{corr}) and impedance fittings were determined using Gamry Echem Analyst software.

3.1.3   HUVEC Cell Culture

Human umbilical vein endothelial cells (HUVECs, ATCC-CRL1730) were cultured using Dulbecco's modified Eagle's medium (DMEM, Sigma-Aldrich) supplemented with 10% fetal bovine serum (FBS, Sigma-Aldrich), 1% penicillin− streptomycin (Sigma-Aldrich, St. Louis, MO), and 1% L-glutamine (Sigma-Aldrich, St. Louis, MO) under standard cell culture conditions (37°C and 5% CO_2). Before cell culture experiments, 316L SS samples were sterilized with 70% ethanol for 10 min, followed by exposing both sides of the samples to UV radiation for 30 min.

To assess cell proliferation, 3-(4,5-Dimethylthiazol-2-yl)-2,5-diphenyl tetrazolium bromide (MTT) assay was used. HUVECs were seeded onto sterile 316L SS samples at a density of 2×10^4 cells/cm^2 and cultured up to 5 days *in vitro*. After 1st, 3rd and 5th days of culture, the samples were rinsed with 1xPBS and transferred to fresh wells. Then, 400 µL MTT solution (1 mg/ml) was added onto each well and incubated for 4 hr to form formazan crystals. Afterward, the formazan crystals were dissolved in 0.1M HCl solution in isopropanol (400 µL/well). A 200 µL of the dissolved solution from each sample was transferred 96 wells, and their absorbance values were reading at 570 nm using a spectrophotometer (Thermo Scientific, Multiskan Go). MTT experiments were performed for three times with three replicates for each run.

3.1.4 Cellular Imaging

Cellular morphology of HUVECs were assessed with fluorescence staining. F-actin, vinculin and DAPI staining procedures were applied to observe the cytoskeleton, focal contacts and nuclei of the cells for each sample, respectively. HUVECs were seeded onto sterile 316L SS samples at 1×10^4 cells/cm^2 and incubated for 72 hr. After 72 hr, culture media were aspirated and the samples were rinsed with 1xPBS. Then, HUVECs were fixed with 4% paraformaldehyde for 20 min at room temperature. Then, the fixed cells were rinsed 1xPBS, and permeabilized with 0.2% Triton X-100 for 30 min and blocked with 5% BSA solution for 30 min. The permeated cells were initially incubated with anti-vinculin primary antibody (rabbit monoclonal, 1:200) for 90 min, followed by adding Alexa Flour 488 conjugated secondary antibody (goat anti-rabbit IgG, 1:1,000) to target the primary antibody for 60 min. Afterwards, actin fibers were stained with red fluorescence phalloidin (1:200) for 60 min. Finally, DAPI solution (0.5% BSA in 1×PBS, 1:40,000) was added onto the samples and incubated for 30 min. Cellular images were captured with a Leica DM2500 microscope (Wetzlar, Germany) at 20x magnification using appropriate cubes and filters for each stain.

HUVECs morphologies also evaluated with SEM imaging. HUVECs were seeded at 5×10^3 cells/cm^2 onto 316L SS samples and incubated for 3 days *in vitro*. After 3 days, HUVECSs were fixed using 4% paraformaldehyde for 10 minutes and dehydrated with 30, 70, 90, 95 and 100% (v/v) ethanol for 10 min each. Afterward, the samples were treated with hexamethyldisilazene (Sigma-Aldrich) and left to dry for 12 hr. The dried samples were coated with gold using sputter coater and the images were captured with SEM.

3.1.5 Scratch Assay

For analysis of HUVECs migration on the surfaces, a scratch assay was performed. Cells at a density of 1×10^5 cells/cm^2 were seeded on the samples and waited 24 hr to reach confluency. Afterward, the cell layer was carefully scratched using a plastic pipette. Then, the cells were cultured for 4, 8, 12 and 24 h in standard cell culture conditions (37°C and 5% CO$_2$). At the end of each time point, all specimens were rinsed with 1xPBS and transferred to a new 24-well plate. Then, cells were fixed with 4% paraformaldehyde for 10 minutes and dehydrated with 30, 70, 90, 95 and 100% (v/v) ethanol for 10 min each. Dehydrated cells were treated with hexamethyldisilane (HMDS, Sigma-Aldrich), and left to dry. The dried samples were coated with gold using sputter coater and the images were captured with SEM. The wound healing areas were measured by ImageJ 1.51 software. The measurements were performed in triplicate for each time point.

3.1.6 HUVEC Cell Functions and Gene Expressions

The nitric oxide (NO) synthesis level of HUVECs cultured on samples up to 3 days were detected from the culture medium using a Nitric Oxide Assay Kit (Abcam, ab65328) according to the manufacturer's protocols. Briefly, the nitrate was catalyzed with nitrate reductase into nitrite. Then, total nitrite was converted into a deep purple azo compound using Griess reagents. The absorbance of the purple azo

compound was measured at 540 nm, which was directly proportional to NO production. The prostaglandin synthesis level of HUVECs cultured on samples were quantitative detected from culture medium using a Prostaglandin E2 ELISA kit (Abcam, ab133021) according to protocols. A mouse IgG antibody has been precoated onto 96-well plates. For each sample, 100 µL of cell medium were added to the wells and incubated at room temperature on a plate shaker for 2 hours at 500 rpm that along with an alkaline phosphatase conjugated Prostaglandin E2 antibody. After incubation, excess reagents were washed, pNpp substrate was added and catalyzed to produce a yellow color solution. Finally, 50 µL stop solution was added to all the wells, and the absorbance of solutions were measured at 405 nm. The intensity of the yellow coloration is inversely proportional to the amount of Prostaglandin E2 captured in the plate. The levels of ET-1 from cell culture medium were measured by ELISA kit (Abcam, 133030) according to protocols. Briefly, 100 µL of each standard and sample culture medium were added to the wells and incubated 1 hr. After washing each well for 5 times, 100 µL of endothelin-1 antibody was added and incubated 30 min. Then, substrate solution was incubated for 30 min, and a stop solution was added into each well. The absorbance of the solutions was measured at 450 nm.

The expression levels of angiogenesis genes were quantitatively analyzed by quantitative real-time polymerase chain reaction (qRT-PCR). Cells were seeded on the specimens (20 mm × 20 mm × 0.5 mm) in 6-well plates at a density of 1×10^6 cells/well and cultured for 1, 3 and 7 days. After each time point, the cells on samples were collected using trypsin and the solutions were centrifuged at 2.000 rpm to obtained specific cells. Then, total RNA was isolated from the cells using High Pure RNA Isolation Kit (Roche Diagnostics) following the manufacturer's instructions. The isolated pellets were treated with RNase-free DNase (DNase I; Roche Diagnostics) to prevent genomic DNA contamination. The quantity and quality of the isolated RNA from each sample were measured spectrophotometrically at 260 and 280 nm using NanoDrop 1000 (Thermo Scientific). Subsequently, 1 µg of total RNA from each sample was reverse transcribed with random hexamers using

Transcriptor First Strand High Fidelity cDNA Synthesis Kit (Roche Diagnostics) according to the manufacturer's protocol. The qPCR analysis was performed using LightCycler® 480 instrument (Roche Diagnostics) to assess the expression levels of vascular cellular adhesion molecule-1 (VCAM-1), platelet endothelial cell adhesion molecule-1 (PECAM-1) and intercellular adhesion molecule-1 (ICAM-1). The expression levels of the target genes were normalized to the mRNA level of the beta-actin gene. The qRT-PCR conditions were as follows: an initial denaturation at 65 °C for 10 min, followed by 50 cycles of 95 °C for 10 s and 60 °C for 20 s, and then the samples were cooled to 40 °C. The expression levels of target genes were quantified using the $2^{-\Delta\Delta CT}$ method. Gene expression experiments were repeated three times, with three samples used for each experiment.

3.1.7 Hemocompatibility Tests

The blood compatibility of the specimens was performed according to the standard protocol (ISO 10993-4). The fresh blood from a healthy volunteer was collected in 3.8 wt% citric acid sodium containing tubes. In the hemolysis experiments, the blood was centrifuged for 15 min at 1,500 rpm to isolate the red blood cells. Then, the red blood cells were collected and diluted into 2% suspension using 0.9% physiological saline. A 3 ml red blood cell suspension was added on each sample group, and incubated at 37°C for 1 h. Afterwards, the suspensions were centrifuged for 5 min at 3,500 rpm. A 200 μl supernatant was transferred into a 96-well plate to measure the absorbance at 450 nm using a spectrophotometer. The 2% red blood cell suspension in the physiological saline and the distilled water were used as the positive and the negative control, respectively. The hemolysis rate was calculated according to the following equation:

$$\text{Hemolysis rate (\%)} = \frac{\text{Sample Absorbance} - \text{Negative Absorbance}}{\text{Positive Absorbance} - \text{Negative Absorbance}} \text{ x } 100$$

For the platelet adhesion experiments, the blood was centrifuged for 15 min at 1,500 rpm to obtain the platelet-rich plasma (PRP). Then, 200 μl of the PRP was added

onto each sample, and incubated at 37°C for 1 h. After incubation, the samples were gently rinsed with 1xPBS and the adhered platelets on surfaces were fixed using 4% paraformaldehyde (Sigma-Aldrich) for 10 minutes. The samples were subsequently dehydrated in 30, 70, 90, 95 and 100% ethanol solutions each for 10 min, respectively. Afterwards, the samples were treated with hexamethyldisilane (Sigma-Aldrich) and left to dry. The dried samples were coated with gold using sputter coater and distribution and morphology of the platelets were observed with SEM.

The research on human blood was approved by the Clinical Research Ethics Committee at Dıskapı Yıldırım Beyazıt Training and Research Hospital, Ministry of Health in Republic of Turkey (2021/106/34), and informed consent was given by all blood donor participants.

3.2   Results

3.2.1   Surface Properties

The surface morphology of the anodized samples is displayed in Fig 3.1a-e. SEM images showed that nanodimple and nanopit structures were obtained on the sample surface by anodic oxidation. When 316L SS foil was anodized at 27V for 15 min and 70V for 90 sec, 25 and 200 nm sized nanodimples were fabricated on the samples, respectively. Then, we applied a second step anodization process for these two nanodimpled samples to obtain the nanopit morphology, whose feature size was controlled to be 25nm and 200 nm on the surface. SEM images confirmed that feature sizes of the nanostructured surfaces increased in parallel with an increase in the applied voltage (Fig 3.1b-c). On the other hand, the nanostructured morphology on surface depended on the electrolyte type. In this research, samples having 25 nm sized nanodimples, 200 nm sized nanodimples, 25 nm sized nanopits and 200 nm sized nanopits are referred as ND25, ND200, NP25 and NP200, respectively. Also, control surface is named as non-anodized (NA) sample.

AFM 2D micrographs and the corresponding roughness profile of the samples are displayed in Fig 3.1f-j. According to the AFM analysis, nanostructured roughness values were measured as 3.1 ± 0.1, 3.4 ± 0.1, 23.2 ± 0.3, 17.5 ± 0.3 and 21.6 ± 0.2 nm for the NA, ND25, ND200, NP25 and NP200 samples, respectively. Moreover, surface areas of the samples were calculated to be 4.1 ± 0.1 for NA, 4.2 ± 0.1 for ND25, 4.8 ± 0.1 for ND200, 4.5 ± 0.1 for NP25, and 4.9 ± 0.1 for NP200 samples. AFM measurements affirmed formation of unique nanostructured surface topography, which was significantly altered upon the anodization process. Contact angle values of NA, ND25, ND200, NP25 and NP200 samples were measured to be $60.8 \pm 5.1°$, $73.5\pm 4.9°$, $81.5\pm 4.5°$, $34.6\pm 6.4°$ and $21.7\pm 3.5°$, respectively. The nanodimpled surfaces had a higher, whereas the nanopit surfaces had a lower water contact angle compared to the non-anodized surfaces.
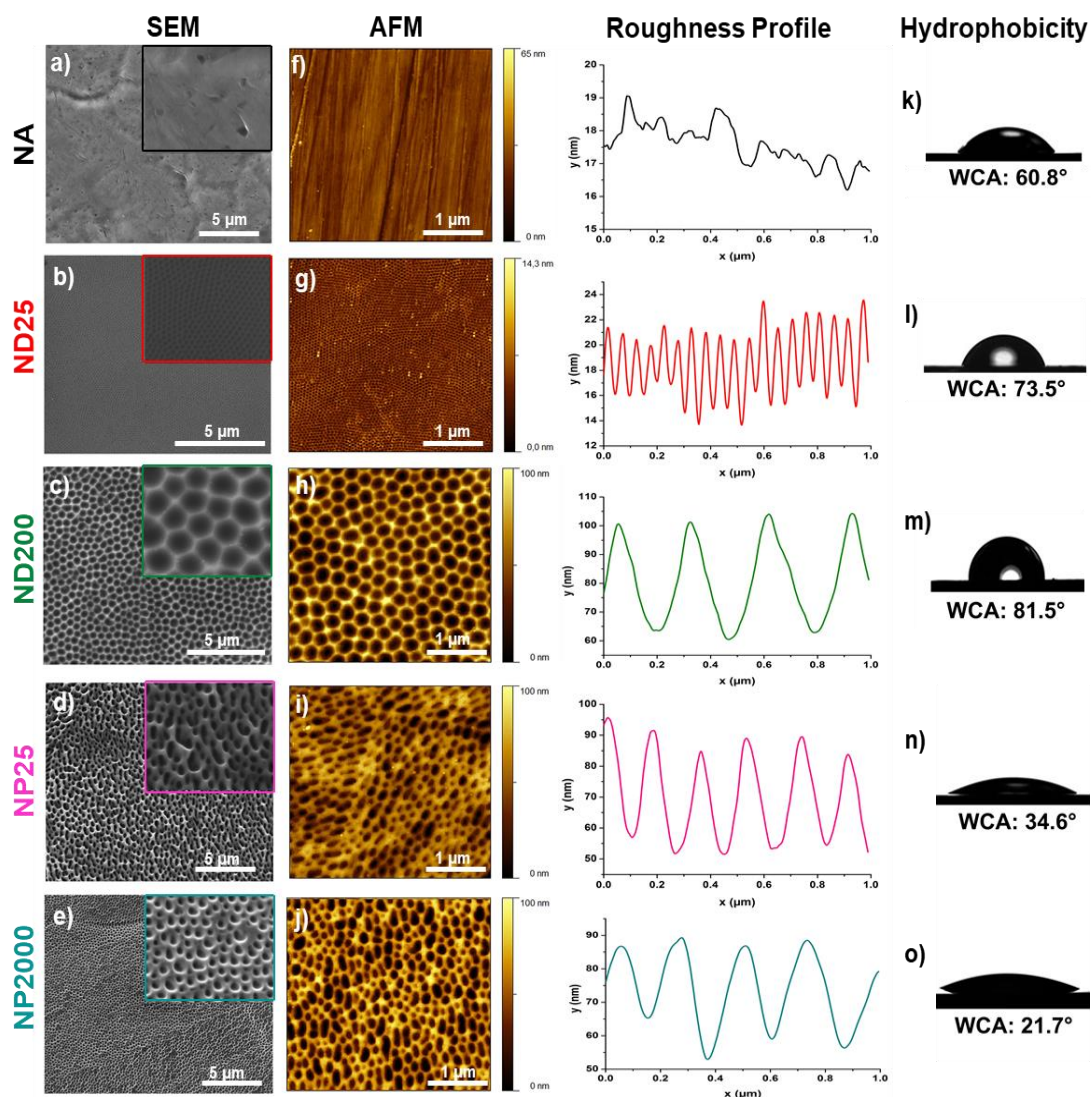
Figure 3.1 (a–e) SEM micrographs, (f-j) atomic force microscopy images and the corresponding roughness profiles obtained across the highlighted lines for the (a, f) NA, (b, g) ND25, (c, h) ND200, (d, i) NP25 and (e, j) NP200 samples. The water contact angles for the k) NA, l) ND25, m) ND200, n) NP25, and o) NP200 samples.

Table 3.1. Nano-scale surface roughness values, surface areas and water contact angles of the samples, $*p < 0.05$ and $**p < 0.01$ compared to NA.

	Surface Nano roughness (S_q, nm)	Surface Area (μm^2)	Contact Angle (º)
NA	3.1 ± 0.1	4.1 ± 0.1	60.8 ± 5.1
ND25	3.4 ± 0.1	4.2 ± 0.1	73.5 ± 4.9
ND200	$23.2 \pm 0.3**$	$4.8 \pm 0.1**$	$81.5 \pm 4.5*$
NP25	$17.5 \pm 0.3**$	$4.5 \pm 0.1*$	$34.6 \pm 6.4**$
NP200	$21.6 \pm 0.2**$	$4.9 \pm 0.1**$	$21.7 \pm 3.5**$

The high resolution XPS spectra of the Cr $2p_{3/2}$ peaks for the non-anodized and anodized 316L SS samples are displayed in Figure 3.2. The results showed that surface chemistry was changed after the anodization process. The $2p_{3/2}$ peaks of Cr_2O_3 appeared at 576.37 eV for the NA samples, while it appeared at 576.89, 576.89 eV, 577.25 and 576.75 eV for the ND25, ND200, NP25 and NP200 samples, respectively. It was detected that the Cr_2O_3 peak intensity increased on the nanostructured surfaces compared to the non-anodized surface. Moreover, a new CrO_3 peak was observed on the nanostructured samples after anodization. This CrO_3 peak appeared at 578.5, 578.5, 579.7 and 579.3 eV for the ND25, ND200, NP25 and NP200 samples, respectively. The high resolution XPS spectra of the Fe $2p_{3/2}$ peaks for the non-anodized and anodized 316L SS samples are displayed in Figure 3.3. Analysis of the Fe $2p_{3/2}$ analysis showed that all samples contained FeOOH, Fe_2O_3 and metallic iron. The intensity of the metallic iron peak decreased on the nanostructured surfaces compared to the NA surfaces. The Fe_2O_3 peak was observed at 710.4 eV for the NA sample, while it was observed at 711.2, 710.7, 711.4 and 710.5 eV for the ND25, ND200, NP25 and NP200 samples, respectively. Upon careful investigation of the XPS peaks, it was observed that the anodization reaction caused slight shifts for all of the chromium and iron peaks toward higher binding

energies. This phenomenon could be attributed to the diffusion of oxygen anions into the 316L SS matrix during the anodization process. When we analyzed nickel components, metallic nickel and NiO peaks appeared at 852.8 and 855.4 eV, respectively, for the non-anodized sample, as shown in Figure 3.4. On the other hand, the metallic nickel peak disappeared completely and NiO peaks appeared at 856.2, 856.6 and 855.8 eV for the ND200, NP25 and NP200 samples, respectively. However, the ND25 surface consisted of metallic nickel (853.4 eV), NiO (856.2 eV) and $Ni(OH)_2$ (857.7 eV). As shown in Figure 3.5, the high-resolution spectra of O1s were curve-fitted with two different peaks at 529.8 and 531.6 eV for the NA surfaces, and these peaks were assigned to metal-oxides and hydroxides, respectively. After anodization, these two peaks appeared at 531.4 and 531.6 eV for ND25, 530.1 and 532.1 eV for ND200, 531.3 and 531.8 eV for NP25, 530.3 and 531.5 eV for NP200 samples. It was observed that OH^- peak intensity significantly increased on all nanostructured samples, especially ND25 and NP25 samples. Moreover, the hydroxylation degree (OH^-/O^{2-}) was quantitatively analyzed to be 2.24, 5.41, 4.85, 5.70 and 3.52 for the NA, ND25, ND200, NP25 and NP200 sample surfaces, respectively.
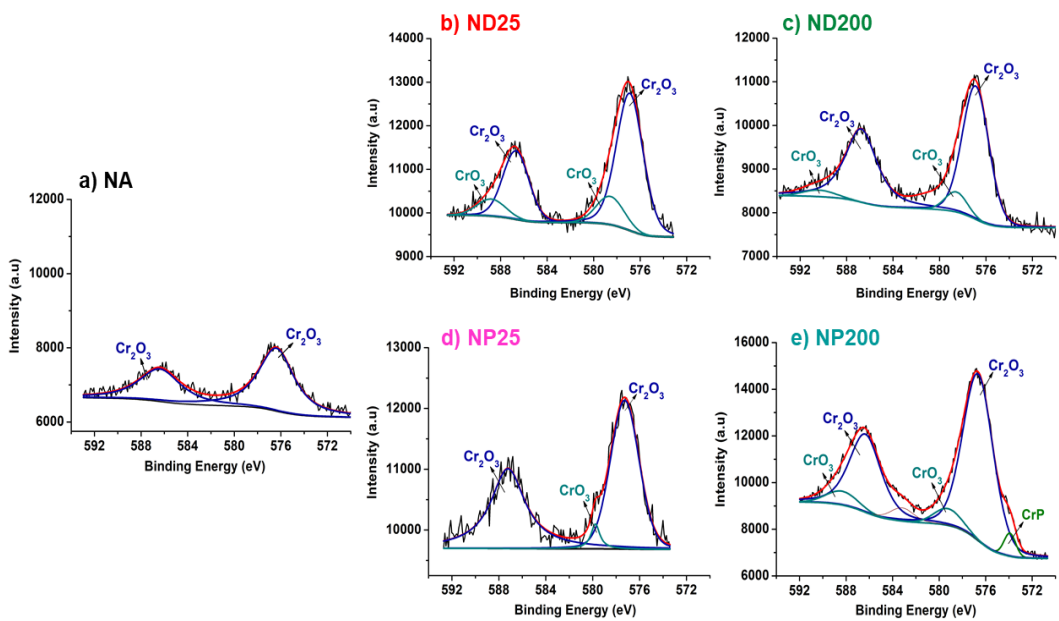
Figure 3.2 High resolution XPS spectra of Cr $2p_{3/2}$ peaks of the NA, ND25, ND200, NP25 and NP200 samples.
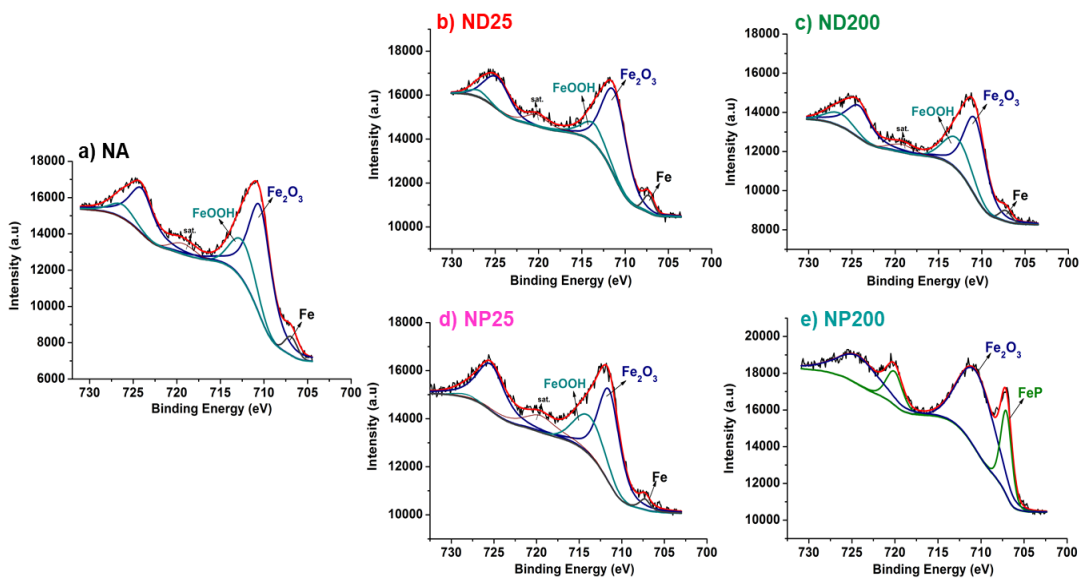
Figure 3.3 High resolution XPS spectra of Fe $2p_{3/2}$ peaks of the NA, ND25, ND200, NP25 and NP200 samples.
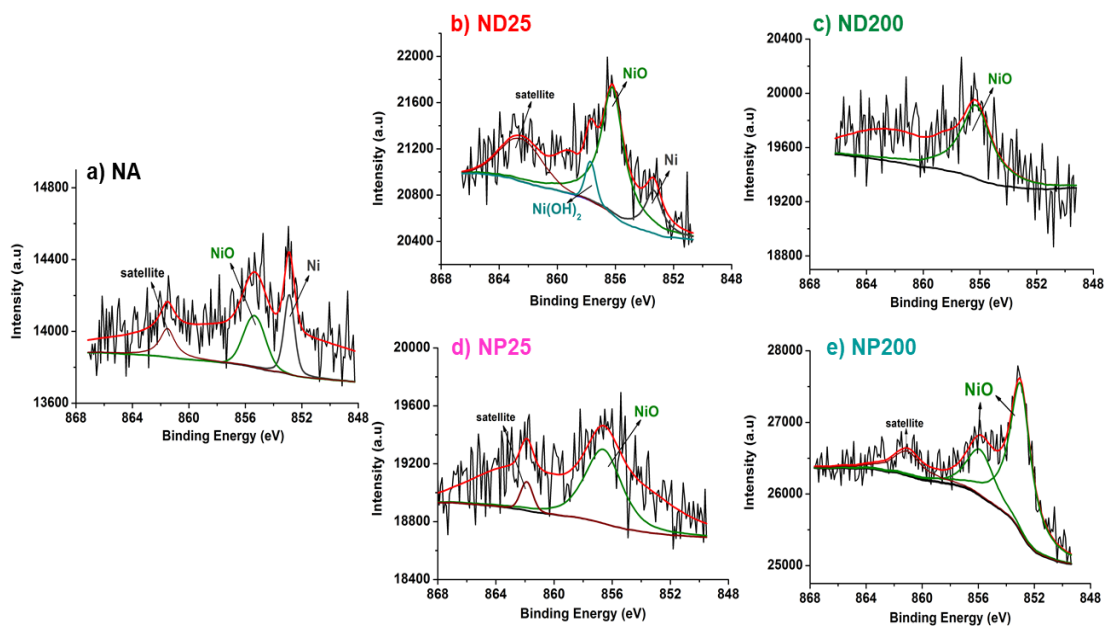
Figure 3.4 High resolution XPS spectra of Ni 2p$_{3/2}$ peaks of the NA, ND25, ND200, NP25 and NP200 samples.
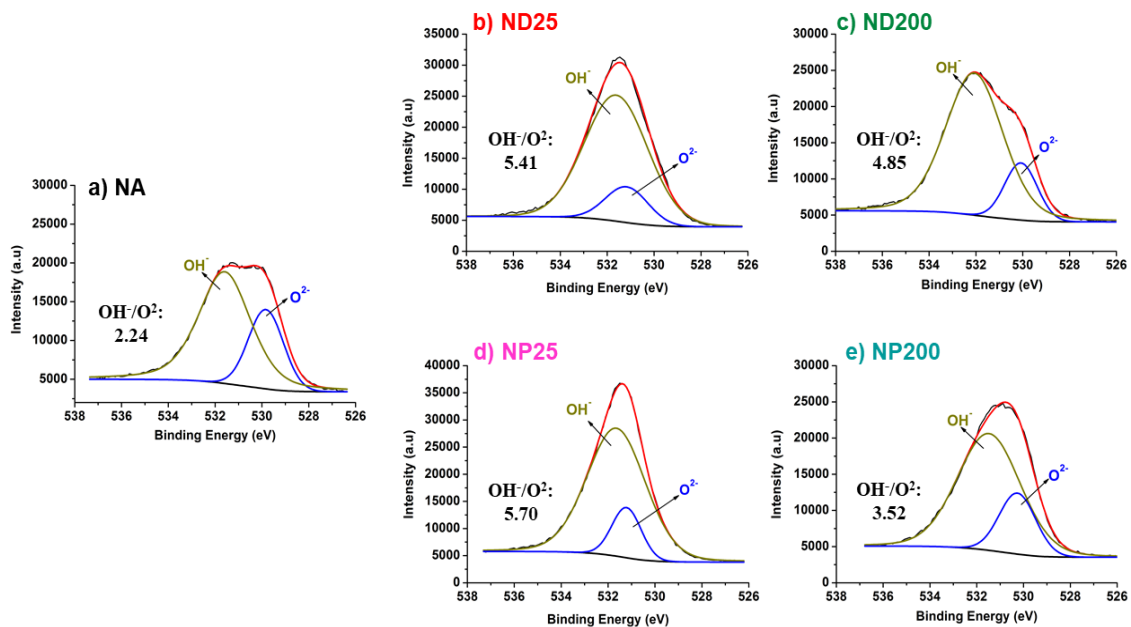
Figure 3.5 High resolution XPS spectra of O 1s peaks of the NA, ND25, ND200, NP25 and NP200 samples.

The zeta potentials were measured at pH 7.2 for all surfaces. As shown in Figure 3.6a, surface charge values were measured as -45.86 ± 8.11, -202.17 ± 7.66, -132.46 ± 9.36, -320.50 ± 5.52 and -146.75 ± 6.31 mV for NA, ND25, ND200, NP25 and NP200 samples, respectively. The results showed that nanostructured surface had more negative surface charges than non-anodized surface. The surface chemistry, especially OH$^-$ component on surface, and surface morphology could affect the surface charged. Especially, the increased intensity of the OH$^-$ component after anodization contribute to negativity of surface charged. On the other hand, the amount of nickel ion releases from samples were observed to be 5.7 ± 0.8, 16.5 ± 4.0, 3.9 ± 1.2, 6.8 ± 1.1 and 4.2 ± 1.5 μg/mL for NA, ND25, ND200, NP25 and NP200 samples, respectively (Figure 3.6b). Moreover, there is no detected any chromium release from samples. These results may be associated with the surface chemistry and its stability. That being said, the highest nickel ion detection from the ND25 surface could be related to the presence of a higher nickel peak intensity on its surface. Furthermore, when we consider increased surface areas of ND200 and NP200 surfaces, the nickel ion release is acceptable compared to non-anodized surface.
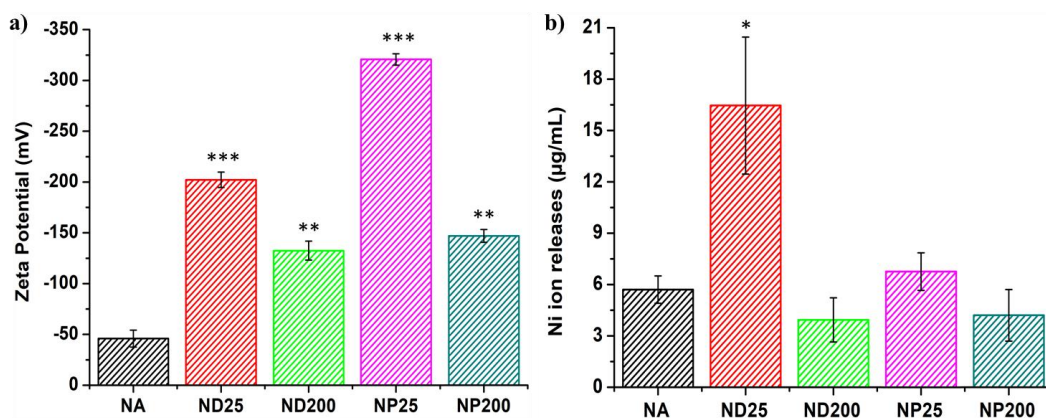
Figure 3.6 The graphs show a) zeta potential values, and b) nickel ion release from the samples, *p<0.05, **p<0.05, and ***p<0.001 compared to NA.

One of the major issues of 316L SS is its insufficient corrosion resistance in the human body, which causes severe complications. The electrochemical behavior of NA and nanostructured samples results are given in Figure 3.7. The positive OCP values of the samples indicate better corrosion behavior of samples. In general, the lower corrosion current (I_{corr}) represent corrosion behavior of surface and positive corrosion potential (E_{corr}) indicate thermodynamic corrosion tendency. The polarization curve of the samples in 1xPBS are given in Figure 3.7b. Tafel plot analysis revealed E_{corr} and I_{corr} values of the samples provided in Table 3.2. The results showed that the ND200 surface had the lowest I_{corr} and corrosion rates. On the other hand, ND25 and NP25 surfaces performed lower I_{corr} values although thery have negative E_{corr} compared to the NA surfaces. Moreover, the corrosion rate values of the samples were calculated to be 189.7 ± 7.4, 122.1 ± 12.1, 95.2 ± 4.8, 141.0 ± 6.1 and 164.6 ± 4.2 nm per year for the NA, ND25, ND200, NP25 and NP200

samples, respectively. These results showed that oxide based nanostructured surface fabricated via anodization could significantly enhance corrosion resistance.
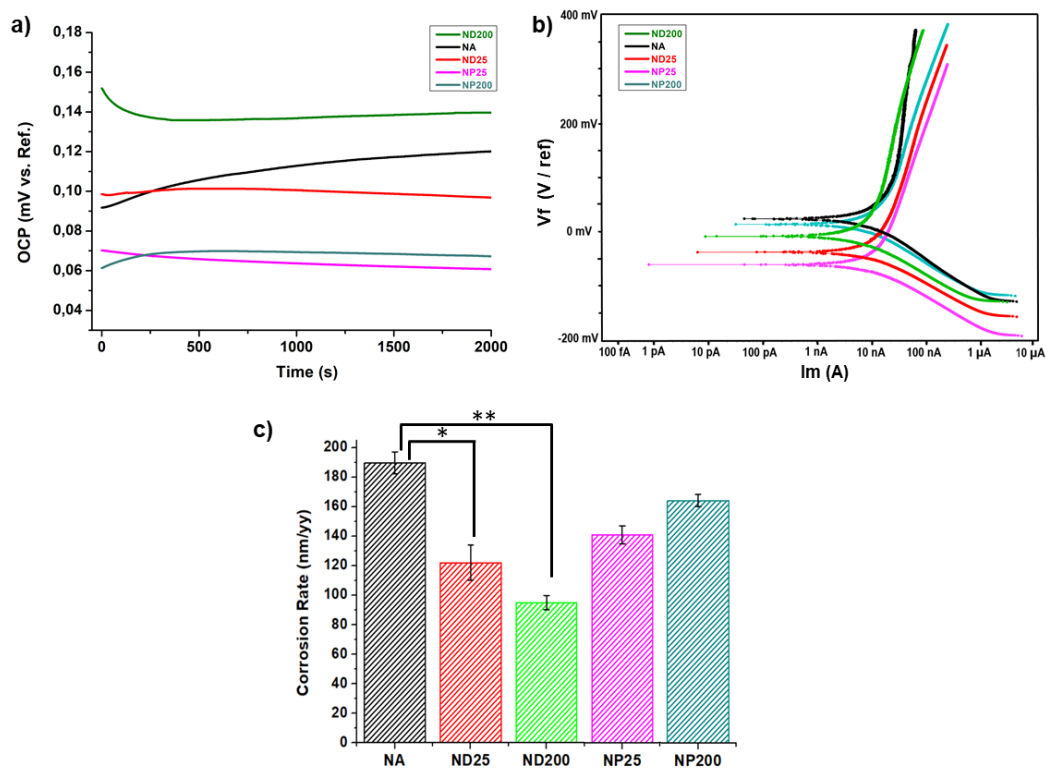
Figure 3.7 a) Open circuit potentials, b) Tafel plots, and c) the corrosion rate of the samples, *p<0.05, **p<0.01.

Table 3.2 Electrochemical parameters obtained from the potentiodynamic
polarization curves of the samples.

	E_{corr} (mV)	I_{corr} (nA)	Corrosion Rate (nm/yy)
NA	23.5	18.5	189.7
ND25	-36.9	12.1	122.1
ND200	10.7	7.9	95.2
NP25	-60.0	12.2	141.0
NP200	13.5	13.8	164.6

Nyquist plots of the samples are presented in Fig 3.8. The diameter of the semicircle for ND200 and NP200 surfaces are larger than that of the control 316L SS surface, suggesting a higher corrosion resistance. Electrochemical impedance spectroscopy (EIS) data fit well to the simplified circuit model (Fig 3.8b). R_{el} corresponds to the resistance of the solution, R_c and C_c represents the resistance of the passive film and native oxide layer capacitance, C_{dl} is the double layer capacitance, and R_{ct} is the charge transfer resistance. Circuit diagram fitting results are provided in Table 3.3. According to these results, higher value of R_{ct} can obtained for the ND200 surface while NA surface exhibited the lowest resistance values. Thus, oxide based nanostructured surface had better corrosion resistance due to its higher charge transfer resistance. In addition, there is a correlation between the lower double layer capacitance and surface roughness, where a lower value indicates a rougher corresponding electrode surface (Shuang et al., 2020). Therefore, the mechanism of the corrosion protection of the oxide based nanostructured film could be related to its characteristics of surface morphology and surface chemistry.
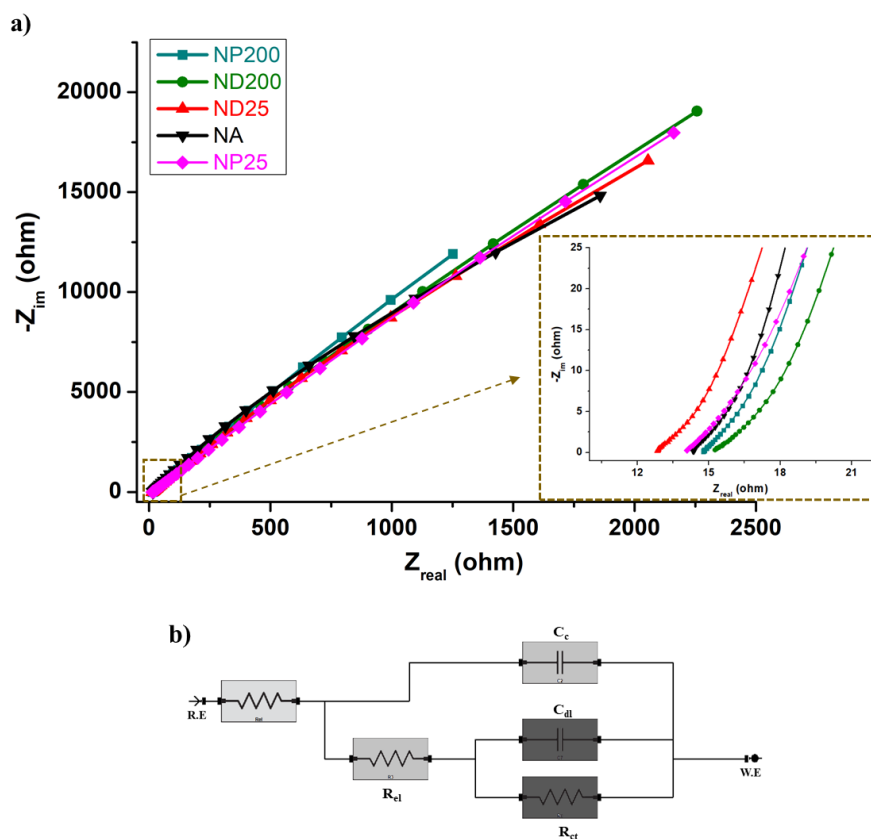
Figure 3.8 a) Nyquist plots from the EIS measurements of the samples, and b) simplified circuit model used for the EIS analysis.

Table 3.3 Circuit parameters calculated from the EIS spectra for control and nanostructured surfaces.

	R_{el} (Ohm)	C_c (10^{-7} F)	R_c (ohm)	C_{dl} (10^{-7} F)	R_{ct} (kohm)	χ^2
NA	15.01	3.93	685.80	1.24	8.26	0.777
ND25	13.62	3.02	549.50	1.22	9.53	0.328
ND200	16.30	2.64	187.10	1.06	11.20	0.838
NP25	16.22	3.68	380.10	1.41	10.80	0.299
NP200	14.93	2.65	618.00	1.24	10.30	0.568

3.2.2 *In Vitro* Biological Properties

HUVEC proliferation on non-anodized and nanostructured surfaces were shown in Fig 3.9a. On the 1st day of culture, there were no significant differences observed between the sample groups. However, on the 3rd day of cell culture, cellular proliferation on the ND200, NP25 and NP200 samples were higher than non-anodized samples ($p < 0.05$). After 5th day of cell culture, nanostructured samples significantly enhanced cellular proliferation compared to the non-anodized sample ($p < 0.01$). The enhanced cellular proliferation could be explained by the nanostructured surface roughness and larger surface areas of the samples, indicating a favorable environment for cellular growth and activity.

The nucleus (blue), f-actin filament (red) and vinculin (green) stained HUVECs on non-anodized and nanostructured samples are illustrated in Figure 3.9b-f. The merged immunofluorescence images showed well-organized actin fibers and elongated cellular morphology on nanostructured surfaces. Vinculin is a cytoskeletal protein that is an important component of focal adhesions, providing a structural link between the cell and its environment. The presence and well distribution of focal adhesions on nanostructured surfaces, especially ND200, indicate better cell migration and signaling on these surfaces. Moreover, cellular spreading were measured to be 1.97×10^{-3}, 3.97×10^{-3}, 4.22×10^{-3}, 2.85×10^{-3}, 3.77×10^{-3} mm^2/cell for the NA, ND25, ND200, NP25 and NP200 samples, respectively.

In addition, the cellular morphology on non-anodized and nanostructured surfaces were further investigated by SEM, and the images were shown in Figure 3.9g-k. The SEM micrographs showed that endothelial cells on the nanostructured surface exhibited well-spread morphology with larger filopodia extension. Especially, the inset images clearly showed that endothelial cells sensed the surfaces better, which led to the notable extension of filopodia. It should be noted that filopodia formation and extension is also an important implication for cellular migration and cell adhesion (Mattila & Lappalainen, 2008)(Knecht et al., 2010).
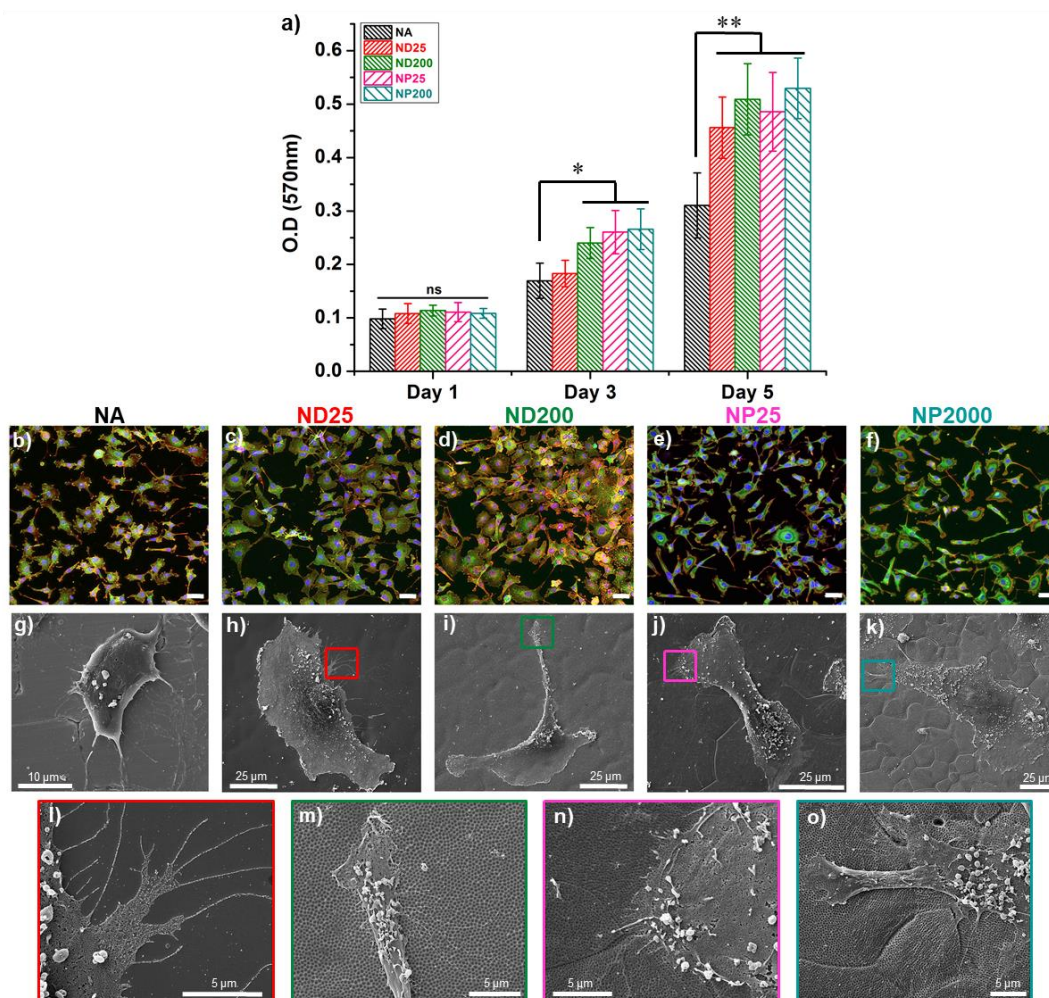
Figure 3.9 a) HUVEC viability on NA, ND25, ND200, NP25 and NP200 samples up to 5 days *in vitro*, *p < 0.05, **p<0.01. (b–f) Nuclei (blue), f-actin (red) and vinculin (green) stained HUVECs on the b) NA, c) ND25, d) ND200, e) NP25 and f) NP200 samples at the third day of culture. (g-o) SEM micrographs of HUVECs on the g) NA, (h, l) ND25, (i, m) ND200, (j, n) NP25 and (k, o) NP200 samples.

Scratch assay provide important information about cellular migration and endothelization on stent surfaces. To investigate the migration behavior of HUVECs on non-anodized and nanostructured surfaces, a scratch was generated and closure of that scratch was investigated at 4, 8, 12 and 24 hours *in vitro*. As shown in Figure

3.10, SEM images clearly showed that the scratches on the nanostructured surfaces were much rapidly closed by endothelial cells compared to non-anodized surface at all cultured time points. According to these results, the NA surface was covered by 14.7%, while the ND25 and NP200 surfaces were covered by 28.3 and 29.8%, respectively at the end of the 4th hour. The wound closure rates were calculated to be 52.1, 57.8, 60.2 and 61.4% for ND25, ND200, NP25 and NP200 surfaces, respectively, whereas it was 35.9% for the NA surface at the end of 8 hours *in vitro*. At the end of 12 hours of culture, the wound closure rates were determined to be %68.1 for the NA surface, while it was 87.5, 92.5, 86.6 and 94.7% for the ND25, ND200, NP25 and NP200 surfaces, respectively. Moreover, the wound on the nanostructured surfaces closed completely at 24h, while non-anodized surface had still a gap, as presented in Figure 3.10b. The quantitative analysis of the results revealed that nanostructured surfaces significantly enhanced cell migration compared to non-anodized surface ($p < 0.05$), as presented in Figure 3.10c. As a result, the migration capacity of HUVECs on the ND200 samples was found to be higher than non-anodized samples, which is critical to rapid endothelization on stent surfaces.
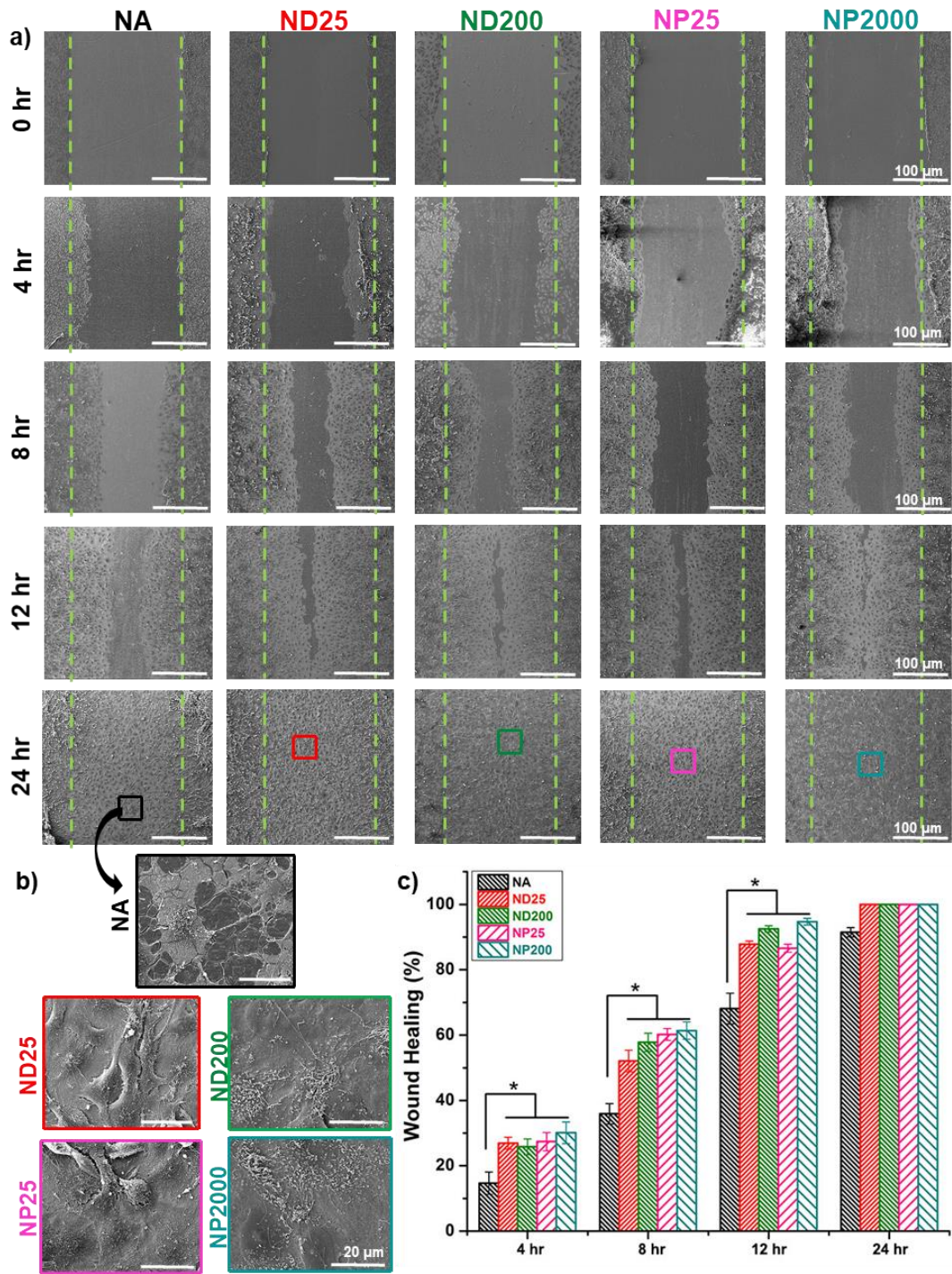
Figure 3.10 Scratch assay of the HUVECs cultured on the samples up to 24 h. a) The SEM images of HUVECs migrating on the samples up to 24 h of culture. b) Higher magnification SEM micrographs at 24 hr of culture. c) The wound closure percentage of the samples.

Nitric oxide synthesis provides cardiovascular hemostasis and induces vasodilation effects, therefore play a crucial role in the proliferation and migration of HUVECs. Figure 3.11b shows NO_x secretion from HUVECs on non-anodized and nanostructures surfaces. The results showed that NO_x secretion was significantly higher on ND200 and nanopit samples compared to the non-anodized samples after 1 day ($p<0.05$). However, at the end of 3 days of culture, significant differences between the sample groups disappeared ($p>0.05$). PGE_2 has vasodilatory effects that inhibit platelet aggregation and influence cell proliferation and angiogenesis. As shown in Figure 3.11c, there was no difference in PGE_2 secretion from HUVECs onto the sample groups ($p>0.05$). At the end of day 3, it was determined that HUVECs on ND200, NP25 and NP200 surfaces significantly enhanced PGE_2 secretion compared to the non-anodized samples ($p<0.05$). On the other hand, End-1 function has a vasoconstrictor effect that secretion is implicated in inflammatory processes and atherosclerosis disease. After 1 day of incubation, End-1 secretion from the nanostructured surfaces was lower than the one from non-anodized sample ($p<0.05$). However, at the end of day 3, NP surfaces exhibited lower End-1 secretion compared to the ND and NA surfaces ($p<0.05$).

To sum up, these results demonstrated that the created nanostructured surface in this study significantly influenced endothelial cell functions. This effect could potentially contribute to improved endothelization and the inhibition of the inflammation process.
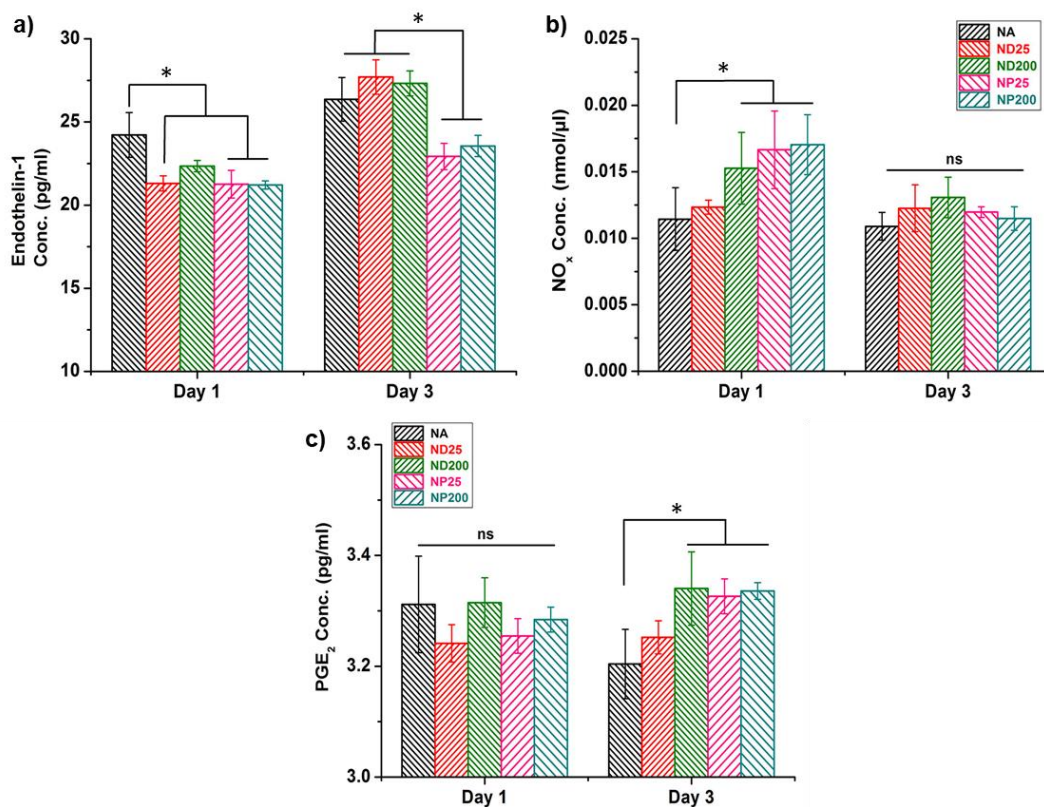
Figure 3.11 a) End-1, b) NOx, and c) PGE2 released from HUVECs cultured on the samples up to 3 days, *p<0.05.

We further evaluated the effect of nanostructured surfaces on the expression of angiogenesis related genes in HUVECs up to 7 days. The expression results of VCAM-1, ICAM-1 and PECAM-1 genes onto surfaces are shown in Figure 3.12. VCAM-1 gene is associated with inflammatory response and development of atherosclerosis. According to the results, it was observed that VCAM-1 gene expression on non-anodized surface were higher than all nanostructured surfaces after 1, 3 and 7 days of incubation (p<0.05). Similarly, ICAM-1 gene expression was higher on non-anodized surface compared to nanostructured surfaces at 1 and 3 days of cultured (p<0.05). After 7th day of cell culture, the lowest ICAM gene expression was observed on the ND200 surface. On the other hand, PECAM-1 plays crucial role

in cell adhesion, cell-cell junctions, and provides anti-inflammatory effects. After 1st and 3rd days of cell culture, there were no observed PECAM-1 gene expression differences between sample groups (p<0.05). However, it was observed that PECAM-1 gene expression significantly upregulated on NP25 and NP200 surface at the end of 7th day of cell culture (p<0.05).
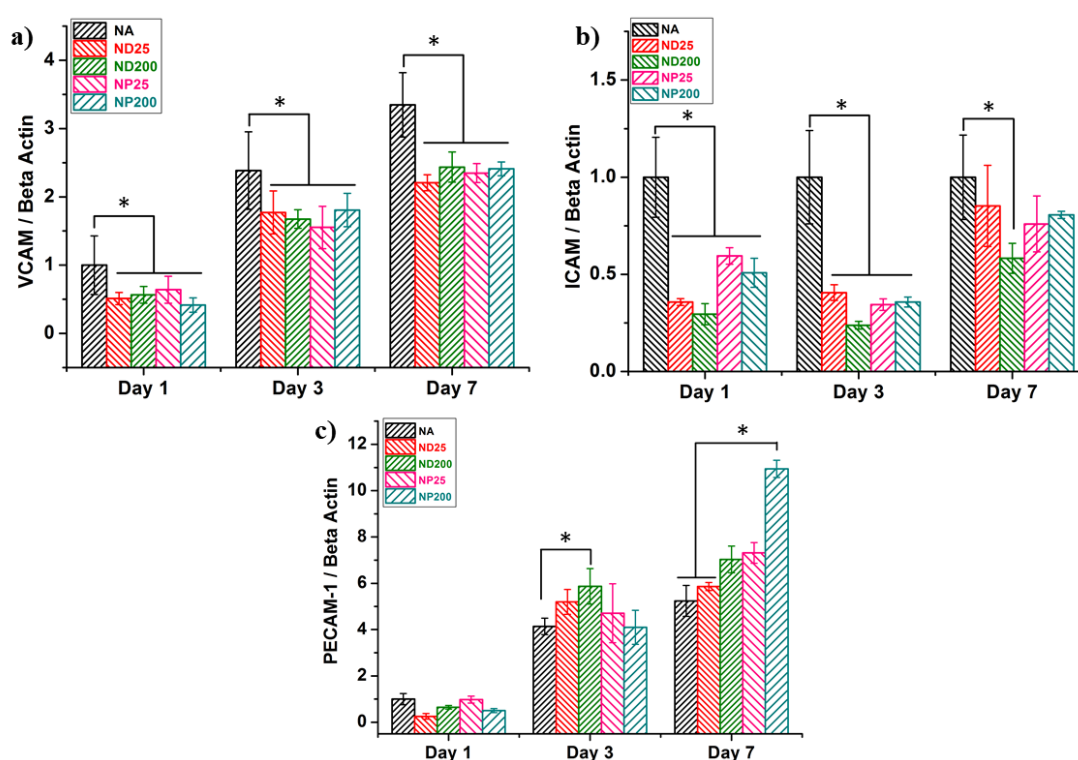
Figure 3.12 Gene expression analysis of HUVECs. a) VCAM-1, b) ICAM, and c) PECAM-1 gene expressions on the NA, ND25, ND200, NP25 and NP200 samples up to 7 days, *p < 0.05.

3.2.3   Hemocompatibility Studies

The morphology of the adherent platelets on the non-anodized and nanostructured surfaces are displayed in Figure 3.13. The platelet morphology on the surface is an important clue about its activation state (Ge et al., 2019). SEM images showed that higher number of aggregated and adherent platelets were present on the NA sample. The platelets had fully spread and long dendritic morphology. However, compared to the NA surface, less platelet adhesion with partial spreading and short dendritic morphology was observed on the ND25 and NP25 samples. Inactivated platelet morphology with fewer platelets was observed on ND200 and NP200 surfaces. This result suggest that thrombosis can probably occur on NA surfaces due to actived and aggregated platelet morphology on its surfaces (Manivasagam et al., 2021). Similarly, calcein am staining results were in-line with SEM images that more adherent platelets were observed on the NA surface, which exhibited elongated dendritic morphology. On the other hand, fewer platelet adhesion with inactivated morphology were observed on the ND200 surface (Figure 3.13l). Quantitative analysis of platelet adhesion on the samples revealed that nanostructured surfaces significantly decreased platelet adhesion compared to the NA surface (p<0.05). The results showed 49% reduction in platelet adhesion on the ND200 sample compared to the non-anodized sample. Hemolysis rate of the samples is given in Figure 3.13n. According to ISO10993-4 standard, a biomaterial should have hemolysis rate of less than 5% to be used as blood-contacting implant. Thus, hemolysis results showed that all surfaces exhibited the desired hemocompatibility. Interestingly, ND200 and ND25 surfaces significantly reduced the hemolysis rate compared to the NA sample, and they exhibited the best potential surface to enhance blood compatibility. These results revealed that surface properties, such as nanostructured topography, morphology, and surface charge can significantly affect platelet adhesion, activation and hemocompatibility of the stent surfaces. The created nanostructured surface roughness reduced platelet adhesion. Similarly, various studied confirmed our results that larger feature size of nanostructured surfaces could reduce platelet adhesion and

activation (Huang et al., 2017; Ferraz et al., 2008). In addition, the negative surface charge and presence of OH⁻ on the surface could contribute to the repellence of the platelets, which has negatively charged.
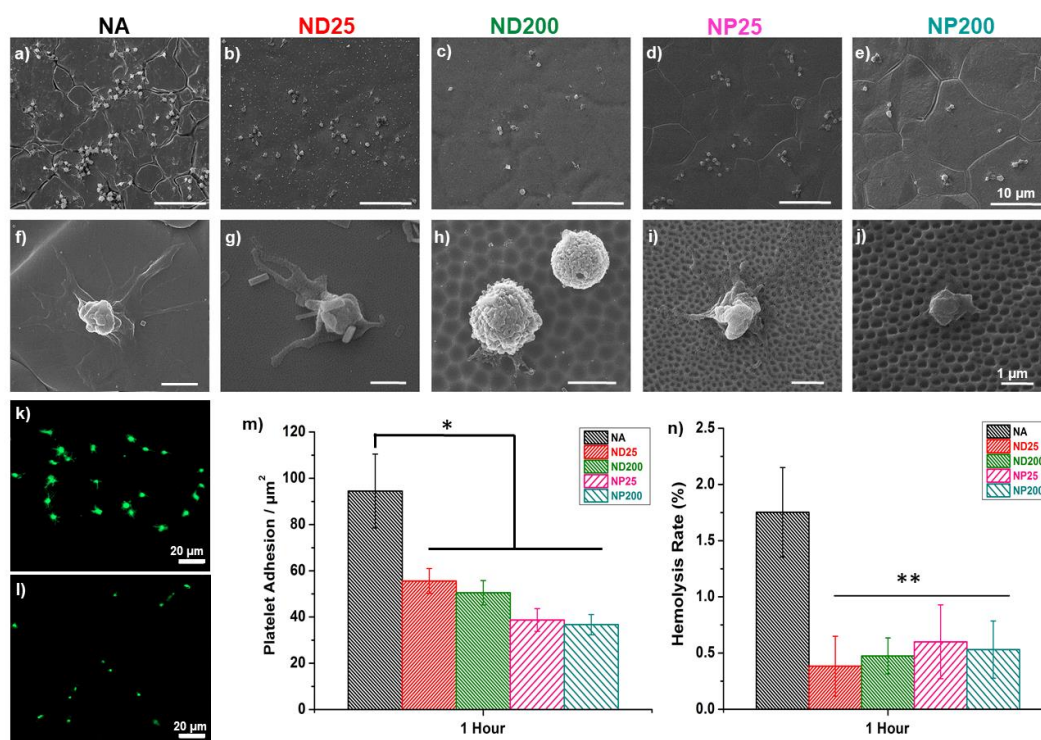
Figure 3.13 (a–j) SEM micrographs, and (k, l) calcein am stained platelets on the (a, f, k) NA, (b, g) ND25, (c, h, l) ND200, (d, i) NP25, and (e, j) NP200 samples. of m) Platelet adhesion, and n) hemolysis rate of the NA, ND25, ND200, NP25 and NP200 samples, *p < 0.05, **p < 0.01.

3.3 Discussion

Stainless steel is one of the commonly-used implant materials for stent applications. However, it has major drawbacks and challenges in clinical applications, which is restenosis, stent thrombosis, inflammatory, poor endothelization, nickel ion release and corrosion. These issues impact the healing response, result in short and long-term complications, and potentially lead to implant failure. It is important to note that creating nanostructured roughness and changing surface properties of the stent by modifying its surfaces potentially remedy these issues, and can offer improved corrosion resistance, biocompatibility, and hemocompatibility. In this study, we observed the effect of nanostructured topography on HUVEC proliferation, functions and gene expression. Also, we demonstrated enhanced corrosion resistance and improved hemocompatibility of nanostructured 316L SS.

Our results indicated that we successfully obtained different nanofeature sizes and morphologies on 316L SS surfaces, as shown in Figure 3.1. The feature size of nanostructured could influence cell adhesion and differentiation. Moreover, a unique nanoscale topography on 316L surface which is important for protein adsorption and cellular proliferation. On the other hand, it is well known that stent material is corroded in the body with time, the leading cause of inflammation due to ion releases, and could also result in a loss of superior mechanical properties. The results of the corrosion experiment indicated that addressing this issue could be achieved by creating oxide-based nanostructures on the surface since the oxide layer acts as a barrier film. Especially, it was observed that ND200 samples exhibited lower corrosion current (Icorr) and corrosion rate, along with higher charge transfer resistance compared to the bare 316L SS. The enhanced corrosion resistance can be explained by the surface chemistry of the oxide-based nanostructured surfaces, especially increased the intensity of the Cr_2O_3 peak in the XPS spectra, which provide corrosion protection, and decrease Ni peak intensity of the ND200 surfaces. Also, surface roughness can influence both corrosion behavior of the samples, and nucleation of metastable pitting and pitting potentials. A correlation could be

observed between the surface roughness and E_{corr} values, indicating that a rougher surface resulted in a lower E_{corr} values. Similarly, the results of ion releases from surface confirms the XPS analysis and corrosion results. The ND200 surface, which has minimum nickel component on its surfaces, performed the lowest nickel ion release among all investigated samples.

On the other hand, achieving rapid endothelization on the stent surface is another crucial factor for successful stent applications. Because endothelial cells play an important role in controlling smooth muscle cell proliferation, platelet activation, and thrombosis through the regulation of their cellular functions and gene expression. (Michiels, 2003; Yau et al., 2015). The *in vitro* results showed that nanostructured samples significantly enhanced HUVEC proliferation compared to the NA samples. Immunofluorescence staining showed that HUVECs sensed nanostructured roughness better and had a well-spread cellular morphology. Also, cells had a larger filopodia extension on the nanostructured samples, which is an important cue for cell migration. Scratch assay confirmed that nanostructured surface promoted higher cellular migration, which is critical for endothelization. Moreover, HUVECs on nanostructured surface expressed higher nitric oxide and prostaglandin synthesis. Nitric oxide and prostaglandin serve as a modulation angiogenesis, while inhibiting platelet adhesion and inflammation (Cahill & Redmond, 2016). Especially, enhanced nitric oxide secretion on the nanostructured surface is promising for stent applications due to its support endothelization and angiogenic effects. Moreover, the nanostructured surface significantly restricted End-1 expression compared to the NA samples, which can potentially contribute to the mitigation of the atherosclerosis process. Taking into account the effects of nitric oxide and prostaglandins, both of which function to modulate angiogenesis, inhibit inflammatory responses, and prevent platelet adhesion, the nanoscale topography on the stent surface demonstrated a favorable microenvironment for rapid endothelization. In addition, one study showed that the nanoscale surface did not promote smooth muscle cell adhesion, with fewer focal contacts of smooth muscle cells observed on the nanostructured surface (Cherian et al., 2022). Also, a study

result supported our findings that creating nanotopograhy on SS stent surface by coated TiO2 nanostructure was revealed to significantly enhance HUVEC proliferation and nitric oxide production while reducing smooth muscle cell proliferation compared to the unmodified SS surface (Mohan et al., 2017).

Furthermore, PECAM-1 expression, which plays a crucial role in cell migration and cell-to-cell interactions, was significantly induced on the nanostructured surfaces. On the other hand, VCAM-1 and ICAM-1 genes, which are responsible for atherosclerosis and platelet aggregation, it was found that their expression was higher on NA samples. That said, nanoscale topography enhanced endothelization and endothelial cell functions, while bare smooth surface has potential inflammation effects. In line with literature, a similar effect of nanostructured topography was observed *in vivo*, where coating titania nanotextured Co-Cr stent exhibited rapid re-endothelization and minimal stent restenosis during 8 weeks implantation in rabbit arteries, compared to bare and drug-eluting stents (Cherian et al., 2022). Another finding from an *in vivo* study confirmed that the nanoscale titania topography on stainless steel stent surfaces improved endothelial coverage, thereby significantly reducing stent restenosis over an 8-week period, in comparison to bare metal stents (Cherian et al., 2020). However, in the case of potential cracking or delamination of coating from surfaces, it may lead to inflammation and dysfunction of endothelization effects for long-term applications.

The nanostructured 316L stent surface performed enhanced hemocompatibility, providing a substantial reduction in both platelet adhesion and hemolysis rate. This improvement promotes its potential application in cardiovascular implants where minimizing blood-material interactions is crucial for long-term functionality and biocompatibility. The hemocompatibility of stent surface is usually related to the surface roughness, chemistry, and charge (Manivasagam et al., 2021). It was observed that the nanostructured surfaces showed more negative surface charge after the anodization process compared to bare surface. The presence of OH⁻ on the surface chemistry could contribute to the repulsion of platelet (Nagai et al., 2014). This negatively charged of nanostructured surface provides electrostatic repulsion to

platelets due to their negative charge, thereby reducing platelet adhesion and may potentially prevent thrombosis. Furthermore, nanostructured topography of the surface provide less platelet adhesion and activation (Moradi et al., 2016). In line with our result, an *in vivo* study confirmed that no inflammation and small platelet adhesion was observed on nanostructured titanium stent. In contrast, bare stent surface showed fully activated platelet coagulation and thrombus formation (Zhang et al., 2022).

In summary, the success of stents implantation depends on various important factors, such as rapid endothelization, thrombosis occurrence, corrosion resistance, as well as providing hemostasis. In this thesis study, our findings showed that creating nanoscale topography on stent surfaces enhanced proliferation, functions and gene expressions of HUVECs, which enhanced endothelization and angiogenic activity. Moreover, this nanostructured surfaced improved corrosion resistance and hemocompatibility for stent applications.

CHAPTER 4

CONCLUSION

This thesis covers fabrication of unique nanostructured topographies on 316L SS surfaces, and comprehensively evaluated surface properties and cellular functions *in vitro* for orthopedic and cardiovascular applications.

In the first part of thesis, we successfully obtained uniform ND structures on the 316L SS surfaces using electrochemical anodization technique for orthopedic applications. Our results suggested that ND surfaces having a 200 nm feature size enhanced osteoblast viability and spreading with well-defined cytoskeletal organization. Furthermore, these nanofeatured surfaces stimulated ALP activity and promoted calcium mineral deposition. In addition, ND surfaces having a 200 nm feature size showed anti-fouling activity against Gram- positive *S. aureus* and Gram-negative *P. aeruginosa* and limited biofilm formation. Cumulatively, fabrication of the ND morphologies via anodization could remedy the two major shortcomings of 316L SS implants: the bioinert nature of 316L SS and infection induced failure of the implants. This study suggested that 200nm sized ND surfaces can be a promising candidate for orthopedic applications.

In the second part of the thesis, we conducted a comprehensive investigation of the impact of nanostructured surfaces on corrosion behavior, and *in vitro* cellular interactions for cardiovascular stent applications. We fabricated 25nm and 200 nm sized features, which had ND and NP morphologies, on the 316L SS surface by altering the anodization parameters. We observed that the nanoscale roughness and surface areas significantly increased, and the surface was more negatively charged for the ND200 sample. Moreover, the ND200 sample improved the corrosion resistance, compared to the bare 316L SS. The nanostructured samples enhanced cellular proliferation, migration, and HUVEC functions, and at the same time

upregulated PECAM-1gene expression and limited VCAM-1 and ICAM-1 gene expressions, and thus proved to be an ideal stent material. Furthermore, the nanostructured samples exhibited superior performance in terms of both hemocompatibility. This result suggests a promising potential for addressing the persistent challenges associated with stent-restenosis and thrombosis, which are commonly faced challenges with bare 316L SS stents. The observed improvements in these crucial aspects highlight the significance of incorporating nanostructured surfaces for the development of cardiovascular stents. Not only does this advance contribute to enhancing the overall efficacy and safety of stent applications, but it also opens avenues for further innovations in biomaterials tailored to mitigate complications and improve patient outcomes in cardiovascular interventions.

That being said, there are essential aspects that warrant consideration and exploration for future research.

- In addition to the optimized anodization parameters used in this thesis, it is possible to delve deeper into optimizing the fabrication process of the nanostructured surfaces, exploring additional parameters, such as distance between anode and cathode, to fine-tune the morphology and dimensions for enhanced performance. Furthermore, optimized anodization parameters should be transferred for the real implant materials. However, the translational of this technology for real implant surfaces require further optimization of the anodization process for stent dimensions, strut size, implant curvature, which require designing proper cathode geometry, and perhaps sacrificial electrodes. Investigating the long-term durability and stability of the anodized samples under physiological conditions would provide valuable insights into their feasibility for extended applications.
- Additionally, an in-depth investigation into the molecular mechanisms underlying the observed improvement in osteoblast viability would be helpful both from a materials science and biology perspective. In fact, exploring the interaction of the nanofeature surfaces with other cell types

involved in the bone healing and formation processes, such as osteoclasts, and evaluating their impact on bone remodeling and overall osteointegration represent an important aspect for future research.

- Moreover, extending the antimicrobial assessments to encompass a broader spectrum of pathogens in a co-culture environment and considering real-world clinical scenarios would contribute to a comprehensive understanding of the anti-fouling and antibacterial properties of the nanostructured surfaces.

- Lastly, the translation of these promising findings from *in vitro* to *in vivo* studies would be a crucial step in validating the practical efficacy of the nanostructured surfaces in real cardiovascular stent and orthopedic implant scenarios. In fact, long-term *in vivo* studies are essential to validate the sustained performance and biocompatibility of the nanostructured surfaces within the complex physiological environment.

REFERENCES

Agbe, H., Sarkar, D. K., & Chen, X. G. (2022). Anodized Aluminum Surface with Topography-Mediated Antibacterial Properties. *ACS Biomaterials Science and Engineering*, *8*(3), 1087–1095. https://doi.org/10.1021/acsbiomaterials.1c01485

Asoh, H., Nakatani, M., & Ono, S. (2016). Fabrication of thick nanoporous oxide films on stainless steel via DC anodization and subsequent biofunctionalization. *Surface and Coatings Technology*, *307*, 441–451. https://doi.org/10.1016/j.surfcoat.2016.09.025

Bandara, C. D., Singh, S., Afara, I. O., Wolff, A., Tesfamichael, T., Ostrikov, K., & Oloyede, A. (2017). Bactericidal Effects of Natural Nanotopography of Dragonfly Wing on Escherichia coli. *ACS Applied Materials & Interfaces*, *9*(8), 6746–6760. https://doi.org/10.1021/acsami.6b13666

Bekmurzayeva, A., Duncanson, W. J., Azevedo, H. S., & Kanayeva, D. (2018). Surface modification of stainless steel for biomedical applications: Revisiting a century-old material. *Materials Science and Engineering C*, *93*(August), 1073–1089. https://doi.org/10.1016/j.msec.2018.08.049

Benčina, M., Junkar, I., Vesel, A., Mozetič, M., & Iglič, A. (2022). Nanoporous Stainless Steel Materials for Body Implants—Review of Synthesizing Procedures. *Nanomaterials*, *12*(17), 2924. https://doi.org/10.3390/nano12172924

Bian, Q., Chen, J., Weng, Y., & Li, S. (2022). Endothelialization strategy of implant materials surface: The newest research in recent 5 years. *Journal of Applied Biomaterials and Functional Materials*, *20*(111). https://doi.org/10.1177/22808000221105332

Bowen, P. K., Shearier, E. R., Zhao, S., Guillory, R. J., Zhao, F., Goldman, J., &

Drelich, J. W. (2016). Biodegradable Metals for Cardiovascular Stents: From Clinical Concerns to Recent Zn-Alloys. *Advanced Healthcare Materials*, *5*(10), 1121–1140. https://doi.org/10.1002/adhm.201501019

Brown, J. C., Gerhardt, T. E., & Kwon, E. (2023). *Risk Factors for Coronary Artery Disease.*

Cahill, P. A., & Redmond, E. M. (2016). Vascular endothelium - Gatekeeper of vessel health. *Atherosclerosis*, *248*, 97–109. https://doi.org/10.1016/j.atherosclerosis.2016.03.007

Chen, Q., & Thouas, G. A. (2015). Metallic implant biomaterials. *Materials Science and Engineering R: Reports*, *87*, 1–57. https://doi.org/10.1016/j.mser.2014.10.001

Cheng, Y., Feng, G., & Moraru, C. I. (2019). Micro-and nanotopography sensitive bacterial attachment mechanisms: A review. *Frontiers in Microbiology*, *10*(FEB), 1–17. https://doi.org/10.3389/fmicb.2019.00191

Cherian, A. M., Joseph, J., Nair, M. B., Nair, S. V., Maniyal, V., & Menon, D. (2020). Successful Reduction of Neointimal Hyperplasia on Stainless Steel Coronary Stents by Titania Nanotexturing. *ACS Omega*, *5*(28), 17582–17591. https://doi.org/10.1021/acsomega.0c02045

Cherian, A. M., Joseph, J., Nair, M. B., Nair, S. V., Vijayakumar, M., & Menon, D. (2022). Coupled benefits of nanotopography and titania surface chemistry in fostering endothelialization and reducing in-stent restenosis in coronary stents. *Biomaterials Advances*, *142*(October), 213149. https://doi.org/10.1016/j.bioadv.2022.213149

Cho, Y. C., Hung, W. C., Lan, W. C., Saito, T., Huang, B. H., Lee, C. H., Tsai, H. Y., Huang, M. S., & Ou, K. L. (2021). Anodized biomedical stainless-steel mini-implant for rapid recovery in a rabbit model. *Metals*, *11*(10), 1–11. https://doi.org/10.3390/met11101575

Chopra, D., Gulati, K., & Ivanovski, S. (2021). Understanding and optimizing the antibacterial functions of anodized nano-engineered titanium implants. *Acta Biomaterialia*, *127*, 80–101. https://doi.org/10.1016/j.actbio.2021.03.027

Clare, J., Ganly, J., Bursill, C. A., Sumer, H., Kingshott, P., & de Haan, J. B. (2022). The Mechanisms of Restenosis and Relevance to Next Generation Stent Design. *Biomolecules*, *12*(3), 1–26. https://doi.org/10.3390/biom12030430

Davoodi, E., Zhianmanesh, M., Montazerian, H., Milani, A. S., & Hoorfar, M. (2020). Nano-porous anodic alumina : fundamentals and applications in tissue engineering. *Journal of Materials Science: Materials in Medicine*. https://doi.org/10.1007/s10856-020-06398-2

Dhawan, U., Pan, H. A., Shie, M. J., Chu, Y. H., Huang, G. S., Chen, P. C., & Chen, W. L. (2017a). The Spatiotemporal Control of Osteoblast Cell Growth, Behavior, and Function Dictated by Nanostructured Stainless Steel Artificial Microenvironments. *Nanoscale Research Letters*, *12*(1), 1–10. https://doi.org/10.1186/s11671-016-1810-1

Dhawan, U., Pan, H. A., Shie, M. J., Chu, Y. H., Huang, G. S., Chen, P. C., & Chen, W. L. (2017b). The Spatiotemporal Control of Osteoblast Cell Growth, Behavior, and Function Dictated by Nanostructured Stainless Steel Artificial Microenvironments. *Nanoscale Research Letters*, *12*(1). https://doi.org/10.1186/s11671-016-1810-1

Domínguez-Jaimes, L. P., Vara, M. Á. A., Cedillo-González, E. I., Valdés, J. J. R., De Damborenea, J. J., Del Campo, A. C., Rodríguez-Varela, F. J., Alonso-Lemus, I. L., & Hernández-López, J. M. (2019). Corrosion resistance of anodic layers grown on 304L stainless steel at different anodizing times and stirring speeds. *Coatings*, *9*(11), 1–14. https://doi.org/10.3390/coatings9110706

Ercan, B., Taylor, E., Alpaslan, E., & Webster, T. J. (2011). Diameter of titanium nanotubes influences anti-bacterial efficacy. *Nanotechnology*, *22*(29). https://doi.org/10.1088/0957-4484/22/29/295102

Erdogan, Y. K., & Ercan, B. (2023). Anodized Nanostructured 316L Stainless Steel Enhances Osteoblast Functions and Exhibits Anti-Fouling Properties. *ACS Biomaterials Science and Engineering*, *9*(2), 693–704. https://doi.org/10.1021/acsbiomaterials.2c01072

Erdogan, Y. K., Uslu, E., Aydınol, M. K., Saglam, A. S. Y., Odabas, S., & Ercan, B. (2023). Morphology of Nanostructured Tantalum Oxide Controls Stem Cell Differentiation and Improves Corrosion Behavior. *ACS Biomaterials Science & Engineering*. https://doi.org/10.1021/acsbiomaterials.3c01277

Feng, G., Cheng, Y., Wang, S. Y., Borca-Tasciuc, D. A., Worobo, R. W., & Moraru, C. I. (2015). Bacterial attachment and biofilm formation on surfaces are reduced by small-diameter nanoscale pores: How small is small enough? *Npj Biofilms and Microbiomes*, *1*(August). https://doi.org/10.1038/npjbiofilms.2015.22

Feng, G., Cheng, Y., Wang, S. Y., Hsu, L. C., Feliz, Y., Borca-Tasciuc, D. A., Worobo, R. W., & Moraru, C. I. (2014). Alumina surfaces with nanoscale topography reduce attachment and biofilm formation by Escherichia coli and Listeria spp. *Biofouling*, *30*(10), 1253–1268. https://doi.org/10.1080/08927014.2014.976561

Ferraz, N., Carlsson, J., Hong, J., & Ott, M. K. (2008). Influence of nanoporesize on platelet adhesion and activation. *Journal of Materials Science: Materials in Medicine*, *19*(9), 3115–3121. https://doi.org/10.1007/s10856-008-3449-7

Fu, J., Su, Y., Qin, Y. X., Zheng, Y., Wang, Y., & Zhu, D. (2020). Evolution of metallic cardiovascular stent materials: A comparative study among stainless steel, magnesium and zinc. *Biomaterials*, *230*(November 2019), 119641. https://doi.org/10.1016/j.biomaterials.2019.119641

Galley, H. F., & Webster, N. R. (2004). Physiology of the endothelium. *British Journal of Anaesthesia*, *93*(1), 105–113. https://doi.org/10.1093/bja/aeh163

Gardin, C., Ferroni, L., Erdoğan, Y. K., Zanotti, F., De Francesco, F., Trentini, M., Brunello, G., Ercan, B., & Zavan, B. (2021). Nanostructured modifications of

titanium surfaces improve vascular regenerative properties of exosomes derived from mesenchymal stem cells: Preliminary in vitro results. *Nanomaterials*, *11*(12). https://doi.org/10.3390/nano11123452

Ge, S., Xi, Y., Du, R., Ren, Y., Xu, Z., Tan, Y., Wang, Y., Yin, T., & Wang, G. (2019). Inhibition of in-stent restenosis after graphene oxide double-layer drug coating with good biocompatibility. *Regenerative Biomaterials*, *6*(5), 299–309. https://doi.org/10.1093/rb/rbz010

Gonzalez, A. S., Riego, Vega, V., García, J., Galié, S., Gutiérrez-del-río, I., Martínez de Yuso, M. V., Villar, C. J., Lombó, F., & Prida, V. M. (2021). Functional antimicrobial surface coatings deposited onto nanostructured 316l food-grade stainless steel. *Nanomaterials*, *11*(4), 1–20. https://doi.org/10.3390/nano11041055

Gori, T., Polimeni, A., Indolfi, C., Räber, L., Adriaenssens, T., & Münzel, T. (2019). Predictors of stent thrombosis and their implications for clinical practice. *Nature Reviews Cardiology*, *16*(4), 243–256. https://doi.org/10.1038/s41569-018-0118-5

Guillory, R. J., Sikora-Jasinska, M., Drelich, J. W., & Goldman, J. (2019). In Vitro Corrosion and in Vivo Response to Zinc Implants with Electropolished and Anodized Surfaces. *ACS Applied Materials and Interfaces*, *11*(22), 19884–19893. https://doi.org/10.1021/acsami.9b05370

Herath, I., Davies, J., Will, G., Tran, P. A., Velic, A., Sarvghad, M., Islam, M., Paritala, P. K., Jaggessar, A., Schuetz, M., Chatterjee, K., & Yarlagadda, P. K. D. V. (2022). Anodization of medical grade stainless steel for improved corrosion resistance and nanostructure formation targeting biomedical applications. *Electrochimica Acta*, *416*(January), 140274. https://doi.org/10.1016/j.electacta.2022.140274

Hsu, H. J., Wu, C. Y., Huang, B. H., Tsai, C. H., Saito, T., Ou, K. L., Chuo, Y. C., Lin, K. L., & Peng, P. W. (2020). Surface characteristics and cell adhesion

behaviors of the anodized biomedical stainless steel. *Applied Sciences*, *10*(18), 1–8. https://doi.org/10.3390/APP10186275

Huang, Q., Yang, Y., Zheng, D., Song, R., Zhang, Y., Jiang, P., Vogler, E. A., & Lin, C. (2017). Effect of construction of TiO2 nanotubes on platelet behaviors: Structure-property relationships. *Acta Biomaterialia*, *51*, 505–512. https://doi.org/10.1016/j.actbio.2017.01.044

Im, S. H., Jung, Y., & Kim, S. H. (2017). Current status and future direction of biodegradable metallic and polymeric vascular scaffolds for next-generation stents. *Acta Biomaterialia*, *60*, 3–22. https://doi.org/10.1016/j.actbio.2017.07.019

Indira, K., Mudali, U. K., & Rajendran, T. N. N. (2015). A Review on TiO 2 Nanotubes : Influence of Anodization Parameters , Formation Mechanism , Properties , Corrosion Behavior , and Biomedical Applications. *Journal of Bio- and Tribo-Corrosion*, *1*(4), 1–22. https://doi.org/10.1007/s40735-015-0024-x

Iqbal, J., Gunn, J., & Serruys, P. W. (2013). Coronary stents: Historical development, current status and future directions. *British Medical Bulletin*, *106*(1), 193–211. https://doi.org/10.1093/bmb/ldt009

Ivanova, E. P., Hasan, J., Webb, H. K., Truong, V. K., Watson, G. S., Watson, J. A., Baulin, V. A., Pogodin, S., Wang, J. Y., Tobin, M. J., Löbbe, C., & Crawford, R. J. (2012). Natural bactericidal surfaces: Mechanical rupture of pseudomonas aeruginosa cells by cicada wings. *Small*, *8*(16), 2489–2494. https://doi.org/10.1002/smll.201200528

Jaganathan, S. K., Supriyanto, E., Murugesan, S., Balaji, A., & Asokan, M. K. (2014). Biomaterials in cardiovascular research: Applications and clinical implications. *BioMed Research International*, *2014*. https://doi.org/10.1155/2014/459465

Jang, Y., Choi, W. T., Johnson, C. T., García, A. J., Singh, P. M., Breedveld, V., Hess, D. W., & Champion, J. A. (2018). Inhibition of Bacterial Adhesion on

Nanotextured Stainless Steel 316L by Electrochemical Etching. *ACS Biomaterials Science and Engineering*, *4*(1), 90–97. https://doi.org/10.1021/acsbiomaterials.7b00544

Jebari-Benslaiman, S., Galicia-García, U., Larrea-Sebal, A., Olaetxea, J. R., Alloza, I., Vandenbroeck, K., Benito-Vicente, A., & Martín, C. (2022). Pathophysiology of Atherosclerosis. *International Journal of Molecular Sciences*, *23*(6), 1–38. https://doi.org/10.3390/ijms23063346

Knecht, D. A., Xue, F., & Janzen, D. M. (2010). Contribution of filopodia to cell migration: A mechanical link between protrusion and contraction. *International Journal of Cell Biology*, *2010*. https://doi.org/10.1155/2010/507821

Koster, R., Vieluf, D., & Sommerauer, M. (2001). Nickel and molybdenum contact allergies in patients with coronary in-stent restenosis. *ACC Current Journal Review*, *10*(3), 62. https://doi.org/10.1016/s1062-1458(01)00267-7

Kure, K., Konno, Y., Tsuji, E., Skeldon, P., Thompson, G. E., & Habazaki, H. (2012). Formation of self-organized nanoporous anodic films on Type 304 stainless steel. *Electrochemistry Communications*, *21*(1), 1–4. https://doi.org/10.1016/j.elecom.2012.05.003

Lamagni, T. (2014). Epidemiology and burden of prosthetic joint infections. *Journal of Antimicrobial Chemotherapy*, *69*(SUPPL1), 5–10. https://doi.org/10.1093/jac/dku247

Latifi, A., Imani, M., Khorasani, M. T., & Joupari, M. D. (2013). Electrochemical and chemical methods for improving surface characteristics of 316L stainless steel for biomedical applications. *Surface and Coatings Technology*, *221*, 1–12. https://doi.org/10.1016/j.surfcoat.2013.01.020

Le, X., Eddy, G., Poinern, J., Ali, N., Berry, C. M., & Fawcett, D. (2013). Engineering a Biocompatible Scaffold with Either Micrometre or Nanometre Scale Surface Topography for Promoting Protein Adsorption and Cellular Response. *International Journal of Biomaterials*, *2013*.

https://doi.org/10.1155/2013/782549

Li, M., Xu, X., Jia, Z., Shi, Y., Cheng, Y., & Zheng, Y. (2017). Rapamycin-loaded nanoporous α-Fe2O3 as an endothelial favorable and thromboresistant coating for biodegradable drug-eluting Fe stent applications. *Journal of Materials Chemistry B*, *5*(6), 1182–1194. https://doi.org/10.1039/c6tb02634f

Li, S., Liu, Y., Zheng, Z., Liu, X., Huang, H., Han, Z., & Ren, L. (2019). Biomimetic robust superhydrophobic stainless-steel surfaces with antimicrobial activity and molecular dynamics simulation. *Chemical Engineering Journal*, *372*(April), 852–861. https://doi.org/10.1016/j.cej.2019.04.200

Libby, P., Buring, J. E., Badimon, L., Hansson, G. K., Deanfield, J., Bittencourt, M. S., Tokgözoğlu, L., & Lewis, E. F. (2019). Atherosclerosis. *Nature Reviews Disease Primers*, *5*(1), 1–18. https://doi.org/10.1038/s41572-019-0106-z

Liu, L., Ercan, B., Sun, L., Ziemer, K. S., & Webster, T. J. (2016). Understanding the Role of Polymer Surface Nanoscale Topography on Inhibiting Bacteria Adhesion and Growth. *ACS Biomaterials Science and Engineering*, *2*(1), 122–130. https://doi.org/10.1021/acsbiomaterials.5b00431

Liu, S., Tian, J., & Zhang, W. (2021). Fabrication and application of nanoporous anodic aluminum oxide: A review. In *Nanotechnology* (Vol. 32, Issue 22). IOP Publishing. https://doi.org/10.1088/1361-6528/abe25f

Lu, Y., Cai, W. J., Ren, Z., & Han, P. (2022). The Role of Staphylococcal Biofilm on the Surface of Implants in Orthopedic Infection. *Microorganisms*, *10*(10). https://doi.org/10.3390/microorganisms10101909

Luo, J., Walker, M., Xiao, Y., Donnelly, H., Dalby, M. J., & Salmeron-Sanchez, M. (2022). The influence of nanotopography on cell behaviour through interactions with the extracellular matrix – A review. *Bioactive Materials*, *15*(August 2021), 145–159. https://doi.org/10.1016/j.bioactmat.2021.11.024

Łyczkowska-Widłak, E., Lochyński, P., & Nawrat, G. (2020). Electrochemical

polishing of austenitic stainless steels. In *Materials* (Vol. 13, Issue 11, pp. 1–25). https://doi.org/10.3390/ma13112557

M Chadi Alraies, Fahed Darmoch, Ramyashree Tummala, R. W. (2017). Diagnosis and management challenges of in-stent restenosis in coronary arteries. *World J Pediatr*, *9*(2).

Manivasagam, V. K., Sabino, R. M., Kantam, P., & Popat, K. C. (2021). Surface modification strategies to improve titanium hemocompatibility: A comprehensive review. *Materials Advances*, *2*(18), 5824–5842. https://doi.org/10.1039/d1ma00367d

Mattila, P. K., & Lappalainen, P. (2008). Filopodia: Molecular architecture and cellular functions. *Nature Reviews Molecular Cell Biology*, *9*(6), 446–454. https://doi.org/10.1038/nrm2406

Michiels, C. (2003). Endothelial cell functions. *Journal of Cellular Physiology*, *196*(3), 430–443. https://doi.org/10.1002/jcp.10333

Minagar, S., Berndt, C. C., Wang, J., Ivanova, E., & Wen, C. (2012). A review of the application of anodization for the fabrication of nanotubes on metal implant surfaces. *Acta Biomaterialia*, *8*(8), 2875–2888. https://doi.org/10.1016/j.actbio.2012.04.005

Mohan, C. C., Cherian, A. M., Kurup, S., Joseph, J., Nair, M. B., Vijayakumar, M., Nair, S. V., & Menon, D. (2017). Stable Titania Nanostructures on Stainless Steel Coronary Stent Surface for Enhanced Corrosion Resistance and Endothelialization. *Advanced Healthcare Materials*, *6*(11). https://doi.org/10.1002/adhm.201601353

Mohan, L., Dennis, C., Padmapriya, N., Anandan, C., & Rajendran, N. (2020). Effect of Electrolyte Temperature and Anodization Time on Formation of TiO 2 Nanotubes for Biomedical Applications. *Materials Today Communications*, *23*(April), 101103. https://doi.org/10.1016/j.mtcomm.2020.101103

Mohandesnezhad, S., Etminanfar, M., Mahdavi, S., & Safavi, M. S. (2022). Enhanced bioactivity of 316L stainless steel with deposition of polypyrrole / hydroxyapatite layered hybrid coating : Orthopedic applications. *Surfaces and Interfaces*, *28*(June 2021), 101604. https://doi.org/10.1016/j.surfin.2021.101604

Montanaro, L., Speziale, P., Campoccia, D., Ravaioli, S., Cangini, I., Pietrocola, G., Giannini, S., & Arciola, C. R. (2011). Scenery of Staphylococcus implant infections in orthopedics. *Future Microbiology*, *6*(11), 1329–1349. https://doi.org/10.2217/fmb.11.117

Moradi, S., Hadjesfandiari, N., Toosi, S. F., Kizhakkedathu, J. N., & Hatzikiriakos, S. G. (2016). Effect of Extreme Wettability on Platelet Adhesion on Metallic Implants: From Superhydrophilicity to Superhydrophobicity. *ACS Applied Materials and Interfaces*, *8*(27), 17631–17641. https://doi.org/10.1021/acsami.6b03644

Nagai, A., Suzuki, Y., Tsutsumi, Y., Nozaki, K., Wada, N., Katayama, K., Hanawa, T., & Yamashita, K. (2014). Anodic oxidation of a Co-Ni-Cr-Mo alloy and its inhibitory effect on platelet activation. *Journal of Biomedical Materials Research - Part B Applied Biomaterials*, *102*(4), 659–666. https://doi.org/10.1002/jbm.b.33044

Ni, S., Li, C., Ni, S., Chen, T., & Webster, T. J. (2014). Understanding improved osteoblast behavior on select nanoporous anodic alumina. *International Journal of Nanomedicine*, *9*(1), 3325–3334. https://doi.org/10.2147/IJN.S60346

Ni, S., Zhai, D., Huan, Z., Zhang, T., Chang, J., & Wu, C. (2020). Nanosized concave pit/convex dot microarray for immunomodulatory osteogenesis and angiogenesis. *Nanoscale*, *12*(31), 16474–16488. https://doi.org/10.1039/d0nr03886e

Noaman, S., O'Brien, J., Andrianopoulos, N., Brennan, A. L., Dinh, D., Reid, C., Sharma, A., Chan, W., Clark, D., Stub, D., Biswas, S., Freeman, M., Ajani, A.,

Yip, T., Duffy, S. J., & Oqueli, E. (2020). Clinical outcomes following ST-elevation myocardial infarction secondary to stent thrombosis treated by percutaneous coronary intervention. *Catheterization and Cardiovascular Interventions*, *96*(4), E406–E415. https://doi.org/10.1002/ccd.28802

Nouri, A., & Wen, C. (2021). Stainless steels in orthopedics. In C. B. T.-S. B. Wen (Ed.), *Woodhead Publishing Series in Biomaterials* (pp. 67–101). Woodhead Publishing. https://doi.org/https://doi.org/10.1016/B978-0-12-818831-6.00008-2

Nuhn, H., Blanco, C. E., & Desai, T. A. (2017). Nanoengineered Stent Surface to Reduce In-Stent Restenosis in Vivo. *ACS Applied Materials and Interfaces*, *9*(23), 19677–19686. https://doi.org/10.1021/acsami.7b04626

Pan, H. A., Liang, J. Y., Hung, Y. C., Lee, C. H., Chiou, J. C., & Huang, G. S. (2013). The spatial and temporal control of cell migration by nanoporous surfaces through the regulation of ERK and integrins in fibroblasts. *Biomaterials*, *34*(4), 841–853. https://doi.org/10.1016/j.biomaterials.2012.09.078

Park, K. S., Kang, S. N., Kim, D. H., Kim, H. B., Im, K. S., Park, W., Hong, Y. J., Han, D. K., & Joung, Y. K. (2020). Late endothelial progenitor cell-capture stents with CD146 antibody and nanostructure reduce in-stent restenosis and thrombosis. *Acta Biomaterialia*, *111*, 91–101. https://doi.org/10.1016/j.actbio.2020.05.011

Partida, E. B., Salas, B. V., Ulloa, A. M., Escamilla, A., Curiel, M. A., Ibáñez, R. R., Villarreal, F., Bastidas, D. M., & Bastidas, J. M. (2017). *Improved in vitro angiogenic behavior on anodized titanium dioxide nanotubes*. 1–21. https://doi.org/10.1186/s12951-017-0247-8

Pietrocola, G., Campoccia, D., Motta, C., Montanaro, L., Arciola, C. R., & Speziale, P. (2022). Colonization and Infection of Indwelling Medical Devices by Staphylococcus aureus with an Emphasis on Orthopedic Implants. *International Journal of Molecular Sciences*, *23*(11). https://doi.org/10.3390/ijms23115958

Piszczek, P., Radtke, A., Ehlert, M., Jędrzejewski, T., Sznarkowska, A., Sadowska, B., Bartmański, M., Erdoğan, Y. K., Ercan, B., & Jedrzejczyk, W. (2020). Comprehensive Evaluation of the Biological Properties of Surface-Modified Titanium Alloy Implants. *Journal of Clinical Medicine*, *9*(2). https://doi.org/10.3390/jcm9020342

Pober, J. S., & Sessa, W. C. (2007). Evolving functions of endothelial cells in inflammation. *Nature Reviews Immunology*, *7*(10), 803–815. https://doi.org/10.1038/nri2171

Rasouli, R., Barhoum, A., & Uludag, H. (2018). A review of nanostructured surfaces and materials for dental implants: Surface coating, patterning and functionalization for improved performance. *Biomaterials Science*, *6*(6), 1312–1338. https://doi.org/10.1039/c8bm00021b

Ren, B., Wan, Y., Liu, C., Wang, H., Yu, M., Zhang, X., & Huang, Y. (2021). Improved osseointegration of 3D printed Ti-6Al-4V implant with a hierarchical micro / nano surface topography: An in vitro and in vivo study. *Materials Science & Engineering C*, *118*(September 2020), 111505. https://doi.org/10.1016/j.msec.2020.111505

Resnik, M., Benčina, M., Levičnik, E., Rawat, N., Iglič, A., & Junkar, I. (2020). Strategies for improving antimicrobial properties of stainless steel. *Materials*, *13*(13), 1–22. https://doi.org/10.3390/ma13132944

Rodriguez-Contreras, A., Guadarrama Bello, D., Flynn, S., Variola, F., Wuest, J. D., & Nanci, A. (2018). Chemical nanocavitation of surfaces to enhance the utility of stainless steel as a medical material. *Colloids and Surfaces B: Biointerfaces*, *161*, 677–687. https://doi.org/10.1016/j.colsurfb.2017.11.051

Saito, T., Hokimoto, S., Oshima, S., Noda, K., Kojyo, Y., & Matsunaga, K. (2009). Metal allergic reaction in chronic refractory in-stent restenosis. *Cardiovascular Revascularization Medicine*, *10*(1), 17–22. https://doi.org/10.1016/j.carrev.2008.01.004

Sanchez, A. G., Schreiner, W., Duffó, G., & Ceré, S. (2011). Surface characterization of anodized zirconium for biomedical applications. *Applied Surface Science*, *257*(15), 6397–6405. https://doi.org/10.1016/j.apsusc.2011.02.005

Shuang, S., Ding, Z. Y., Chung, D., Shi, S. Q., & Yang, Y. (2020). Corrosion resistant nanostructured eutectic high entropy alloy. *Corrosion Science*, *164*(June 2019), 108315. https://doi.org/10.1016/j.corsci.2019.108315

Singh, A. V., Vyas, V., Patil, R., Sharma, V., Scopelliti, P. E., Bongiorno, G., Podestà, A., Lenardi, C., Gade, W. N., & Milani, P. (2011). Quantitative characterization of the influence of the nanoscale morphology of nanostructured surfaces on bacterial adhesion and biofilm formation. *PLoS ONE*, *6*(9). https://doi.org/10.1371/journal.pone.0025029

Staruch, R., Griffin, M., & Butler, P. (2017). Nanoscale Surface Modifications of Orthopaedic Implants: State of the Art and Perspectives. *The Open Orthopaedics Journal*, *10*(1), 920–938. https://doi.org/10.2174/1874325001610010920

Sutha, S., Kavitha, K., Karunakaran, G., & Rajendran, V. (2013). In-vitro bioactivity, biocorrosion and antibacterial activity of silicon integrated hydroxyapatite/chitosan composite coating on 316 L stainless steel implants. *Materials Science and Engineering C*, *33*(7), 4046–4054. https://doi.org/10.1016/j.msec.2013.05.047

Talha, M., Behera, C. K., & Sinha, O. P. (2013). A review on nickel-free nitrogen containing austenitic stainless steels for biomedical applications. *Materials Science and Engineering C*, *33*(7), 3563–3575. https://doi.org/10.1016/j.msec.2013.06.002

Torrado, J., Buckley, L., Durán, A., Trujillo, P., Toldo, S., Valle Raleigh, J., Abbate, A., Biondi-Zoccai, G., & Guzmán, L. A. (2018). Restenosis, Stent Thrombosis, and Bleeding Complications. *Journal of the American College of Cardiology*, *71*(15), 1676–1695. https://doi.org/10.1016/j.jacc.2018.02.023

Tsuchiya, H., Suzumura, T., Terada, Y., & Fujimoto, S. (2012). Formation of self-organized pores on type 316 stainless steel in organic solvents. *Electrochimica Acta*, *82*, 333–338. https://doi.org/10.1016/j.electacta.2012.06.048

Uslu, E., Mimiroglu, D., & Ercan, B. (2021). Nanofeature Size and Morphology of Tantalum Oxide Surfaces Control Osteoblast Functions. *ACS Applied Bio Materials*, *4*(1), 780–794. https://doi.org/10.1021/acsabm.0c01354

Wang, J., Song, C., Xiao, Y., & Liu, B. (2018). In vivo and in vitro analyses of the effects of a novel high-nitrogen low-nickel coronary stent on reducing in-stent restenosis. *Journal of Biomaterials Applications*, *33*(1), 64–71. https://doi.org/10.1177/0885328218773306

Wu, S., Altenried, S., Zogg, A., Zuber, F., Maniura-Weber, K., & Ren, Q. (2018). Role of the Surface Nanoscale Roughness of Stainless Steel on Bacterial Adhesion and Microcolony Formation. *ACS Omega*, *3*(6), 6456–6464. https://doi.org/10.1021/acsomega.8b00769

Yang, K., & Ren, Y. (2010). Nickel-free austenitic stainless steels for medical applications. *Science and Technology of Advanced Materials*, *11*(1), 014105. https://doi.org/10.1088/1468-6996/11/1/014105

Yao, H., He, Y., Ma, J., Jiang, L., Li, J., Wang, J., & Huang, N. (2021). Recent advances in cardiovascular stent for treatment of in-stent restenosis: Mechanisms and strategies. *Chinese Journal of Chemical Engineering*, *37*, 12–29. https://doi.org/10.1016/j.cjche.2020.11.025

Yau, J. W., Teoh, H., & Verma, S. (2015). Endothelial cell control of thrombosis. *BMC Cardiovascular Disorders*, *15*(1), 1–11. https://doi.org/10.1186/s12872-015-0124-z

Zal, E., Sarraf, M., Musharavati, F., Jaber, F., Wang, J. I., Reza, H., Hosseini, M., Bae, S., Chowdhury, M., So, H., & Liana, N. (2022). Effect of zirconia nanotube coating on the hydrophilicity and mechanochemical behavior of zirconium for biomedical applications. *Surfaces and Interfaces*, *28*(November

2021), 101623. https://doi.org/10.1016/j.surfin.2021.101623

Zhang, J., Li, G., Qu, Y., Guo, Z., Zhang, S., & Li, D. (2022). Fabrication and Hemocompatibility Evaluation of a Robust Honeycomb Nanostructure on Medical Pure Titanium Surface. *ACS Applied Materials and Interfaces*, *14*(7), 9807–9823. https://doi.org/10.1021/acsami.1c22818

Zhao, K., Wang, S., Lu, J., Ni, C., Wang, M., & Wang, S. (2021). Fabrication and characterization of anodic films onto the FeCrAl stainless steel in ethylene glycol electrolyte. *Surface and Coatings Technology*, *425*(July), 127707. https://doi.org/10.1016/j.surfcoat.2021.127707

Zheng, S., Bawazir, M., Dhall, A., Kim, H. E., He, L., Heo, J., & Hwang, G. (2021). Implication of Surface Properties, Bacterial Motility, and Hydrodynamic Conditions on Bacterial Surface Sensing and Their Initial Adhesion. *Frontiers in Bioengineering and Biotechnology*, *9*(February), 1–22. https://doi.org/10.3389/fbioe.2021.643722

Zhu, X., Jańczewski, D., Guo, S., Lee, S. S. C., Parra Velandia, F. J., Teo, S. L. M., He, T., Puniredd, S. R., & Julius Vancso, G. (2015). Polyion multilayers with precise surface charge control for antifouling. *ACS Applied Materials and Interfaces*, *7*(1), 852–861. https://doi.org/10.1021/am507371a

Zong, J., He, Q., Liu, Y., Qiu, M., Wu, J., & Hu, B. (2022). Advances in the development of biodegradable coronary stents: A translational perspective. *Materials Today Bio*, *16*(July). https://doi.org/10.1016/j.mtbio.2022.100368

APPENDICES

A.   XPS Spectra of Cr, Fe and Ni Binding Energy of Samples

Sample/ B. E	Chromium		Iron			Nickel	
	Cr_2O_3	CrO_3	FeOOH	Fe_2O_3	Fe	NiO	Ni
NA	576.3	-	712.4	710.4	706.9	855.4	852.8
ND25	576.9	578.5	713.6	711.2	707.2	856.2	853.4
ND200	576.9	578.5	712.7	710.7	707.2	856.2	-
NP25	577.2	579.7	713.7	711.4	707.2	856.6	-
NP200	576.7	579.3	-	710.5	707.0 (FeP)	853.0 - 855.8	-

Appendix A1 Table 1. The XPS spectra of Cr, Fe and Ni $2p_{3/2}$ binding energy of the NA, ND25, ND200, NP25 and NP200 surfaces.

B. XPS Spectra of O 1s Binding Energy of Samples

	OH^- B.E. (eV)	O^{2-} B.E. (eV)	Intensity: OH^-/O^{2-}
NA	531.6	529.8	2.24
ND25	531.6	531.1	5.41
ND200	532.0	530.1	4.85
NP25	531.8	531.2	5.70
NP200	531.5	530.3	3.52

Appendix B1 Table 1. The XPS spectra of O 1s binding energy and hydroxylation ratio of the NA, ND25, ND200, NP25 and NP200 surfaces.

CURRICULUM VITAE

Surname, Name: Erdoğan, Yaşar Kemal

EDUCATION

Degree	Institution	Year of Graduation
MS	Suleyman Demirel University/ Biomedical Engineering	2017
BS	Erciyes University/ Biomedical Engineering	2014
High School	İnönü High School, Çorum	2008

FOREIGN LANGUAGES

Advanced English

PUBLICATIONS

1. Erdogan, Y. K.; Ercan, B. Anodized Nanostructured 316L Stainless Steel Enhances Osteoblast Functions and Exhibits Anti-Fouling Properties. *ACS Biomater. Sci. Eng.* **2023**, *9* (2), 693–704. https://doi.org/10.1021/acsbiomaterials.2c01072.

2. Isik, M., Karakaya, E., Arslan, T. S., Atila, D., Erdogan, Y. K., Arslan, Y. E., Eskizengin, H., Eylem, C. C., Nemutlu, E., Ercan, B., D'Este, M., Okesola, B. O., Derkus, B., 3D Printing of Extracellular Matrix-Based Multicomponent, All-Natural, Highly Elastic, and Functional Materials toward Vascular Tissue Engineering. *Adv. Healthcare Mater.* **2023**, 12, 2203044. https://doi.org/10.1002/adhm.202203044

3. Karakaya, E., Erdogan, Y. K., Arslan, T. S., Arslan, Y. E., Odabas, S., Ercan, B., Emregul, E., Derkus, B., Decellularized Bone Extracellular Matrix-Coated Electrospun PBAT Microfibrous Membranes with Cell Instructive Ability and Improved Bone Tissue Forming Capacity. *Macromol. Biosci.* **2022**, 22, 2200303. https://doi.org/10.1002/mabi.202200303

4. Gardin, C.; Ferroni, L.; Erdoğan, Y.K.; Zanotti, F.; De Francesco, F.; Trentini, M.; Brunello, G.; Ercan, B.; Zavan, B. Nanostructured Modifications of Titanium Surfaces Improve Vascular Regenerative Properties of Exosomes Derived from Mesenchymal Stem Cells: Preliminary In Vitro Results. *Nanomaterials* **2021**, *11*, 3452. https://doi.org/10.3390/nano11123452

5. Piszczek, P.; Radtke, A.; Ehlert, M.; Jędrzejewski, T.; Sznarkowska, A.; Sadowska, B.; Bartmański, M.; Erdoğan, Y.K.; Ercan, B.; Jedrzejczyk, W. Comprehensive Evaluation of the Biological Properties of Surface-Modified Titanium Alloy Implants. *J. Clin. Med.* **2020**, *9*, 342. https://doi.org/10.3390/jcm9020342